



TECHNISCHE  
UNIVERSITÄT  
WIEN  
Vienna University of Technology

## Masterarbeit

# Diffusion Tensor Imaging

Ausgeführt am

Atominstitut der Technischen Universität Wien

und am Institut für

medizinische Physik und biomedizinische Technik

der Medizinischen Universität Wien

unter der Anleitung von

Univ.Prof. DI Dr.techn. Gerald Badurek

und

Assoc. Prof. Priv.-Doz. DI. Dr. Christian Windischberger

durch

Jasmin Tröstl

Ascherstraße 6

A-2734 Puchberg

Wien, 13.12.2011



# Contents

|  |           |
|--|-----------|
| <b>Zusammenfassung</b>   | <b>5</b>  |
| <b>Abstract</b>  | <b>7</b>  |
| <b>1 Physics of MRI</b>  | <b>9</b>  |
| 1.1 magnetic moment of the Orbital Motion . . . . .                            | 9         |
| 1.2 The Spin of Electrons . . . . .  | 12        |
| 1.3 The Spin of Nuclei . . . . .   | 15        |
| 1.4 Quantum Mechanical Consideration of the Spin in a Magnetic Field . . . . . | 16        |
| 1.5 Principles of Nuclear Magnetic Resonance . . . . .                         | 19        |
| 1.6 Relaxation . . . . .   | 23        |
| <b>2 Magnetic Resonance Imaging</b>  | <b>27</b> |
| 2.1 Signal Detection and Fourier Transform . . . . .                           | 27        |
| 2.2 Data Acquisition . . . . .   | 28        |
| 2.2.1 Slice Selection . . . . .  | 28        |
| 2.2.2 Spatial Encoding . . . . .   | 30        |
| 2.2.3 k-space . . . . .  | 33        |
| 2.3 MRI Sequence . . . . .   | 35        |
| 2.3.1 Spin Echo Sequence . . . . .   | 35        |
| 2.3.2 Echo-Planar Imaging . . . . .  | 36        |
| 2.4 Artifacts . . . . .  | 37        |
| 2.4.1 Chemical Shift Artifact . . . . .  | 37        |
| 2.4.2 Flow Artifacts . . . . .   | 38        |
| 2.4.3 Aliasing Artifacts . . . . .   | 40        |
| <b>3 Diffusion Tensor Imaging</b>  | <b>43</b> |
| 3.1 Diffusion . . . . .  | 43        |
| 3.2 Basics of Diffusion Tensor Imaging . . . . .                               | 44        |
| 3.3 Fractional Anisotropy . . . . .  | 50        |
| 3.4 Fiber Tractography . . . . .   | 52        |

|          |  |           |
|----------|--|-----------|
| 3.4.1    | Line Propagation Model . . . . .                                     | 52        |
| 3.4.2    | Probabilistic Fiber Tracking . . . . .                               | 55        |
| 3.4.3    | Pitfalls and Limitations of Fiber Tractography . . . . .             | 57        |
| <b>4</b> | <b>Data Preprocessing in DTI</b>                                     | <b>59</b> |
| 4.1      | Standard Preprocessing . . . . .                                     | 59        |
| 4.2      | DARTEL - A fast diffeomorphic image registration algorithm . . . . . | 64        |
| 4.3      | Tract Based Spatial Statistics - TBSS . . . . .                      | 71        |
| <b>5</b> | <b>Application of Diffusion Tensor Imaging</b>                       | <b>73</b> |
| 5.1      | Social Anxiety Disorder . . . . .                                    | 74        |
| 5.2      | Methods . . . . .  | 75        |
| 5.2.1    | Subjects . . . . .   | 75        |
| 5.2.2    | Acquisition . . . . .  | 76        |
| 5.3      | Analysis . . . . .   | 76        |
| 5.4      | Results . . . . .  | 78        |
| 5.5      | Discussion . . . . .   | 83        |
| <b>6</b> | <b>Conclusion and Outlook</b>  | <b>85</b> |
|          | <b>Bibliography</b>  | <b>87</b> |
|          | <b>List of Figures</b>   | <b>91</b> |
|          | <b>List of Tables</b>  | <b>97</b> |

# Zusammenfassung

Die Diffusions-Tensor-Bildgebung ist ein Magnetresonanztomographie-Verfahren zur Abschätzung des Anisotropiegrades von Wasserdiffusion. Je nach Gewebe ist die Diffusion nahezu isotrop (zum Beispiel in Flüssigkeiten oder in der grauen Substanz des Gehirns) oder gerichtet (zum Beispiel in der weißen Substanz des Gehirns). Diese Unterschiede in der Diffusion werden mittels eines Tensors für jedes gemessene Volumenelement (Voxel) abgeschätzt. Somit kann für jedes Voxel die Richtung der Diffusion, die Stärke und die Gerichtetheit approximiert werden. Bringt man die Eigenwerte dieses Diffusionstensors in Relation, kann die sogenannte fraktionale Anisotropie (FA) berechnet werden, die der Kohärenz und Gerichtetheit von Nervenfasern entspricht.

Die ersten diffusionsgewichteten Bilder wurden in den 1980er Jahren aufgenommen und erwiesen sich vor allem bei Schlaganfällen und Tumoren als hilfreiches diagnostisches Mittel. Die Diffusions-Tensor-Bildgebung findet aber auch Anwendung bei Erkrankungen wie Schizophrenie oder Multipler Sklerose. Diese Erkrankungen gehen mit morphologischen Veränderungen der Gehirnsubstanz einher, welche mit Hilfe von Diffusions-Tensor-Bildgebung nicht-invasiv und in-vivo untersucht werden können.

Weiters können auf der Basis von Diffusions-Tensor-Bildgebung Nervenbahnen innerhalb der weißen Substanz mittels Faser-Traktographie rekonstruiert werden. Diese Methode wird häufig verwendet, um Trakte zu identifizieren und die Integrität dieser zu untersuchen. Diese Rekonstruktion kann mittels sogenannter Streamlining Algorithmen durchgeführt werden. Dabei folgt man der dominanten Diffusionsrichtung bis ein Abbruchkriterium erfüllt ist. Eine weitere Methode zur Rekonstruktion ist die sogenannte probabilistische Faser-Traktographie. Mittels dieser Methode werden in einem ersten Schritt die Diffusionsrichtungen lokal abgeschätzt. Anschließend werden alle möglichen Faserverbindungen zwischen zwei beliebigen Punkten des Gehirns berechnet. Je öfter eine Faserverbindung durch ein bestimmtes Voxel berechnet wird, umso höher ist die Wahrscheinlichkeit, dass sich in diesem Voxel tatsächlich ein Nervenstrahl befindet. Somit wird die globale Konnektivität mittels einer Wahrscheinlichkeitsverteilung abgeschätzt.

In dieser Masterarbeit wurde die Diffusions-Tensor-Bildgebung angewandt um Unterschiede in den Diffusionsparametern der weißen Substanz zwischen Patienten mit Sozialphobie und gesunden Kontrollprobanden zu untersuchen. Dazu wurde die Analyse auf den Fasciculus Uncinatus

beschränkt, der Teile des präfrontalen Kortex, wie den Orbitofrontalkortex, mit Teilen des Temporallappen, wie zum Beispiel der Amygdala und dem Hippocampus, verbindet. Dieser Hirntrakt wurde mittels probabilistischer Faser-Traktographie berechnet. Die Ergebnisse zeigten eine bilateral verminderte fraktionale Anisotropie in Patienten in anterioren Teilen des Fasciculus Uncinatus nahe des Orbitofrontalenkortex. Dies deutet auf eine verminderte Konnektivität der Nervenfasern in diesem Teil des Gehirns hin. Weiters zeigten Patienten eine bilateral erhöhte fraktionale Anisotropie in posterioren Teilen des Fasciculus Uncinatus. Eine Interpretation dieser erhöhten Konnektivität zeigte sich allerdings als schwierig, sodass weitere Untersuchungen erforderlich sind.

# Abstract

Diffusion tensor imaging is a magnetic resonance imaging technique which allows for approximating the grade of anisotropy of water diffusion in organized matter, such as the human brain or muscles. Depending on the tissue, diffusion is either isotropic (e.g. grey matter) or directed (e.g. white matter). These differences can be approximated for every voxel by using a tensor. With this diffusion tensor the diffusion strength, direction and directionality can be estimated. By relating the eigenvalues of the diffusion tensor, the fractional anisotropy (FA) can be calculated, which represents the directionality and coherence of fibers.

The first diffusion-weighted images were acquired in the 1980s. These measurements proofed beneficial for the diagnosis of stroke and tumors. Today, diffusion tensor imaging is used for diseases like schizophrenia and multiple sclerosis, but also other neurological diseases that go along with morphological changes of brain tissue. These changes can be analyzed non-invasively in-vivo using diffusion tensor imaging.

On the basis of diffusion tensor imaging nerve bundles and fiber tracts can be reconstructed using fiber tractography. This method can be used for the identification of fiber tracts and to analyze tract integrity. For the reconstruction of a fiber tract so-called streamlining algorithms can be used. With this method the dominant diffusion direction is followed until a termination criterion is fulfilled. Another method is the so-called probabilistic fiber tracking. This routine locally estimates the diffusion direction first. Then all possible fiber connections between voxels are calculated. The more connections are calculated through a certain voxel, the higher is the probability that there really exists a connection within this voxel. Therefore the global connectivity is approximated by a probability distribution.

Here this magnetic resonance imaging technique was applied to investigate white matter differences between social phobia patients and healthy controls. For this purpose the analysis was limited to the uncinate fasciculus, which connects frontal regions such as orbitofrontal cortex with posterior regions such as hippocampus and amygdala. This fiber tract was calculated using probabilistic fiber tractography. The results showed decreased FA in patients bilaterally in anterior parts of the uncinate fasciculus next to orbitofrontal cortex. This indicates a reduced fiber connectivity in these brain areas. In addition areas with increased FA in patients were found bilaterally in

posterior parts of the uncinate fasciculus. The interpretation of this increased connectivity was difficult so that further studies are required.



# Chapter 1

## Physics of MRI

### 1.1 magnetic moment of the Orbital Motion

In general the magnetic moment of a current density distributions  $\mathbf{j}(\mathbf{r})$  is given by

$$\boldsymbol{\mu} = \frac{1}{2} \int_V \mathbf{r} \times \mathbf{j}(\mathbf{r}) dV \quad (1.1)$$

In classical physics the electron orbits the atomic nucleus. This orbital motion can also be seen as an electrical current.

$$\mathbf{j}(\mathbf{r}) dV = I d\mathbf{r} \quad (1.2)$$

The magnetic dipole momentum of such a loop then is

$$\boldsymbol{\mu} = \frac{I}{2} \cdot \int \mathbf{r} \times d\mathbf{r} = I \cdot \mathbf{A} \quad \begin{array}{l} I \dots \text{electrical current} \\ \mathbf{A} \dots \text{are a vector perpendicular to loop plane} \end{array} \quad (1.3)$$

When we now put this loop into a magnetic field  $\mathbf{B}$  the following torque  $\boldsymbol{\tau}$  acts on it:

$$\boldsymbol{\tau} = \boldsymbol{\mu} \times \mathbf{B} \quad (1.4)$$

To compare and transfer this equation to an atom we assume that the electron orbits the atomic nucleus with a time period of  $T$ , which corresponds to  $\frac{2\pi}{\omega}$  ( $\omega$  being the angular frequency of the orbital motion). The current generated by the orbital motion can then be described as:

$$I = \frac{q}{T} = -\frac{e \cdot \omega}{2\pi} \quad \text{with} \quad \begin{array}{l} q \dots \text{electrical charge} \\ e = 1.602176565 \cdot 10^{-19} \text{ C} \dots \text{elementary charge} \end{array} \quad (1.5)$$

Using this expression and inserting into (1.3) we get

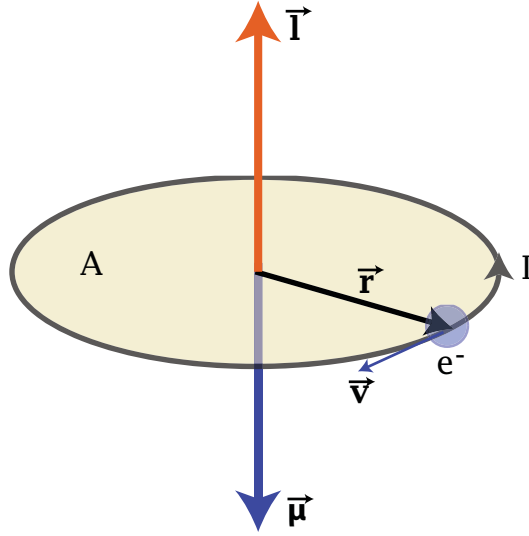


**Figure 1.1:** Classical picture of the angular momentum  $\mathbf{l}$  and magnetic moment  $\boldsymbol{\mu}$  due to the orbital motion of the electron with the velocity  $\mathbf{v}$  and the radius  $r$ .

$$\boldsymbol{\mu} = I \cdot \mathbf{A} = -\frac{1}{2}e\omega r^2 \mathbf{e}_{\perp} \quad (1.6)$$

with  $\mathbf{A} = r^2\pi\mathbf{e}_{\perp}$  and  $\mathbf{e}_{\perp}$  the unit vector in the direction of  $\mathbf{A}$ . Now we can introduce the orbital angular momentum  $|\mathbf{l}| = m_e |v| r = m_e \omega r^2$  ( $m_e$ ...rest mass of the electron,  $|v|$ ...velocity of the electron,  $r$ ...radius of the orbital motion). We find the following relationship:

$$\boldsymbol{\mu} = -\frac{e}{2m_e} \mathbf{l} = -\gamma_e \mathbf{l} \quad \gamma \dots \text{gyromagnetic ratio of the electron} \quad (1.7)$$

We see that in case of the electron  $\boldsymbol{\mu}$  and  $\mathbf{l}$  point in the opposite direction (see figure 1.1).

The gyromagnetic ratio  $\gamma = \frac{q}{2m}$  ( $q$ ...electrical charge,  $m$ ...mass of particle) is the ratio between magnetic dipole moment and angular momentum and is generally dependent on the considered material. Considering electrons the gyromagnetic ratio is  $\gamma_e = \frac{|-e|}{2m_e}$ . Further we can make use of the Bohr model. We know that the electron in the first orbit has an orbital angular momentum of  $l = \hbar$ . Inserting this in (1.7) yields the Bohr magneton  $\mu_B$ :

$$\mu_B = \frac{e}{2m_e} \hbar = 9.274078 \cdot 10^{-24} \text{Am}^2 \quad (1.8)$$

We can now define the magnetic moment of the electron  $\boldsymbol{\mu}_l$  in units of  $\mu_B$ :

$$\boldsymbol{\mu}_l = -\mu_B \frac{\mathbf{l}}{\hbar} \quad (1.9)$$

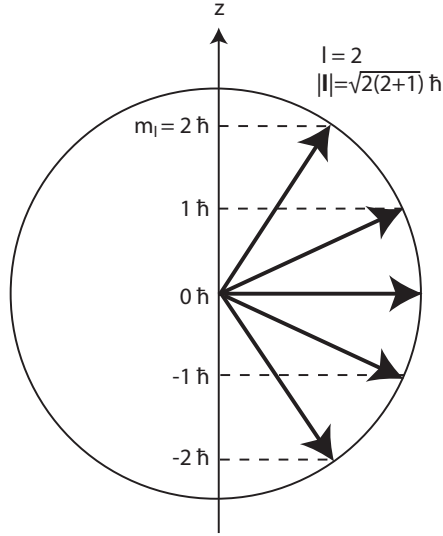


**Figure 1.2:** Quantized angular momentum with  $l = 2$ .

When we now apply a magnetic field  $\mathbf{B}$ , a torque acts on  $\boldsymbol{\mu}_l$  aiming for parallel alignment of the magnetic moment and  $\mathbf{B}$ . The magnetic moment  $\boldsymbol{\mu}_l$  will precess around  $\mathbf{B}$ . The precession frequency can be calculated as follows:

$$\frac{\partial \mathbf{l}}{\partial t} = \boldsymbol{\tau} = \boldsymbol{\mu} \times \mathbf{B}, \quad \frac{\partial \mathbf{l}}{\partial t} = -\gamma_e \cdot \mathbf{l} \times \mathbf{B} \quad (1.10)$$

$$\frac{\partial \mathbf{l}}{\partial t} = \boldsymbol{\omega}_L \times \mathbf{l}$$

Comparing the equations in (1.10) yields the precession frequency

$$\boldsymbol{\omega}_L = \gamma_e \mathbf{B} = \frac{g_l e \hbar}{2m_0} \mathbf{B} \quad (1.11)$$

This angular frequency is the so-called Larmor frequency  $\boldsymbol{\omega}_L$ . The z-component of  $\mathbf{l}$  is not random but quantized. This cannot be explained by classical physics. Therefore we introduce the quantum mechanical angular momentum  $\mathbf{l}$  which has one quantized axis, in our case  $l_z$ . The possible values are:

$$l_z = m_l \hbar \quad \text{with } m_l = 0, \pm 1, \dots, \pm l \quad (1.12)$$

Here we also introduce  $m_l$ , the magnetic quantum number. Accordingly  $\mu_{l,z}$  is:

$$\mu_{l,z} = -\frac{e}{2m_e} l_z = -m_l \mu_B \quad (1.13)$$

Since  $m_l$  can only have certain values ( $m_l = 0, \pm 1, \dots, \pm l$ ) the maximum value of  $\mu_{l,z}$  is  $\mu_{l,z} = l \cdot \mu_B$ .

The absolute value of  $\mathbf{l}$  is:

$$|\mathbf{l}| = \sqrt{l(l+1)} \cdot \hbar \quad (1.14)$$

Figure 1.2 shows a quantized angular momentum with  $l = 2$ . In this section we have seen that the motion of electrical charges leads to an angular momentum  $\mathbf{l}$ , which is quantized as soon as one axis is specified (e.g. by applying a magnetic field). We also introduced the magnetic moment  $m_l$ . Besides this semi-classical consideration, a second mechanism results into a magnetic moment, which cannot be explained by classical physics. This mechanism is due to the intrinsic angular momentum of elementary particles called spin.

## 1.2 The Spin of Electrons

In the late 19<sup>th</sup> and in the early 20<sup>th</sup> century several experiments indicated that elementary particles such as electrons have an additional property besides charge  $-e$  and rest mass  $m_e$ . One of these experiments was arranged by Otto Stern (1888-1969) and Walter Gerlach (1889-1979). In their experiment in 1921 - the so-called Stern-Gerlach experiment (see figure 1.3) - they investigated the deflection of silver atoms in an inhomogeneous magnetic field. The silver atoms were evaporated in an oven. The evaporated atoms could escape through an opening and were collimated using an aperture. The atoms were passing an orthogonal inhomogeneous magnetic field  $\mathbf{B}$ . The experiment was repeated without a magnetic field  $\mathbf{B}$ . Without any magnetic field no force is acting on the atoms and they do not get deflected. When we now apply the inhomogeneous magnetic field  $\mathbf{B}$  the deflection showed two clear maxima, which can be seen in figure 1.3. An inhomogeneous magnetic field exerts an additional force on a magnetic moment. This force depends on the relative orientation of the magnetic field and the magnetic moment. From the potential energy of the magnetic field we can calculate the force acting on the magnetic moment:

$$E_{pot} = -\boldsymbol{\mu}_l \mathbf{B} \quad (1.15)$$

$$\mathbf{F} = -\nabla E_{pot} = \boldsymbol{\mu}_l \nabla \mathbf{B} \quad (1.16)$$

The ground state of an silver atom is an s-state ( $l = 0$ ) which means that the atom does not have an orbital magnetic dipole moment ( $\mu_l = 0$ ). Therefore they suggested that the electron has an additional intrinsic angular momentum which leads to the seen deflection. Also an earlier experimental result indicated such a property: the anomalous Zeeman effect. The normal Zeeman effect is very easy to explain, it is the splitting of spectral lines in several components due to a magnetic field. We already know the potential energy of the magnetic field ( $E_{pot} = -\boldsymbol{\mu}_l \mathbf{B}$ ). And we also know the relationship between  $\boldsymbol{\mu}_l$  and the Bohr magneton  $\mu_B$  (1.9). Applying a magnetic field in the z-direction we can use (1.13) and get the potential energy:

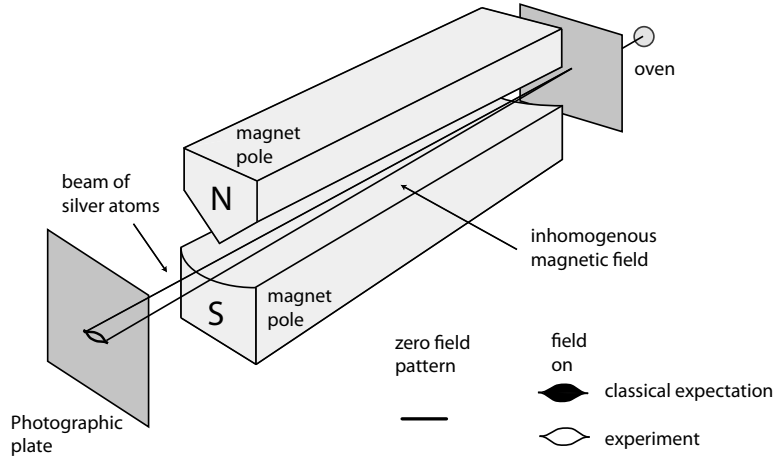


**Figure 1.3:** Stern-Gerlach Experiment. The particle beam of neutral silver atoms passes through an inhomogeneous magnetic field in z-direction. In the figure you see the set-up of the magnetic poles, which produce the magnetic field. The particle beam is detected at a photographic plate. Without a magnetic field no deflection is measured (straight line at photographic plate). When the magnetic field is turned on the classical expectation was a homogenous distribution, as it was believed that the orientation of the magnetic moment should be random. But the results showed two clear maxima. This is due to the quantization of  $s_z$ . Only two orientations are possible (spin up and spin down) yielding the two maxima.

$$E_{pot} = -m_l \mu_B B_z \quad \text{with} \quad -l \leq m_l \leq l \quad (1.17)$$

Due to this quantization the degenerate energy levels are split and can be seen in the atomic spectrum. If the atom is in an s-state (with  $l = 0$ ),  $E_{pot}$  is zero, hence we should not see splitting. However, the spectral lines split in the atomic spectrum. This is the so-called anomalous Zeeman effect. The splitting of the degenerate energy levels in s-state atoms (anomalous Zeeman effect) can only be explained by introducing a new quantum number representing the intrinsic angular momentum of the electron.

In 1924 Wolfgang Pauli proposed this new quantum number with two possible values. One year later in 1925 Samuel A. Goudsmit (1902-1978) and George E. Uhlenbeck (1900-1988) called this new quantum number spin  $s$ . The absolute value of the spin is analogous to the orbital angular momentum

$$|s| = \sqrt{s(s+1)} \cdot \hbar \quad (1.18)$$

Considering the Stern-Gerlach experiment we have seen that two maxima were measured when the inhomogeneous magnetic field was applied. Due to the electron configuration in silver atoms only one electron spin (only one valence electron) can contribute to the magnetic moment, all other

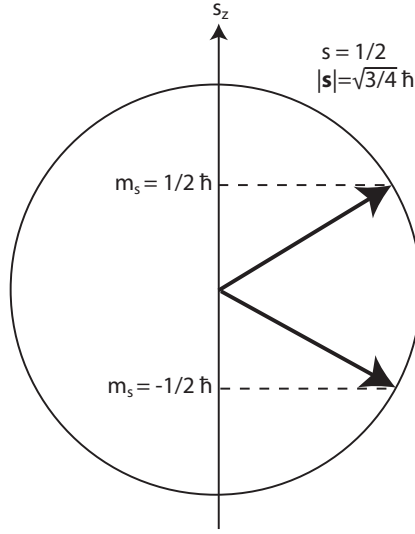


**Figure 1.4:** Two possible orientations (spin up and spin down) of the electron spin.

compensate each other. Therefore only two possible orientations (see figure 1.4) of the spin are possible (with  $m_s$  being the magnetic quantum number of the spin):

$$s_z = m_s \cdot \hbar \quad \text{with} \quad m_s = \pm \frac{1}{2}. \quad (1.19)$$

The absolute value of the electronic spin is then (see (1.18))

$$|s| = \frac{\sqrt{3}}{2} \cdot \hbar \quad (1.20)$$

Analogous to the magnetic moment, we can define the intrinsic magnetic moment of the electron and its z-component:

$$\boldsymbol{\mu}_s = -g_s \frac{e}{2m_e} \mathbf{s} \quad (1.21)$$

$$\mu_{s,z} = -g_s m_s \mu_B \quad \text{with} \quad m_s = \pm \frac{1}{2} \quad (1.22)$$

$g_s$  is the g-factor of the electron spin, which relates the intrinsic magnetic moment with the intrinsic angular momentum of the electron. Now we can also define the gyromagnetic ration  $\gamma_s$  of the electron spin

$$\gamma_s = g_s \mu_B \hbar \quad (1.23)$$

### 1.3 The Spin of Nuclei

Also protons and neutrons (the components of nuclei) have an intrinsic angular momentum. We can now introduce the nuclear spin  $\mathbf{I}$ :

$$|\mathbf{I}| = \sqrt{I(I+1)}\hbar \quad (1.24)$$

$I$  is the nuclear spin quantum number. According to the magnetic quantum number of the electron spin  $m_s$  (1.19) we also adopt the nuclear magnetic quantum number  $m_I$ . For the  $z$ -component of the nuclear spin we get:

$$I_z = m_I \hbar \quad \text{with} \quad -I \leq m_I \leq I \quad (1.25)$$

For the magnetic nuclear momentum we get:

$$\boldsymbol{\mu}_I = \frac{g_I \mu_N}{\hbar} \mathbf{I} = \gamma_I \mathbf{I} \quad (1.26)$$

$\gamma_I = \frac{e g_I}{2 m_p}$  is the gyromagnetic ratio, conventionally the proton mass  $m_p$  is used for the definition of  $\gamma_I$ . Here we also introduce the nuclear g-factor  $g_I$  which relates the nuclear magnetic moment  $\boldsymbol{\mu}_I$  with the nuclear angular momentum  $\mathbf{I}$ . For electrons we had the Bohr magneton  $\mu_B$ , here we have the nuclear magneton  $\mu_N = \frac{e}{2 m_p} \hbar = \mu_B / 1836 = 5.0508244 \cdot 10^{-27} \text{ Am}^2$ , which contains the proton mass  $m_p$  instead of the electron mass  $m_e$ . Most atomic nuclei possess spin. As nuclei consist of protons and neutrons, the nuclear spin depends on the proton and neutron number.

Hydrogen  ${}^1_1\text{H}$  consists of only one proton; therefore the nuclear spin quantum number is  $I = \frac{1}{2}$ . When we now consider the hydrogen isotope  ${}^2_1\text{H}$  (deuterium) consisting of one proton and one neutron, the overall nuclear-spin depends on whether the spins of the proton and the neutron are in a parallel configuration ( $I = 1$ ) or in an anti-parallel configuration ( $I = 0$ ). The nuclear spin has either an integer or half integer nuclear spin quantum number  $I$ . Each configuration has an energy level. In case of deuterium the energy of the configuration with  $I = 1$  is lower than for  $I = 0$ . Therefore the ground state of deuterium is an  $I = 1$  state. This is possible due to proton and neutron coupling. Considering only two protons or two neutrons, this configuration would not be possible due to the Pauli exclusion principle. Table 1.1 shows a selection of nuclei, their spin in ground state, their natural abundance relative to isotopes from the same element and their Larmor frequency.

| Isotope                 | Ground-state<br>spin | relative natural abundance<br>of isotopes (%) | Larmor Frequency<br>at 1 T $\omega/2\pi/(MHz)$ |
|-------------------------|----------------------|---|--|
| ${}^1_1\text{H}$        | 1/2                  | 99.9885                                       | 42.589   |
| ${}^2_1\text{H}$        | 1                    | 0.0115  | 6.538  |
| ${}^3_1\text{H}$        | 1/2                  | 0   | 45.428   |
| ${}^{13}_6\text{C}$     | 1/2                  | 1.1   | 10.709   |
| ${}^{14}_7\text{N}$     | 1                    | 99.6  | 3.078  |
| ${}^{15}_7\text{N}$     | 1/2                  | 0.37  | 4.317  |
| ${}^{23}_{11}\text{Na}$ | 3/2                  | $\sim 100$                                    | 11.266   |
| ${}^{31}_{15}\text{P}$  | 1/2                  | $\sim 100$                                    | 17.258   |

**Table 1.1:** In this table a small selection of nuclear isotopes including spin, natural abundance and Larmor frequency at 11.4 Tesla are displayed. More Isotopes can be found on [www.webelements.com](http://www.webelements.com)

## 1.4 Quantum Mechanical Consideration of the Spin in a Magnetic Field

Applying a static magnetic field we have seen that the angular momentum of electron orbital motion precesses around the magnetic field lines. We have introduced the spin of electrons and the nuclear spin of atomic nuclei using semi-classical physics. In this section we consider the nuclear spin using quantum mechanics. We will see that the nuclear spin will also precess in the presence of a static magnetic field.

I limit the considerations to a hydrogen  ${}^1_1\text{H}$  nucleus in the ground state  $I = 1/2$  (which is equivalent to the consideration of a single proton with spin  $s=1/2$ ). The magnetic moment of  ${}^1_1\text{H}$  can be formulated in vector form:

$$\boldsymbol{\mu}_I = \frac{g_I \mu_N}{\hbar} \mathbf{I} = \gamma_I \mathbf{I} \quad (1.27)$$

The potential energy of the spin in a static homogeneous magnetic field is

$$E_{pot} = -\boldsymbol{\mu}_I \mathbf{B}. \quad (1.28)$$

For a quantum mechanical consideration we need the Schrödinger equation. The Hamiltonian in this case is  $\hat{\mathbf{H}} = -\boldsymbol{\mu}_I \mathbf{B} = -\gamma_I \mathbf{B} \hat{\mathbf{I}}$  yielding the time independent Schrödinger equation:

$$-\gamma_I \mathbf{B} \hat{\mathbf{I}} \phi = E \phi \quad \begin{array}{l} \phi \dots \text{nuclear spin function} \\ B = (B_x, B_y, B_z) \end{array} \quad (1.29)$$



$^1_1\text{H}$ , which is the most frequently used nucleus for magnetic resonance, has a nuclear spin of  $I = \frac{1}{2}$ , therefore only two values are possible for  $m_I$  ( $+\frac{1}{2}$  for spin up and  $-\frac{1}{2}$  for spin down). Here we introduce the nuclear spin operator  $\hat{\mathbf{I}}$

$$\hat{\mathbf{I}} = \begin{pmatrix} \hat{I}_x \\ \hat{I}_y \\ \hat{I}_z \end{pmatrix} \quad (1.30)$$

with the following components:

$$\hat{I}_x = \frac{\hbar}{2} \begin{pmatrix} 0 & 1 \\ 1 & 0 \end{pmatrix} \quad \hat{I}_y = \frac{\hbar}{2} \begin{pmatrix} 0 & -i \\ i & 0 \end{pmatrix} \quad \hat{I}_z = \frac{\hbar}{2} \begin{pmatrix} 1 & 0 \\ 0 & -1 \end{pmatrix} \quad (1.31)$$

Calculation of  $\hat{\mathbf{I}}^2 = \hat{I}_x^2 + \hat{I}_y^2 + \hat{I}_z^2$  yields

$$\hat{I}^2 = \hbar^2 \frac{3}{4} \begin{pmatrix} 1 & 0 \\ 0 & 1 \end{pmatrix}. \quad (1.32)$$

We can now define eigenfunctions of the  $\hat{I}_z$  operator. We choose eigenfunctions representing spin up ( $|\uparrow\rangle$ ) and spin down ( $|\downarrow\rangle$ ):

$$|\uparrow\rangle = \begin{pmatrix} 1 \\ 0 \end{pmatrix} \quad |\downarrow\rangle = \begin{pmatrix} 0 \\ 1 \end{pmatrix} \quad (1.33)$$

When we now apply the operator on its eigenfunctions we get the eigenvalues:

$$\hat{I}_z |\uparrow\rangle = \frac{\hbar}{2} \begin{pmatrix} 1 & 0 \\ 0 & -1 \end{pmatrix} \begin{pmatrix} 1 \\ 0 \end{pmatrix} = +\frac{\hbar}{2} \begin{pmatrix} 1 \\ 0 \end{pmatrix} = +\frac{\hbar}{2} |\uparrow\rangle \quad (1.34)$$

$$\hat{I}_z |\downarrow\rangle = \frac{\hbar}{2} \begin{pmatrix} 1 & 0 \\ 0 & -1 \end{pmatrix} \begin{pmatrix} 0 \\ 1 \end{pmatrix} = -\frac{\hbar}{2} \begin{pmatrix} 0 \\ 1 \end{pmatrix} = -\frac{\hbar}{2} |\downarrow\rangle \quad (1.35)$$

$$\hat{I}_z |I, m_I\rangle = \hbar m_I |I, m_I\rangle \quad \text{with} \quad \begin{array}{l} m_I = +\frac{1}{2} \text{ for } |\uparrow\rangle \\ m_I = -\frac{1}{2} \text{ for } |\downarrow\rangle \end{array} \quad (1.36)$$

Using (1.31) we can rewrite our Hamiltonian  $\hat{\mathbf{H}}$ :

$$\hat{\mathbf{H}} = -\frac{e\hbar}{2m_p} \begin{pmatrix} B_z & B_x - iB_y \\ B_x + iB_y & -B_z \end{pmatrix} \quad (1.37)$$

When we apply a magnetic field in z-direction ( $\mathbf{B} = (0, 0, B_z)$ ) we get the following Schrödinger equation

$$-\frac{e\hbar}{2m_p} B_z \begin{pmatrix} 1 & 0 \\ 0 & -1 \end{pmatrix} \phi = E\phi. \quad (1.38)$$

This equation is equivalent to the eigenvalue problem in (1.34) and (1.35) except for the factor  $\frac{eB_z}{m_p}$ , so we already know the result of this equation:

$$E_{\downarrow\uparrow} = \pm \frac{e\hbar B_z}{2m_p} = -\mu_N B_z = -\gamma_I B_z \hbar m_I \quad (1.39)$$

Additionally, we now consider the time-dependent Schrödinger equation. This consideration is especially important when the magnetic field is varying in time. At first we restrict our calculations to a static magnetic field in the z-direction.

$$-\mu_N B_z \begin{pmatrix} 1 & 0 \\ 0 & -1 \end{pmatrix} \phi = i\hbar \frac{\partial \phi}{\partial t}. \quad (1.40)$$

The general solution of this equation can be obtained by a superposition of  $|\uparrow\rangle$  and  $|\downarrow\rangle$  with corresponding time functions:

$$|\phi(t)\rangle = A \cdot \exp(-i \frac{e}{2m_p} B_z t) |\uparrow\rangle + B \cdot \exp(+i\hbar \frac{e}{2m_p} B_z t) |\downarrow\rangle = \alpha |\uparrow\rangle + \beta |\downarrow\rangle. \quad (1.41)$$

A and B are amplitudes of the functions ( $A, B \in \mathbb{C}$ ). In quantum mechanics  $|\phi(t)\rangle$  must be normalized, this can be achieved with  $\langle\phi(t) | \phi(t)\rangle = |A|^2 + |B|^2 = 1$ . The expected value of the nuclear spin component can be calculated with  $\hat{I}_z$  with  $\langle\phi(t) | \hat{I}_z | \phi(t)\rangle$ . With equation (1.33) follows

$$|\phi(t)\rangle = \begin{pmatrix} \alpha \\ \beta \end{pmatrix}. \quad (1.42)$$

The expected value of  $\hat{I}_z$  then is

$$\langle\hat{I}_z\rangle = \langle\phi(t) | \hat{I}_z | \phi(t)\rangle = \begin{pmatrix} \alpha^* & \beta^* \end{pmatrix} \cdot \frac{\hbar}{2} \begin{pmatrix} 1 & 0 \\ 0 & -1 \end{pmatrix} \cdot \begin{pmatrix} \alpha \\ \beta \end{pmatrix} = \frac{\hbar}{2} (|\alpha|^2 - |\beta|^2). \quad (1.43)$$

The same can be repeated for  $\langle\hat{I}_x\rangle$  and for  $\langle\hat{I}_y\rangle$ :

$$\langle\hat{I}_x\rangle = \langle\phi(t) | \hat{I}_x | \phi(t)\rangle = \begin{pmatrix} \alpha^* & \beta^* \end{pmatrix} \cdot \frac{\hbar}{2} \begin{pmatrix} 0 & 1 \\ 1 & 0 \end{pmatrix} \cdot \begin{pmatrix} \alpha \\ \beta \end{pmatrix} = \frac{\hbar}{2} (\alpha^* \beta + \alpha \beta^*) \quad (1.44)$$

$$\langle\hat{I}_y\rangle = \langle\phi(t) | \hat{I}_y | \phi(t)\rangle = \begin{pmatrix} \alpha^* & \beta^* \end{pmatrix} \cdot \frac{\hbar}{2} \begin{pmatrix} 0 & -i \\ i & 0 \end{pmatrix} \cdot \begin{pmatrix} \alpha \\ \beta \end{pmatrix} = \frac{i\hbar}{2} (\alpha \beta^* - \alpha^* \beta) \quad (1.45)$$

Using

$$\alpha = A \cdot \exp(-i \frac{e}{2m_p} B_z t) \quad (1.46)$$

$$\beta = B \cdot \exp\left(+i \frac{e}{2m_p} B_z t\right) \quad (1.47)$$

we see that  $\langle \hat{I}_z \rangle$  is constant over time. But  $\langle \hat{I}_x \rangle$  is proportional to  $\cos(\frac{eB_z}{2m_p} t) = \cos(\omega_L t)$  and  $\langle \hat{I}_y \rangle$  is proportional to  $\sin(\frac{eB_z}{2m_p} t) = \sin(\omega_L t)$ . The components in the x-y-plane precess with the Larmor frequency  $\omega_L$  while the z-component is constant.

## 1.5 Principles of Nuclear Magnetic Resonance

Elementary particles such as electrons, protons and neutrons have a spin of  $s = 1/2$ . Also atomic nuclei have a spin  $I$ ; the value depends on the number of protons and neutrons.

Let us again consider an ensemble of hydrogen  ${}^1\text{H}$  nuclei with a nuclear spin of  $I = 1/2$ . When a static magnetic field is applied the spins start to precess around the magnetic field lines, following the quantum mechanic rules of quantization. They can only align in discrete angles ( $2I + 1$  possible values for  $m_I$ ). The Larmor frequency of the nuclear spins is:

$$\omega_L = \frac{g_I \mu_N}{\hbar} B = \frac{g_I e B}{2m_p} = \gamma_I B \quad (1.48)$$

We have also seen that the energy of the nuclear spin is quantized in a magnetic field. The potential energy of the nuclear magnetic moment is, using  $\boldsymbol{\mu}_I = \frac{g_I \mu_N}{\hbar} \mathbf{I}$ :

$$E_{\text{pot}} = -\boldsymbol{\mu}_I \mathbf{B} = -g_I \mu_N B = -\gamma_I B \hbar m_I \quad \text{with } -I \leq m_I \leq I \quad (1.49)$$

The energy difference between two possible orientations ( $m_I \pm 1/2 \rightarrow \delta m_I = \pm 1$ ) is then:

$$|\Delta E| = \gamma_I \hbar B \quad (1.50)$$

This splitting of energy levels due to a magnetic field is called nuclear Zeeman effect. A transition between both levels is possible when a photon with the energy  $\Delta E = \hbar \omega_L = g_I \mu_N B = \gamma_I B$  is absorbed or radiated, respectively. This is the principle of nuclear magnetic resonance. By absorption of a photon with the energy  $\Delta E$  the nuclear spin gets excited which means that it transits from a state of lower energy to a state of higher energy. An excited spin can also emit a photon with the energy  $\Delta E$ , doing this the spin de-excites which means that the spin transits from a state of higher energy to a state of lower energy.

In thermal equilibrium the magnetic energy (see equation (1.50)) is much smaller than the thermal energy  $k_B T$ , therefore both energy states have nearly the same probability, with  $T$  being the temperature and  $k_B$  the Boltzmann constant ( $k_B = 1.3807 \cdot 10^{-23} \text{ J/K}$ ). At room temperature and a magnetic field of 1 Tesla, the excess of the number of spins in the energetic efficient states would be only  $10^{-5}$ . This distribution can be calculated with the Boltzmann statistics:

$$\frac{N_{+1/2}}{N_{-1/2}} = \exp \frac{\Delta E}{k_B \cdot T} \quad \text{with} \quad \begin{array}{l} N_{+1/2} \dots \text{number of } \uparrow - \text{spins} \\ N_{-1/2} \dots \text{number of } \downarrow - \text{spins} \end{array} \quad (1.51)$$

Therefore, the transition will hardly be observed, because the number of emitted photons would be too small, unless there is a large number of nuclei. However, at room temperature the population differs only by  $10^{-5}$ , the difference in population still leads to a net magnetization. For the population difference we find ( $N \dots$  number of spins):

$$\Delta n = N \tanh \frac{\gamma_I \hbar B}{2k_B T} \approx \frac{N \gamma_I \hbar B}{2k_B T} \quad \text{with} \quad \gamma_I \hbar B \ll k_B T \quad (1.52)$$

With this difference we can calculate the total magnetization of an ensemble of  $\frac{1}{2}\text{H}$  nuclei:

$$\mathbf{M} = \Delta n \boldsymbol{\mu}_I \approx \frac{N \gamma_I \hbar}{2k_B} \cdot \frac{B}{T} \cdot \boldsymbol{\mu}_I \quad \text{with } B \dots \text{magnetic field strength} \quad (1.53)$$

Now we want to know how the magnetization changes in time. For this consideration we start with static magnetic field in z-direction:

$$\mathbf{B} = \begin{pmatrix} 0 \\ 0 \\ B_z \end{pmatrix} \quad (1.54)$$

The nuclear magnetic moment aligns to the magnetic field lines due to the following torque

$$\boldsymbol{\tau} = \boldsymbol{\mu}_I \times \mathbf{B} \quad (1.55)$$

The change of the nuclear spin  $\mathbf{I}$  in time is exactly the torque:

$$\boldsymbol{\tau} = \frac{d\mathbf{I}}{dt} \quad (1.56)$$

Using (1.55), (1.56) and (1.26) results into the equation of motion for the nuclear magnetic moment:

$$\frac{d\mathbf{m}_I}{dt} = \gamma_I \cdot \mathbf{m}_I \times \mathbf{B} \quad (1.57)$$

We have already seen that the total magnetization is proportional to the magnetic moment (see (1.53)) yielding

$$\frac{d\mathbf{M}}{dt} = \gamma_I \cdot \mathbf{M} \times \mathbf{B} \quad (1.58)$$

We can now split the magnetization vector into three equations, since the magnetic field is applied in z-direction, we get:

$$\begin{aligned}\frac{dM_x}{dt} &= \gamma_I M_y B_z \\ \frac{dM_y}{dt} &= -\gamma_I M_x B_z\end{aligned}\tag{1.59}$$

$$\frac{dM_z}{dt} = 0$$

We can solve these equations with the initial condition  $\mathbf{M}(0) = (M_{x,0}, M_{y,0}, M_{z,0})$  at  $t=0$ :

$$\begin{aligned}M_x(t) &= M_{x,0} \cos \omega_L t - M_{y,0} \sin \omega_L t \\ M_y(t) &= M_{x,0} \sin \omega_L t + M_{y,0} \cos \omega_L t \\ M_z(t) &= M_{z,0}\end{aligned}\tag{1.60}$$

These results are similar to the results we already obtained using quantum mechanics (see section 1.4), where we considered a single nuclear magnetic moment in a magnetic field). Here we investigated the magnetization vector. We see that the magnetization vector behaves similarly to the nuclear magnetic moment. It precesses in the x-y plane (perpendicular to the magnetic field) along the magnetic field with a constant z-component. The precession frequency is again the Larmor frequency. When we apply a radio-frequency field with the Larmor frequency  $\omega_L$  with the magnetic field strength  $B_{RF}$  perpendicular to the static magnetic field  $\mathbf{B}$  the time-dependent magnetic field  $\mathbf{B}(t)$  is:

$$\mathbf{B}(t) = \begin{pmatrix} B_{RF} \cdot \cos(\omega_L t) \\ B_{RF} \cdot \sin(\omega_L t) \\ B_z \end{pmatrix}\tag{1.61}$$

Now we have to solve the following equation of motion:

$$\frac{d\mathbf{M}}{dt} = \gamma_I \cdot \mathbf{M} \times \mathbf{B}(t)\tag{1.62}$$

We can again split the vector yielding three coupled differential equations:

$$\begin{aligned}\frac{dM_x}{dt} &= \gamma_I \cdot (M_y B_z + M_z B_{RF} \sin(\omega_L t)) \\ \frac{dM_y}{dt} &= \gamma_I \cdot (-M_x B_z + M_z B_{RF} \cos(\omega_L t)) \\ \frac{dM_z}{dt} &= \gamma_I \cdot (M_x B_{RF} \cos(\omega_L t) + M_y B_{RF} \sin(\omega_L t))\end{aligned}\tag{1.63}$$

The above equations are the Bloch equations (resting frame). The general solution of (1.63) is (with  $M_0$ ...magnitude of the magnetization):

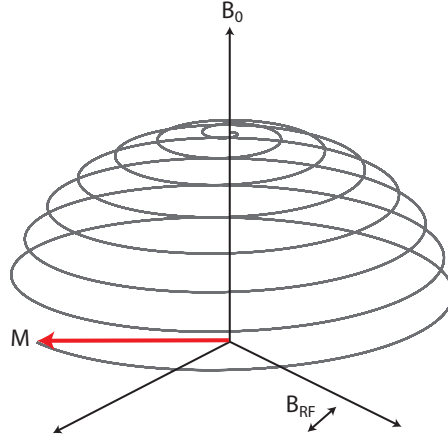


**Figure 1.5:** Excitation of magnetization vector while the radio-frequency field is applied. Plotted with gnuplot ([www.gnuplot.info](http://www.gnuplot.info)).

$$M_x(t) = M_0 \cdot \sin(\gamma_I B_{RF} t) \cdot \sin(\omega_L t)$$

$$M_y(t) = M_0 \cdot \sin(\gamma_I B_{RF} t) \cdot \cos(\omega_L t) \quad (1.64)$$

$$M_z(t) = M_0 \cdot \cos(\gamma_I B_{RF} t)$$

We now assume parallel magnetization to the static magnetic field (z-direction) at the time  $t = 0$  ( $M(t = 0) = (0, 0, M_z)$ ). Applying the radio-frequency field for the time  $0 \leq t \leq \frac{\pi}{2\omega_{RF}}$  with  $\omega_{RF} = \gamma_I B_{RF}$  we see using the general solution of the Bloch equations that after the time  $t = \frac{\pi}{2\omega_{RF}}$  the z-component of the magnetization has been flipped to the x-y plane and performs precession in this plane (flip angle  $90^\circ$ ). If the radio-frequency pulse was applied for the time  $t = \frac{\pi}{\omega_{RF}}$  the resulting magnetization vector would point in the negative z-direction (flip angle  $180^\circ$ ). An example excitation can be found in figure 1.5. We see that the duration of the radio-frequency (RF) pulse therefore defines the value of the so-called flip angle  $\theta$ :

$$\theta(t) = \omega_{RF} t = \gamma_I B_{RF} t \quad (1.65)$$

## 1.6 Relaxation

When the radio-frequency field is switched off, the magnetization decays to its initial state (state of thermal equilibrium). The return from the equilibrium state to equilibrium is called relaxation. The decay of the transversal magnetization  $M_{x,y}$  can be described as follows

$$\begin{aligned}\frac{dM_x}{dt} &= -\frac{1}{T_2} M_x \\ \frac{dM_y}{dt} &= -\frac{1}{T_2} M_y\end{aligned}\tag{1.66}$$

This relaxation process is the so-called transversal relaxation or  $T_2$  relaxation (see figure 1.6). The solution of equation (1.66) is

$$M_{x,y}(t) = M_{x,y}(0) \cdot \exp(-t/T_2) \quad \text{with} \quad M_{x,y}(0) \dots \text{initial magnetization} \tag{1.67}$$

Equation (1.66) describes how fast the transversal magnetization  $M_{x,y}$  decreases. Due to interaction between the single spins, the spins get out of phase and the magnetization is decreasing, because spins point in arbitrary directions in the x-y-plane. This dephasing process is characterized by the time constant  $T_2$ .

To measure the transversal relaxation time we need a coil perpendicular to the static magnetic field. The magnetization rotating in the x-y-plane induces voltage  $V(t)$  (see section 2.1) in the coil proportional to the magnetization  $M_{x,y}$ . This signal is the so-called free induction decay (FID) (see figure 1.6). Measuring the actual decay of the signal due to the transversal relaxation, we see that the signal decay is faster than expected in equation (1.67). This is due to inhomogeneities in the magnetic field, which further reduces the coherence of the magnetization. When we now combine the effects of the spin-spin relaxation and inhomogeneities in the magnetic field we get the time constant  $T_2^*$ . The transversal magnetization then decreases with

$$M_{x,y}(t) = M_{x,y}(t=0) \cdot \exp(-t/T_2^*).\tag{1.68}$$

A comparison between  $T_2$  and  $T_2^*$  can be seen in figure 1.6.  $T_2^*$  is smaller than  $T_2$ , the relation between both is

$$\frac{1}{T_2^*} = \frac{1}{T_2} + \frac{1}{T_2'}\tag{1.69}$$

with  $T_2'$  considering the relaxation due to static field inhomogeneities.

Another relaxation mechanism is the longitudinal relaxation. It describes the recovery of the longitudinal magnetization ( $M_z$ ). The spins can interact with the surroundings (so-called lattice) transferring energy. When the spin moves away from thermal equilibrium (e.g. due to an RF pulse),

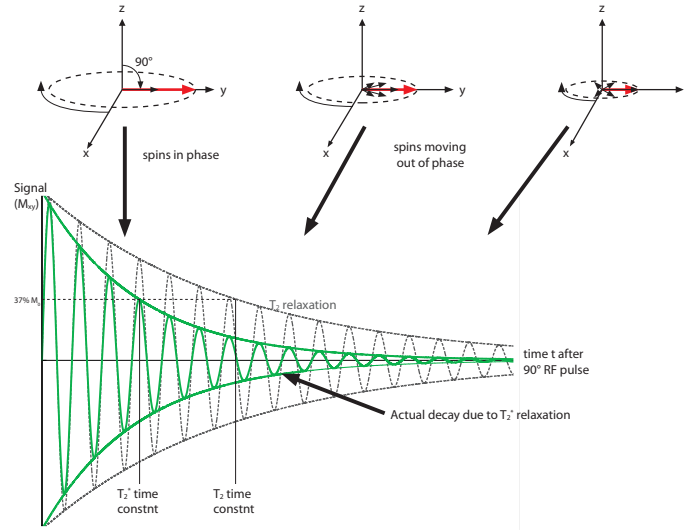


**Figure 1.6:**  $T_2$  relaxation after  $90^\circ$  RF- Pulse compared to  $T_2^*$  relaxation. When the radio-frequency (RF) field is switched on the magnetization flips to the x-y-plane. When the spins get out of phase the transversal magnetization  $M_{x,y}$  decreases. This decrease is due to spin-spin interactions. But the actual decrease we are measuring is due to  $T_2^*$  relaxation.

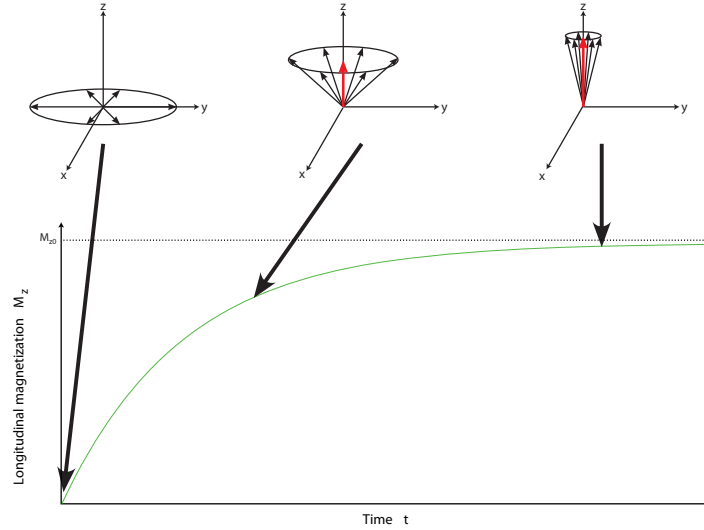


**Figure 1.7:**  $T_1$  relaxation after  $90^\circ$  RF- Pulse. When the radio-frequency (RF) field is switched on the magnetization flips to the x-y-plane. After the pulse the longitudinal magnetization recovers due to the longitudinal relaxation.



the spin will eventually recover yielding an increase in the longitudinal magnetization. With the recovery of the longitudinal magnetization the transversal magnetization decreases simultaneously. The relaxation takes place in a characteristic time, the so-called  $T_1$  relaxation time, which is longer than  $T_2$ . This process is called "spin-lattice relaxation". For the z-component of the magnetization vector we get

$$\frac{dM_z}{dt} = \frac{M_0 - M_z}{T_1} \quad (1.70)$$

with  $M_0$ , the magnitude of  $M_z$  in thermal equilibrium. The solution of this equation is

$$M_z(t) = M_0 \cdot (1 - 2 \cdot \exp(-t/T_1)) \quad (1.71)$$

The Bloch equations from (1.63) do not consider relaxation processes. Now we can modify the Bloch equations to additionally consider these relaxation processes:

$$\begin{aligned} \frac{dM_x}{dt} &= \gamma_I \cdot (M_y B_z + M_z B_{RF} \sin(\omega_L t)) - \frac{1}{T_2} M_x \\ \frac{dM_y}{dt} &= \gamma_I \cdot (-M_x B_z + M_z B_{RF} \cos(\omega_L t)) - \frac{1}{T_2} M_y \\ \frac{dM_z}{dt} &= \gamma_I \cdot (M_x B_{RF} \cos(\omega_L t) + M_y B_{RF} \sin(\omega_L t)) + \frac{M_0 - M_z}{T_1} \end{aligned} \quad (1.72)$$

The relaxation times depend on the tissue. In table 1.2 you find typical relaxation times for different tissues in the human body at 1.5 T.

| Tissue                                      | $T_1$ (ms)  | $T_2$ (ms) |
|---|-------------|------------|
| Adipose tissues                             | 240-250     | 60-80      |
| Whole blood (deoxygenated)                  | 1350        | 50         |
| Whole blood (oxygenated)                    | 1350        | 200        |
| Cerebrospinal fluid (similar to pure water) | 4200 - 4500 | 2100-2300  |
| Gray matter of cerebrum                     | 920         | 100        |
| White matter of cerebrum                    | 780         | 90         |
| Liver                                       | 490         | 40         |
| Kidneys                                     | 650         | 60-75      |
| Muscles                                     | 860-900     | 50         |

**Table 1.2:** Relaxation times for tissues in the human body at 1.5 Tesla [44].

## References

Additional literatures that have been used in this section are:

- W Demtröder. 2009. *Experimentalphysik 3 Atome, Moleküle und Festkörper*. Springer.
- H Haken, H C Wolf. 2005. *The physics of atoms and quanta: introduction to experiments and theory*. Springer.
- M H Levitt. 2008. *Spin Dynamics Basics of Nuclear Magnetic Resonance*. John Wiley & Sons Ltd.

## Chapter 2

# Magnetic Resonance Imaging

### 2.1 Signal Detection and Fourier Transform

Applying RF pulses in connection with a static magnetic yield a macroscopic magnetization and signals induced in a coil perpendicular to the magnetic field. The signal detection is based on the Faraday law. A time-dependent magnetic flux  $\Phi(t)$  through a conducting loop induces voltage  $V(t)$  in it. The Faraday law is:

$$V(t) = \frac{\partial \Phi(t)}{\partial t} \quad (2.1)$$

The magnetic flux is given by

$$\Phi(t) = \int_V \mathbf{B}_L(\mathbf{r}) \cdot \mathbf{M}(\mathbf{r}, t) d\mathbf{r} \quad (2.2)$$

with  $\mathbf{B}_L(\mathbf{r})$  being the magnetic field which is produced by the electrical current in the loop and with  $\mathbf{M}(\mathbf{r}, t)$  being the magnetization. Inserting (2.2) into (2.1) yields

$$V(t) = -\frac{\partial}{\partial t} \int \mathbf{B}_L(\mathbf{r}) \cdot \mathbf{M}(\mathbf{r}, t) d\mathbf{r} \quad (2.3)$$

In MRI, the Fourier transform is crucial. The Fourier transform of a spatially-dependent function  $\rho(x)$  is

$$S(k) = F\{\rho(x)\} = \int_{-\infty}^{\infty} \rho(x) e^{-i2\pi kx} dx \quad (2.4)$$

To recover  $\rho(x)$  the inverse Fourier transform must be applied on  $S(k)$ :

$$\rho(x) = F^{-1}\{S(k)\} = \int_{-\infty}^{\infty} S(k) e^{-i2\pi kx} dk \quad (2.5)$$

Some examples of Fourier transforms can be found in figure 2.1.

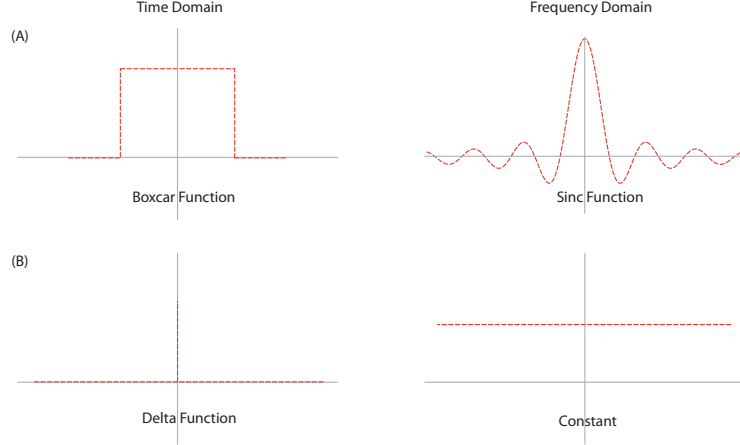


**Figure 2.1:** Examples of Fourier transforms. (A) Boxcar function vs. sinc function and (B) delta function vs. constant function.

## 2.2 Data Acquisition

The signal induced in the coil is generated by all parts of the object. This would be sufficient for a homogenous object. However in MRI this is seldom the case. For heterogeneous objects we need to differ spatial positions in the object. Therefore spatial localization is necessary. Spatial localization can be achieved by: (1) selective excitation and (2) spatial encoding.

### 2.2.1 Slice Selection

#### Slice-Selective RF Pulses

For slice-selection selective excitation is needed. To encode the spatial information it is necessary that the Larmor frequency of spins is position-dependent. The easiest way to accomplish this is to apply a linear gradient field besides the static magnetic field  $B_0$ :

$$\mathbf{B} = \mathbf{G} + B_0 \quad (2.6)$$

with  $\mathbf{G}$  being the gradient. To excite the spins selectively in this gradient field we need a slice-selective pulse. To create a slice-selective pulse design we use a Fourier transform. To illustrate this we chose a linear gradient  $G_z$  in z-direction. The function we have to deal with is a boxcar function (see figure 2.1 (A)). We assume the following slice in z-direction with the slice thickness  $\Delta z$  which is centered at  $z = z_0$

$$p(z) = \begin{cases} 1 & |z - z_0| < \Delta z/2 \\ 0 & \text{otherwise} \end{cases} = \Pi\left(\frac{z - z_0}{\Delta z}\right). \quad (2.7)$$

With this slice-selection the position-dependent Larmor frequency of the spins is:

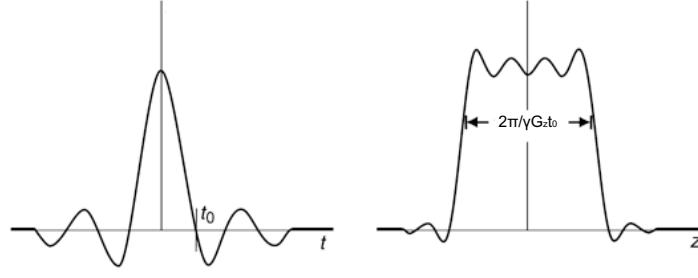


**Figure 2.2:** Truncation of RF pulse. Since a perfect sinc-pulse with an infinite duration is not realizable in an MR experiment, the pulse is truncated yielding a different slice-selection profile an example seen in this figure (from <http://www.currentprotocols.com>).

$$\omega(z) = \omega(z_0) + \gamma G_z z \quad \text{or} \quad f(z) = f(z_0) + 2\pi\gamma G_z z \quad (2.8)$$

Using (2.7) and (2.8) we get:

$$p(f) = \Pi\left(\frac{2\pi f}{\gamma G_z}\right) = \Pi\left(\frac{f - f(z_0)}{\Delta f}\right) \quad (2.9)$$

with  $\Delta f = 2\pi G_z \Delta z$ . The necessary frequency of the RF pulse is  $\omega_{RF} = 2\pi f(z_0) = \omega_0 + \gamma G_z z_0$ . Calculation of the Fourier transform of (2.9) yields

$$F(t) \propto \Delta f \cdot \text{sinc}(\pi \Delta f t) \cdot e^{-i2\pi f(z_0)t}. \quad (2.10)$$

We see that the pulse envelope  $B^e(t)$  of the slice-selective RF pulse is proportional to  $\text{sinc}(\pi \Delta f t)$ . However, such a sinc pulse is not physically realizable as RF pulses can only last for finite time periods. Assuming a symmetric pulse period with the duration  $\tau_p$

$$B^e(t) \propto \text{sinc}\left[\pi \Delta f \left(t - \frac{\tau_p}{2}\right)\right], \quad 0 \leq t \leq \tau_p \quad (2.11)$$

the slice-selection profile then is

$$p(f) = \Pi\left(\frac{f - f(z_0)}{\Delta f}\right) e^{i2\pi(f - f(z_0))\tau_p/2} \quad (2.12)$$

or

$$p(z) = \Pi\left(\frac{z - z_0}{\Delta z}\right) e^{i\gamma G_z (z - z_0)\tau_p/2} \quad (2.13)$$

An example of the so-called truncated pulses can be seen in figure 2.2. One example of possible slice-selections can be seen in figure 2.3. The gradients are applied in x-, y- and z-direction or sagittal, coronal and axial direction, respectively.

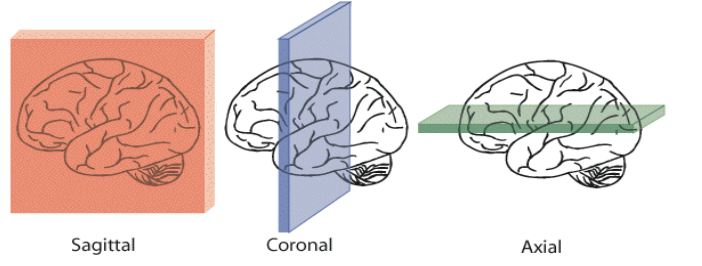


**Figure 2.3:** (a) sagittal slice (x-axis), (b) coronal slice (y-axis) and (c) axial slice (z-axis) [41].

### Rephasing Gradient

As a consequence of the gradient field  $G_z$ , an additional phase shift  $e^{i\gamma G_z(z-z_0)\tau_p/2}$  can be found in the slice. This phase shift results into a signal loss. To avoid this signal loss an additional refocusing gradient is applied in z-direction. This gradient compensates the phase shift. This method is called post-excitation rephasing. To calculate the rephasing gradient  $G_{r,z}$  needed, we require the phase angle during the rephasing period

$$\phi(z, t) = \gamma G_z(z - z_0)\tau_p + \gamma G_{r,z}(z - z_0)(t - \tau_p) \quad (2.14)$$

Assuming the duration of  $G_{r,z}$  to be  $\tau_r$ , the phase shift within the slice should vanish after the time  $\tau_p + \tau_r$ :

$$\phi(z, t = \tau_p + \tau_r) = 0 \quad \rightarrow \quad G_{r,z}\tau_r = -\frac{1}{2}G_z\tau_p \quad (2.15)$$

This condition can be fulfilled with the following relations:

$$\tau_r = \frac{\tau_p}{2} \quad \text{and} \quad G_{r,z} = -G_z \quad (2.16)$$

We see that the rephasing gradient needs the opposite polarity of the initial gradient and to be applied for the duration  $\frac{\tau_p}{2}$ .

### 2.2.2 Spatial Encoding

During acquisition we apply an additional gradient field  $G_x$  in x-direction. The precession is now dependent on the position in x-direction, yielding a frequency-encoded FID signal. To illustrate this we assume one slice with a certain spin distribution  $\rho(x)$ . The local FID signal then looks like

$$dS(x, t) \propto \rho(x)dx e^{-i\gamma(B_0 + G_x x)t} \quad (2.17)$$

The signal from the whole object then is

$$S(t) = \int_{Object} dS(x, t) \propto \int_{-\infty}^{\infty} \rho(x) e^{-i\gamma(B_0 + G_x x)t} dx = e^{-i\omega_0 t} \cdot \int_{-\infty}^{\infty} \rho(x) e^{-i\gamma G_x x t} dx. \quad (2.18)$$

with  $\gamma B_0 = \omega_0$ . Equation (2.18) can be generalized to:

$$S(t) \propto \int_V \rho(\mathbf{r}) e^{-i\gamma \mathbf{B}(\mathbf{r}) \mathbf{r} t} d\mathbf{r} \quad \text{with} \quad \begin{aligned} \mathbf{B}(\mathbf{r}) &= \mathbf{B}_0 + \mathbf{G} \\ \mathbf{G} &= (G_x, G_y, G_z) \end{aligned} \quad (2.19)$$

This gradient is the so-called frequency-encoding or readout gradient. Using this method we can encode spatial information only in one dimension (along the field gradient). For multidimensional spatial localization of signals further information is needed. Hence we apply an additional gradient  $G_y$  in y-direction for the time  $T_{PE}$  before data acquisition. The influence of the gradient on the local signal then is

$$dS(x, t) \propto \begin{cases} \rho(x) e^{-i\gamma(B_0 + G_y)t} & 0 \leq t \leq T_{PE} \\ \rho(x) e^{-i\gamma G_y T_{PE}} e^{-i\gamma B_0 t} & T_{PE} \leq t \end{cases} \quad (2.20)$$

During the time  $T_{PE}$  the spins receive different phase angles  $\phi$ . After the time  $T_{PE}$  the phase angle is:

$$\phi(x) = -\gamma G_y y T_{PE} \quad (2.21)$$

Hence this gradient is the so-called phase-encoding gradient. The time period in which the gradient is applied is called the phase-encoding interval.

Summarizing, spatial encoding is performed applying a phase-encoding gradient before data acquisition yielding a phase shift at different spatial positions followed by a frequency-encoding (readout) gradient during acquisition. Figure 2.4 shows the effects of the readout and phase-encoding gradient on the Larmor frequencies of spatially different located spins.

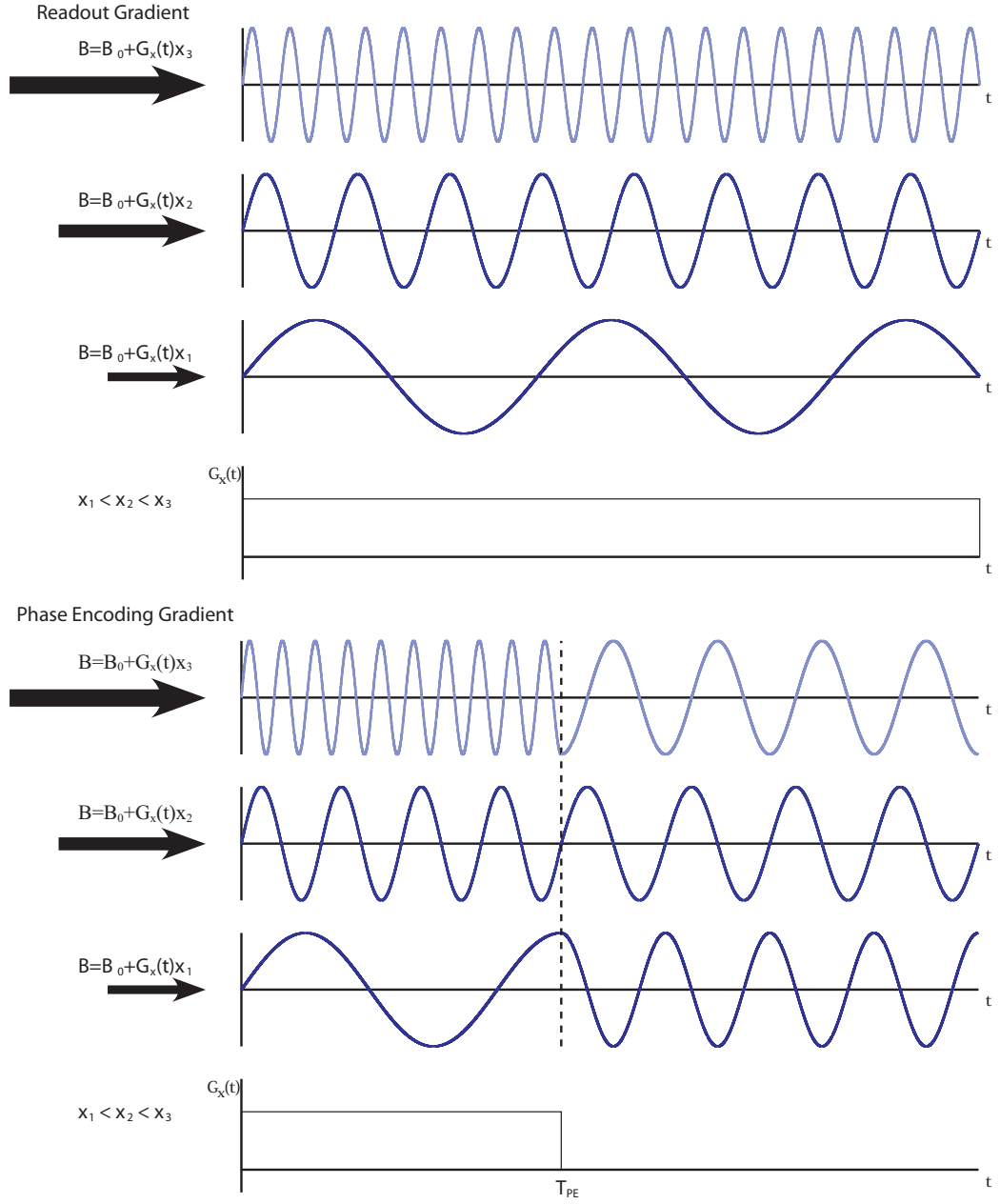


**Figure 2.4:** The upper figure shows the effect of the readout gradient on the Larmor frequencies. This gradient is applied during data acquisition yielding different precession frequencies at different spatial positions. The bottom figure shows the effect of the phase-encoding gradient. This gradient is applied for the time  $T_{PE}$  before data acquisition yielding a phase shift for different spatial positions.



### 2.2.3 k-space

The net magnetization flipped into the x-y-plane in an object induces a signal. The received signal in presence of a gradient field  $\mathbf{G}$  was introduced in equation (2.19) assuming a spin distribution  $\rho(r)$ . Transferring this spin distribution to the magnetization  $M(\mathbf{r})$  in the object, (2.19) becomes

$$S(t) \propto \int_V M(\mathbf{r}) \cdot e^{-i\gamma(B_0 + \mathbf{G}\mathbf{r})t} d\mathbf{r} \quad (2.22)$$

Here we are only interested in signals that have relevance for spatial encoding. Since  $e^{-i\gamma B_0 t}$  is spatially independent, we only consider  $e^{-i\gamma \mathbf{G}\mathbf{r}t}$ . We define  $\mathbf{k}$  as follows:

$$\mathbf{k} = \gamma \int \mathbf{G} dt \quad (2.23)$$

Using equation (2.22) and (2.23) we get

$$S(\mathbf{k}) \propto \int_V M(\mathbf{r}) \cdot e^{-i\mathbf{k}\mathbf{r}} d\mathbf{r}. \quad (2.24)$$

This equation is a Fourier transform. In section 2.1 we have already seen that to recover the signal as function of position we need to perform the inverse Fourier transform:

$$M(\mathbf{r}) \propto \int_{\mathbf{k}} S(\mathbf{k}) \cdot e^{i\mathbf{k}\mathbf{r}} d\mathbf{k} \quad (2.25)$$

De facto an inverse 2 or 3 dimensional Fourier transformation is needed. The acquired signal considering phase and frequency-encoding ( $G_p$  and  $G_f$ , respectively) can then be described as follows [32]:

$$S(k_f, k_p) = \int \int S(x, y) e^{i(k_f x + k_p y)} dx dy \quad (2.26)$$

with

$$k_f(t) = \gamma \int_0^t G_f(t') dt' \quad (2.27)$$

$$k_p(t) = \gamma \int_0^t G_p(t') dt' \quad (2.28)$$

This inverse Fourier transform then is calculated as follows:

$$S(x, y) = \int \int S(k_f, k_p) \cdot e^{i(k_f x + k_p y)} dk_f dk_p \quad (2.29)$$

The coordinate system in which the MR signal is detected is the so-called k-space, with  $k_p$  as vertical axis and  $k_f$  as horizontal axis. When an MR image is acquired the k-space is filled with data. During the application of gradients the detected signal follows a trajectory in k-space. The  $k_f$  coordinate is proportional to  $G_f$  (see equation (2.27)). When  $G_f$  is applied the trajectory moves horizontally. The coordinate  $k_p$  is proportional to  $G_p$  (see equation (2.28)). When  $G_p$  is

applied the trajectory moves along  $k_p$ . The velocity of the trajectory is proportional to the gradient strength. Prephasing frequency and phase-encoding gradients can be applied to define the starting point of the first trajectory in k-space. Two example trajectories can be found in figure 2.5.

Points in close proximity of the origin of the k-space provide low-resolution information and determine the signal-to-noise ratio of the final image. Points in outer k-space regions contain information on small features, which can be seen in figure 2.6.

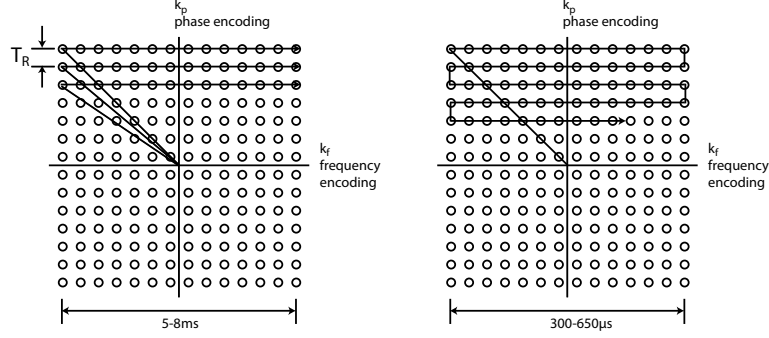


**Figure 2.5:** k-space trajectories. In the left image a line is measured for every  $T_R$ . After the line is acquired the signal is reformed and a new phase-encoding gradient is applied, yielding a new line. In the right image we see a typical EPI sequence. After every readout line a new phase-encoding gradient is applied. In this sequence the data acquisition of the readout line must be fast enough that all lines can be measured while the MR signal is still present, therefore the acquisition time for each line is smaller, this needs strong gradient fields.

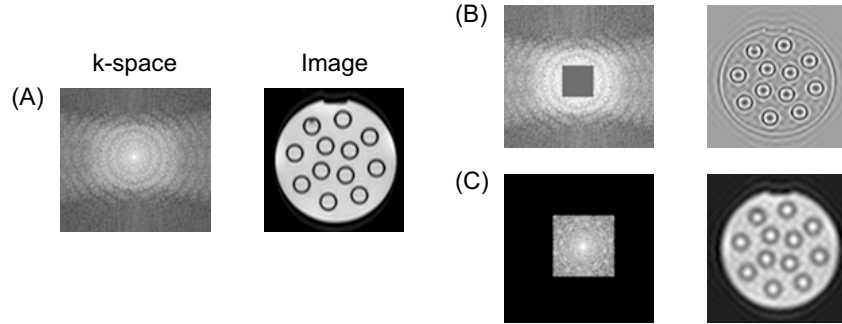


**Figure 2.6:** This figure shows the effects of missing k-space data. This case is simulated by setting distinct points zero as shown in the left column indicated with a black box. (A) contains the whole k-space. (B) The center is set zero, the image only contains small structures. (C) The periphery is set zero yielding a low-resolution image containing contrast information. Figure modified from [31].

## 2.3 MRI Sequence

An MRI sequence is a combination of pre-selected RF and gradient pulses. In the following two basic sequences will be introduced.

### 2.3.1 Spin Echo Sequence

A simple sequence is the so-called spin echo sequence. With this sequence it is possible to estimate the  $T_2$  parameters. A spin echo is created by a  $90^\circ$  pulse at  $t=0$  with a subsequent  $180^\circ$  pulse at  $t=\tau$ . After the first excitation pulse the longitudinal magnetization is rotated to the x-y-plane. The transversal magnetization decays due to dephasing of the spins caused by spin-spin interactions and static magnetic field inhomogeneities. The second excitation pulse flips the spins along one axis in the x-y plane. Since the inhomogeneities are static, the effect of the field inhomogeneities which led to a dephasing before, rephase the spins and a spin echo can be measured at  $t = 2\tau$ . The signal, however, is attenuated. The dephasing due to spin-spin relaxation is not revoked and therefore the signal strength decreases with the time-constant  $T_2$  and not  $T_2^*$  (Signal attenuation is  $e^{-2\tau/T_2}$ ), see also figure 2.7. The full signal can be regained by applying another  $90^\circ$  pulse. The time between two  $90^\circ$  pulses is the so-called repetition time  $T_R$ . The time  $2\tau$  is the so-called echo time  $T_E$ .

Physically we can say that the spins rotate with different frequencies ( $\omega_s$ ...slow rotating and  $\omega_f$ ...fast rotating spins). The spins dephase due to static inhomogeneities and spin-spin interaction and after the time  $\tau$  they have the following phase difference  $\phi = (\omega_f - \omega_s) \cdot \tau$ . When the  $180^\circ$  pulse is applied the spins flip in the x-y-plane along one axis. Since the spins still rotate with the same frequency the fast spins catch up with the slow spins. At  $t = 2\tau$  the spins are rephased and a spin echo can be measured (see figure 2.7).

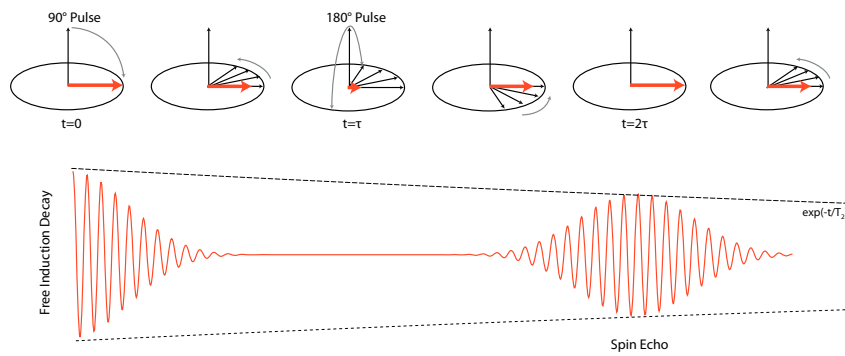


**Figure 2.7:** Spin echo sequence. A  $90^\circ$  pulse is applied and the magnetization is flipped to the x-y-plane. Due to dephasing of the spins, the magnetization is decaying. After  $T_E/2$  a  $180^\circ$  pulse is applied. The spins rephase and a spin echo can be measured at the time  $2\tau$ . The signal is attenuated due to spin-spin interaction ( $e^{-2\tau/T_2}$ ).

### 2.3.2 Echo-Planar Imaging

Echo-planar imaging (EPI) is an ultra fast imaging technique introduced by Mansfield in 1977. All points in k-space are acquired from one FID signal, therefore this sequence can provide high temporal resolution which are important e.g. for functional MRI experiments. The spatial resolution, however, is limited.

One common EPI sequence applies a  $90^\circ$  slice-selective RF pulse. Prephasing readout and phase-encoding gradients are applied which define the starting point of the k-space trajectory. For data acquisition the readout gradient is applied with alternating polarity. This causes the spins to rotate with  $\pm\omega$ . The spins are dephased and subsequently rephased resulting in a signal increase (see figure 2.8). The changing polarity of the readout gradient leads to positive and negative velocities in k-space which can be seen in figure 2.5. Phase encoding gradients are applied for a very short time between two readout gradients with different polarity, these pulses are called "blips". These "blips" move the k-space trajectory from line to line. The data acquisition time for the whole k-space is between 50 to 100ms. Therefore, strong gradient fields are needed, since the velocity of the trajectory in k-space is dependent on the gradient strength.

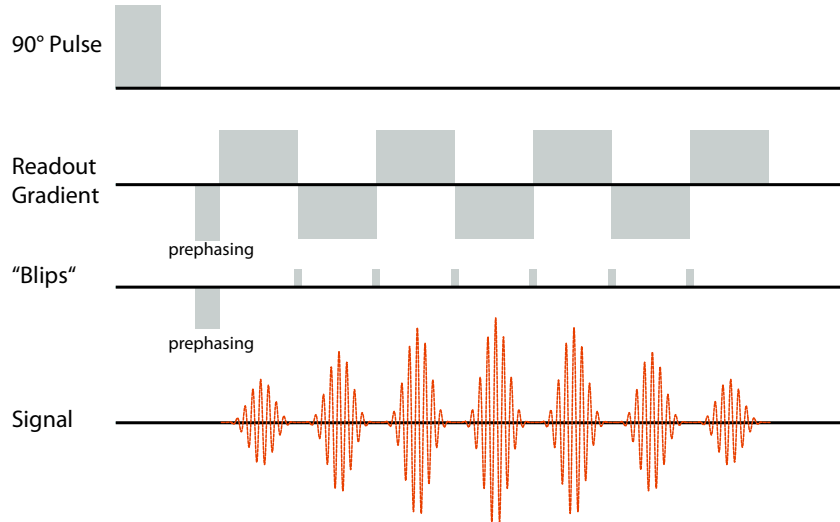


**Figure 2.8:** EPI sequence. After excitation prephasing gradients are applied. Subsequently readout gradient are applied with changing polarity. Gradient "blips" are applied for a very short time between readout gradients.

## 2.4 Artifacts

The following section will give a brief overview on problems encountering during MR imaging namely image distortions and artifacts. This overview is limited to the most common image artifacts such as aliasing, chemical shift and motion artifacts.

### 2.4.1 Chemical Shift Artifact

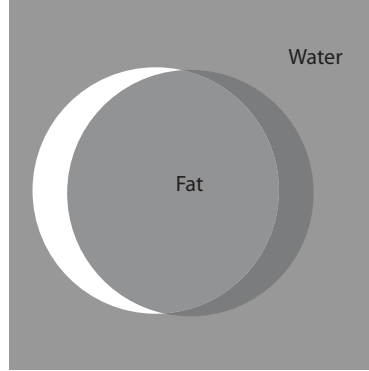


**Figure 2.9:** Misregistration due to chemical shift. The fat signal is shifted to lower frequencies [20].

This artifact originates from different chemical environments. The Larmor frequency of protons in fat tissue is shifted to lower frequencies compared to protons in water. This shift in the frequency yields a misregistration of fat and water protons. The signal of the spins with the shifted Larmor frequency are registered in the wrong position (see figure 2.9). The frequency shift is

$$\Delta\omega_c = \gamma\delta B_0 \quad (2.30)$$

with  $\delta$  the shielding constant which considers the "effective" magnetic field and  $B_0$  the static homogenous magnetic field. The frequency bandwidth of a voxel is

$$\Delta\omega_x = \gamma G_x \Delta x \quad (2.31)$$

using the Larmor frequency  $\omega = \gamma B$  and the linear gradient field  $G_x$ . The chemical shift in x-direction then is

$$\delta_c = \frac{\Delta\omega_c}{\Delta\omega_x} = \frac{\delta B_0}{G_x \Delta x} \quad (2.32)$$

The spatial shift then is:

$$\Delta x_c = \delta_c \Delta x = \frac{\delta B_0}{G_x} \quad (2.33)$$

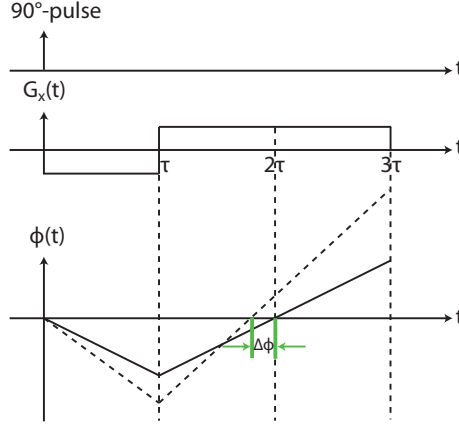


**Figure 2.10:** Typical frequency-encoding period. Dashed line shows effects of motion in the frequency-encoding direction yielding a different phase shift than compared to no motion (black line) [20].

To reduce this artifact strong readout gradients can be used, since the spatial displacement is proportional to  $\frac{1}{G}$ . Another way to improve image quality is to use fat suppression techniques, where a fat saturation pulse excites fat protons prior to the data acquisition, so that the signal from fat protons is already saturated before excitation of all other protons.

### 2.4.2 Flow Artifacts

During an ideal MR measurement the object measured should be stationary. As soon as living organisms (blood flow, heart beat, breathing, coughing, etc. ) are involved this is no longer possible resulting in flow artifacts such as blurring and spatial distortions. In the following a brief introduction to flow induced artifacts is given.

#### Flow Effects along Frequency Encoding Gradient

Object motion during frequency-encoding might lead to phase shifts. Assuming a frequency-encoding gradient  $G_x$  in x-direction for the time  $t$  and a displacement  $x(t)$  in the same direction, the phase shift of the spins is

$$\begin{aligned}\phi_F &= \gamma \int_0^t G_x(t') x(t') dt' = \gamma \int_0^t G_x(t') (x_0 + v_x t') dt' = \\ &= \gamma x_0 \int_0^t G_x(t') dt' + \gamma \int_0^t G_x(t') v_x t' dt'\end{aligned}\tag{2.34}$$

The first term represents the desired spatial encoding. In addition we get the latter term, which includes the additional phase shift due to the motion

$$\phi_F(t) = \gamma \int_0^t G_x(t') v_x t' dt' = -\frac{1}{2} \gamma G_x v_x t^2\tag{2.35}$$

During the period  $\tau \leq t \leq 3\tau$  (see figure 2.10) data acquisition is performed resulting into

$$\phi_F = \Delta\phi(\tau) + \gamma \int_{\tau}^t G_x(t') v_x t' dt' = \frac{1}{2} \gamma G_x v_x (t^2 - \tau^2) \quad (2.36)$$

The echoes peak is at  $t = T_E = 2\tau$  yielding

$$\phi_F = \gamma G_x v_x \tau^2 \quad (2.37)$$

Due to this shift, the spins are not completely rephased. Figure 2.10 shows the above calculated phase shift. Imaging effects resulting from this are for instance spatial shift and blurring.

### Flow Effects along the Phase Encoding Direction

For motion effects along the phase-encoding direction we again use equation (2.34). We apply the phase-encoding gradient  $G_P$  at the time  $T_P$  in y-direction with the duration  $\tau$  yielding

$$\phi_P = \gamma \int_{t_P}^{t_P+\tau} G_P(x_0 + v_x t) dx = \gamma x \tau + \gamma G_P v_x \tau (t_P + \tau/2) \quad (2.38)$$

Compared to equation (2.37) we get a different phase shift:

$$\phi_P = \gamma G_P v_x \tau (t_P + \tau/2) \quad (2.39)$$

Consequences of this motion are e.g. spatial misregistration.

### 2.4.3 Aliasing Artifacts

Aliasing artifacts arise when the k-space is not fully measured (undersampled). In information theory the Nyquist theorem states the following [10]: function  $x(t)$  is completely determined if  $x(t)$  contains frequencies in the range  $[f_{min}, f_{max}]$  and the sampling rate is  $f_s \geq 2(f_{max} - f_{min})$ .  $f_s$  is the so-called Nyquist frequency. Figure 2.11 shows a measured signal with two different sampling frequencies, one meeting this Nyquist criterion, the other violating it. In MRI an undersampling of the k-space leads to a wrapping-around of the object (see figure 2.12). Aliasing artifacts should be prevented because a post-measurement solving of this problem is in general very difficult. It can be prevented for instance by choosing adequate sampling rates.



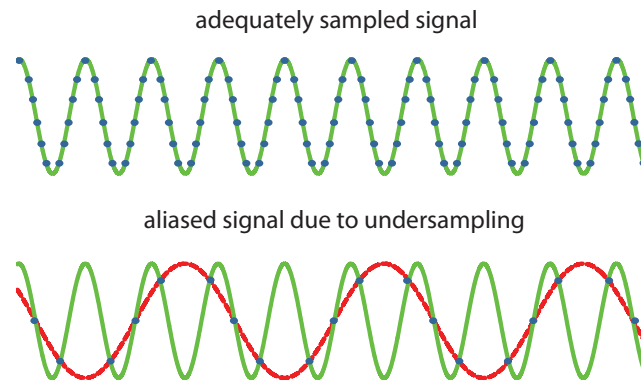


**Figure 2.11:** Aliasing due to undersampling. In the upper figure you see a signal measured with an adequate sampling frequency ( $f_s > f_{Nyquist}$ ). In the bottom figure you see the same signal with a sampling frequency not meeting the Nyquist criterion, therefore the reconstructed signal does not represent the original signal.

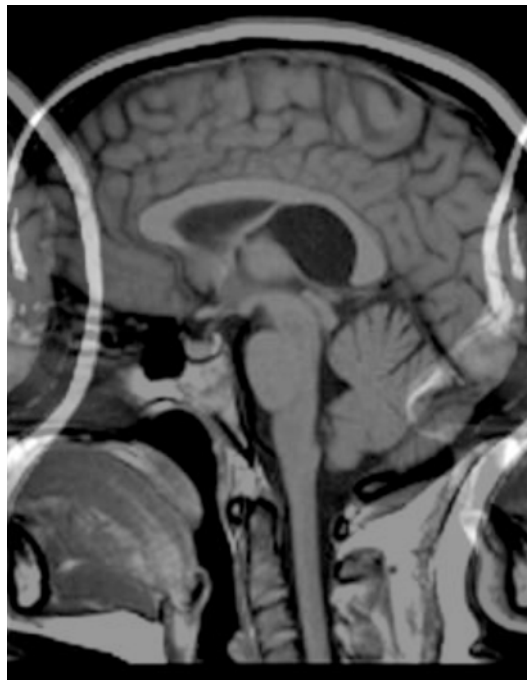


**Figure 2.12:** Aliased MR image due to undersampling.

## References

Additional literatures that have been used in this section are:

- Z-P Liang, P C Lauterbur. 1999. *Principles of Magnetic Resonance Imaging - A Signal Processing Perspective*. Wiley-IEEE Press.
- F Schmitt, M K Stehling, R Truner. 1998. *Echo-Planar Imaging: Theory, Technique and Application*. Springer.

## Chapter 3

# Diffusion Tensor Imaging

### 3.1 Diffusion

From a theoretical point of view Adolf Fick in 1855 was the first to describe diffusion [17]. One of Fick's laws illustrates that the cause of diffusion processes is due to a difference in the concentration:

$$\mathbf{J} = -D\nabla C \quad (3.1)$$

$\mathbf{J}$  is the net particle flux,  $D$  the diffusion coefficient (an intrinsic property) and  $C$  is the particle concentration. This means that particles move from areas with high concentration to areas with low concentration. We can also see that when the concentration difference vanishes, diffusion stops. But this is only on a macroscopic scale. From a microscopic point of view diffusion persists, as on molecular scale the movement is solely due to collisions between particles.

The seminal studies of Robert Brown showed that pollen grains under a microscope particles moved randomly without seeing an obvious cause (1828) [17]. He first believed that this was a sign of life, but later he proved himself wrong presenting the same result when observing dust particles.

Finally in the beginnings of the 20<sup>th</sup> century Albert Einstein stated, without knowing Brown's work, that particles (microscopically visibly) in a liquid will perform movements that can be observed in a microscope. His intention behind this was to prove the existence of atoms [17]. Describing the motion of particles undergoing diffusion with a probabilistic framework he finally combined Brown's and Fick's pictures. Further, Einstein described the displacement using a distribution of a group of particles. The mean square displacement of particles is stated as follows [17]:

$$\langle R^2 \rangle = \sigma^2 = 2Dt \quad (3.2)$$

Free diffusion follows a Gauss distribution [23]:

$$P = \frac{1}{\sigma\sqrt{2\pi}} e^{-x^2/2\sigma^2} \quad (3.3)$$

With this Gauss function we can calculate the water population at a certain time point  $t$  and position  $x$  [23]:

$$P(x, t) = \frac{1}{\sigma\sqrt{4\pi Dt}} e^{-x^2/4Dt} \quad (3.4)$$

We see that the distribution width will increase with longer  $t$ . For a fixed  $t$ , the distribution width will increase with higher diffusion constants  $D$ .

A technique that can be used to quantify this diffusion process is diffusion tensor imaging (DTI) [19, 22, 23]. With DTI, diffusion can be observed non-invasively in-vivo. The diffusion processes we are interested in MRI are on molecular scale and they are far beyond the usual resolution of MRI. Typical acquisition times are around 50 *ms* and the average distance a molecule travels in that time is around 10  $\mu m$ . In the brain or in muscles the molecules interact with tissue components such as fibers, macromolecules and cell membranes. In this case diffusion is not isotropic anymore and this anisotropy can now be observed. Considering myelin-sheathed neuron fibers, the diffusion is restricted perpendicular to the myelin sheaths that surround the axons and we can observe diffusion inside these sheaths. An average voxel of DTI images has a volume of some  $mm^3$ , therefore only the overall effect of the diffusion of all fibers in this voxel can be observed, not the diffusion within a single fiber.

## 3.2 Basics of Diffusion Tensor Imaging

At the beginning of the diffusion-weighted sequence we have a  $90^\circ$  RF excitation pulse that flips the spins in the x-y-plane. A gradient field with a certain strength is applied between  $t_1$  and  $t_2$ , along this gradient direction the spins do not precess with the same Larmor frequency and the transversal magnetization is thus attenuated. At  $t_3$  the same gradient field is again applied but this time with opposite polarity. Because of this opposite polarity the spins rephase and a signal can be measured. The gradient is turned off at  $t_4$ . Therefore, the first gradient pulse is called "dephasing" and the second "rephasing" gradient. The rephasing pulse has not the same effect on the spins that moved and they are not fully rephased. Therefore they do not contribute to the spin echo signal anymore; the signal is attenuated. However,  $T_2$  relaxation effects also attenuate the signal. To estimate only the effects of diffusion,  $T_2$  effects must be quantified (measurement without gradient field). Figure 3.1 and figure 3.2 show the principle of diffusion weighted sequences.

A great advantage is that diffusion is intrinsic, i.e. it is independent of magnetic fields or MR effects. To calculate the effects of diffusion on the MR signal we need (1) the travelled average distance ( $\sigma$ ), (2) the distribution of water molecules at a certain time point and position (see equation (3.4)) and (3) the phase shift due to diffusion. We already know  $\sigma$  (see equation (3.2)) and the population  $P(x, t)$ . For the phase shift we consider a water sample and apply a static

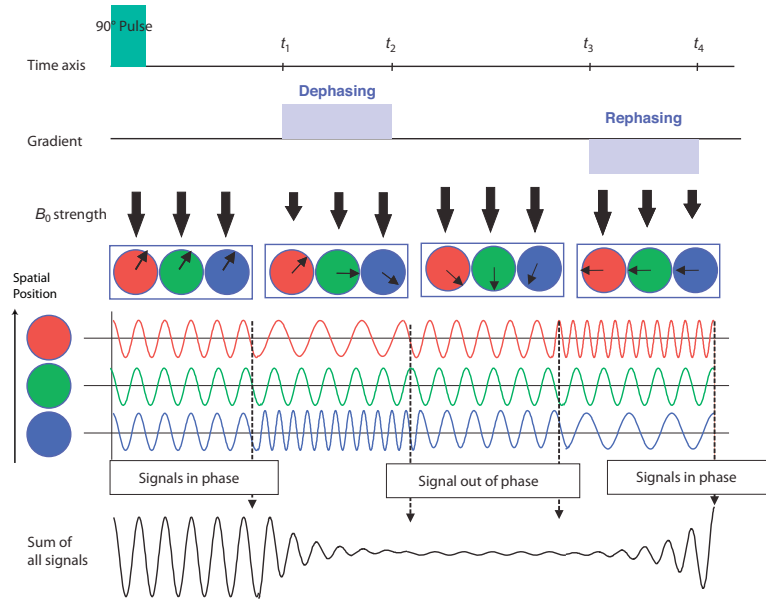


**Figure 3.1:** Basics of diffusion measurement. A strong static magnetic field  $B_0$  is applied in z-direction. A  $90^\circ$  pulse flips the spins to the x-y-plane. All spins have the same precession frequency. After the time  $t_1$  a dephasing pulse is applied (switch off at  $t_2$ ). In this figure we can see how the dephasing pulse yields different precession frequencies of the spins, the spins get out of phase and the signal vanishes. At  $t_3$  a rephasing pulse is applied. When the spins did not change their position, the rephasing pulse brings the spins back in phase and the full signal can be measured. Figure taken from [23]

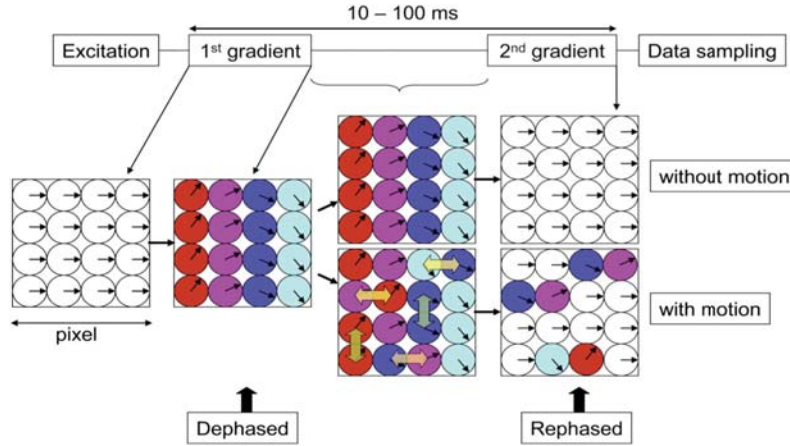


**Figure 3.2:** Basics of diffusion measurement. The upper row shows the case of no diffusion. In this case the rephasing pulse focuses all spins. In the lower row diffusion is allowed. In this case the dephasing and rephasing gradient are in z-direction (the color implies different Larmor frequencies due to the gradient). If spins change their position vertically this would not affect the signal, but when they change their position horizontally the rephasing gradient does not have the same effect on the spins due to their different phase shift resulting from the first dephasing pulse. Figure modified from [25].

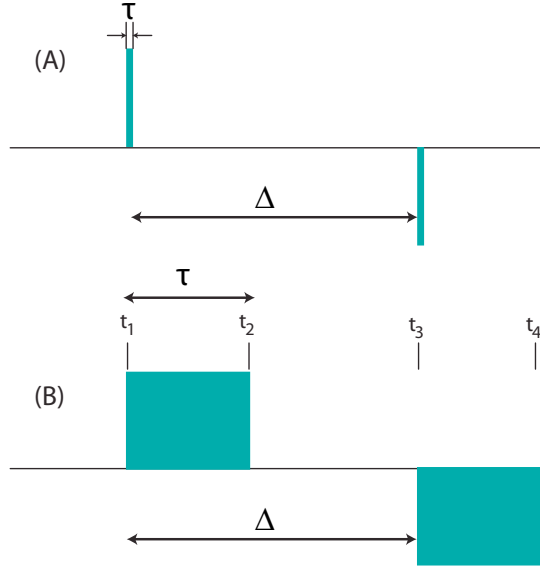


**Figure 3.3:** (A)  $\tau \ll \Delta$ . Diffusion during gradient pulse can be neglected (B) Realistic diffusion gradients. Diffusion during gradient pulse cannot be neglected. Modified from [23].

magnetic field (magnitude  $B_0$ ) and a linear field gradient in x-direction (magnitude  $G_x = \frac{dB_z}{dx}$ ), the position-dependent precession frequency of the proton spins then is:

$$\omega = \gamma(B_0 + G_x x) \quad (3.5)$$

Assuming that one water molecule diffuses in x-direction we get the time-dependent position  $\eta(t) = \eta_0 + \delta(t)$  with  $\eta_0$  being the mean position of the proton and  $\delta(t)$  the displacement. For the time period  $t_1 \leq t \leq t_2$  we apply the gradient  $G_x$  (dephasing gradient) and the proton spin receives the following phase angle:

$$\phi = \int_{t_1}^{t_2} \omega = \gamma \int_{t_1}^{t_2} G_x \eta(t) dt = \gamma \int_{t_1}^{t_2} G_x (\eta_0 + \delta(t)) dt \quad (3.6)$$

After the time period  $\Delta$  ( $t_2 \leq \Delta \leq t_3$ , the gradient is applied for the time  $t_3 \leq t \leq t_4$  with the opposite polarity (rephasing gradient), the phase angle then is:

$$\phi = \gamma G_x \left[ \int_{t_1}^{t_2} \delta(t) dt - \int_{t_3}^{t_4} \delta(t) dt \right] \quad (3.7)$$

If the duration of the gradient  $\tau$  ( $t_1 \leq \tau \leq t_2$ ) is much smaller than  $\Delta$ , we can neglect diffusion of the molecules during the gradient pulse. If the proton did not move during  $\Delta$  the resulting phase would be zero. However protons diffuse yielding a finite phase angle  $\phi$ . Without proof the phase shift is  $\phi(x) = e^{i\gamma G \tau x}$  [23], with  $x$  the position in x-direction,  $G$  being the gradient strength and  $\tau$  its duration. Taking all together the total signal is

$$\sum_x P(x, t) \phi(x) \rightarrow \frac{1}{\sigma \sqrt{4\pi D \Delta}} \int_x e^{-x^2/4D\Delta} e^{i\gamma G \tau x} dx \quad (3.8)$$

If no gradient is applied equation (3.8) is equal 1. However, equation (3.8) can be calculated as:

$$S = \frac{1}{\sigma \sqrt{4\pi D \Delta}} \left[ \int_{-\infty}^{\infty} e^{-x^2/4D\Delta} \cos(\gamma G \tau x) dx - i \int_{-\infty}^{\infty} e^{-x^2/4D\Delta} \sin(\gamma G \tau x) dx \right] \quad (3.9)$$

Due to symmetry the latter integral is zero. The result of the first integral is

$$S(t) = S(0) e^{-\gamma^2 G^2 \tau^2 D t} \quad (3.10)$$

To derive equation (3.10) we assumed  $\tau \ll \Delta$ , but this assumption is not valid for practical situations (see figure 3.3), where the gradient duration is typically between 5-30 *ms*. Therefore, diffusion effects during the application of the gradient cannot be neglected. The phase shift then is  $\phi(x, t) = e^{i\gamma G(t)tx}$  yielding

$$\int_x P(x, t) \phi(x, t) dx = \frac{1}{\sigma \sqrt{4\pi D t}} \int_x e^{-x^2/4Dt} e^{i\gamma G(t)tx} dx. \quad (3.11)$$

In addition we need to integrate over time to yield the signal intensity:

$$S(t) = S(0) e^{-\gamma^2 D \int_{t_1}^{t_4} \left( \int_0^t G(t') dt' \right)^2 dt} \quad (3.12)$$

or

$$\ln \left( \frac{S(t)}{S(0)} \right) = -\gamma^2 D \int_{t_1}^{t_4} \left( \int_0^t G(t') dt' \right)^2 dt \quad (3.13)$$

A typical time course of  $G(t)$  can be seen in figure 3.4. With this time course we can integrate equation (3.12)

$$\int_{t_1}^{t_2} G^2 t^2 dt + \int_{t_2}^{t_3} G^2 \tau^2 dt + \int_{t_3}^{t_4} (G\tau + G(t - t_3))^2 dt \quad (3.14)$$

Setting  $t_1 = 0$ ,  $t_2 = \tau$ ,  $t_3 = \Delta$  and  $t_4 = \tau + \Delta$  yields:

$$\int_0^{\tau} G^2 t^2 dt = \frac{G^2 \tau^3}{3} \quad (3.15)$$

$$\int_{\tau}^{\Delta} G^2 \tau^2 dt = G^2 \tau^2 (\Delta - \tau) = G^2 \tau^2 \Delta - G^2 \tau^3 \quad (3.16)$$

$$\int_{\Delta}^{\Delta+\tau} (G\tau + G(t - \Delta))^2 dt = \frac{G^2 \tau^3}{3} \quad (3.17)$$

The total signal then is

$$\ln \left( \frac{S(t)}{S(0)} \right) = -\gamma^2 G^2 \tau^2 \left( \Delta - \frac{\tau}{3} \right) D = -bD \quad (3.18)$$

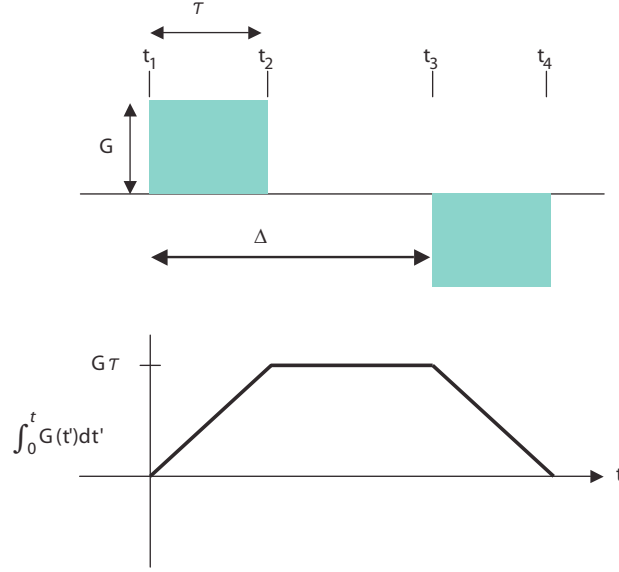


**Figure 3.4:** Time course of diffusion gradients. The bottom figure shows the acquired phase angle as function of time. Modified from [23].

$$S(t) = S(0) \cdot e^{-bD} \quad (3.19)$$

with  $b$  being the b-factor. This factor characterizes the gradient pulse. Higher b-values indicate stronger diffusion weighting. The higher the b-value is the higher is the diffusion weighting. In general, diffusion does not only occur in one direction. To be able to approximate the diffusion in 3 dimensions, we can use a tensor formalism:

$$\bar{D} = \begin{pmatrix} D_{xx} & D_{yx} & D_{zx} \\ D_{xy} & D_{yy} & D_{zy} \\ D_{xz} & D_{yz} & D_{zz} \end{pmatrix} \quad (3.20)$$

$\bar{D}$  is assumed to be symmetric ( $D_{ij} = D_{ji}$ ). Therefore at least 6 directions must be measured to estimate the diffusion tensor  $D$ . The diffusion tensor describes the diffusion pattern at each voxel in the brain representing an ellipsoid, the eigenvectors being the radii. The eigenvectors also represent the mean diffusion directions. A sphere then represents totally isotropic diffusion. To extract information from the DTI data, parameters are derived from the diffusion tensor already estimated by measuring in different direction. The trace is equal to the sum of the eigenvalues.

$$Tr(\bar{D}) = D_{xx} + D_{yy} + D_{zz} \text{ or } \lambda_1 + \lambda_2 + \lambda_3 \quad (3.21)$$

Dividing the trace by three results in the mean diffusivity.



$$MD = \frac{D_{xx} + D_{yy} + D_{zz}}{3} \text{ or } MD = \frac{\lambda_1 + \lambda_2 + \lambda_3}{3} \quad (3.22)$$

The fractional anisotropy is a scalar between 0 and 1 that describes the degree of anisotropy, 0 representing isotropy and 1 total anisotropy.

$$FA = \frac{\sqrt{3((\lambda_1 - \lambda)^2 + (\lambda_2 - \lambda)^2 + (\lambda_3 - \lambda)^2)}}{\sqrt{2(\lambda_1^2 + \lambda_2^2 + \lambda_3^2)}} \quad (3.23)$$

with  $\lambda = (\lambda_1 + \lambda_2 + \lambda_3)/3$ . The volume ratio (VR) is the ratio of the volume of the ellipsoid to the volume of a sphere with  $\lambda$

$$VR = \frac{\lambda_1 \lambda_2 \lambda_3}{\lambda^3} \quad (3.24)$$

And finally the relative anisotropy (RA), stating the ratio between anisotropic part of diffusivity to the isotropic part, it varies between 0 and  $\sqrt{2}$ :

$$RA = \frac{\sqrt{(\lambda_1 - \lambda)^2 + (\lambda_2 - \lambda)^2 + (\lambda_3 - \lambda)^2}}{\sqrt{3}\lambda} \quad (3.25)$$

### 3.3 Fractional Anisotropy

FA is a value between 0 and 1. 0 means total isotropy and 1 diffusion only in one direction (total anisotropy). When we look at the human brain FA is close to 0 in cerebrospinal fluid (CSF), grey matter has an FA value of approximately 0.2 and in white matter FA reaches its maximum (around 0.8) [23]. A mean FA image of 15 healthy subjects can be seen in figure 3.5. When we calculate FA we use the eigenvalues of the diffusion tensor. This diffusion tensor can be represented by an ellipsoid, a perfect sphere representing isotropic diffusion like in CSF, a slightly flatted ellipsoid for grey matter and a very elongated ellipsoid representing white matter. Now we know the grade of anisotropy but not the direction of the diffusion. A very useful representation of the diffusion direction is a color-encoded representation. Therefore we only take the main diffusion direction and give three directions colors (left-right in red, anterior-posterior in green, superior-inferior in blue). All other directions yield a superposition of the three main colors. Mori and colleagues [25] have summarized this information in the following figure 3.7.

An example of such a color encoding can be seen in figure 3.6, this figure shows an axial slice of a healthy single subject. From the same subject we can also show the main diffusion directions directly in form of vectors (see fig. 3.6). This information can be used for fiber tractography.

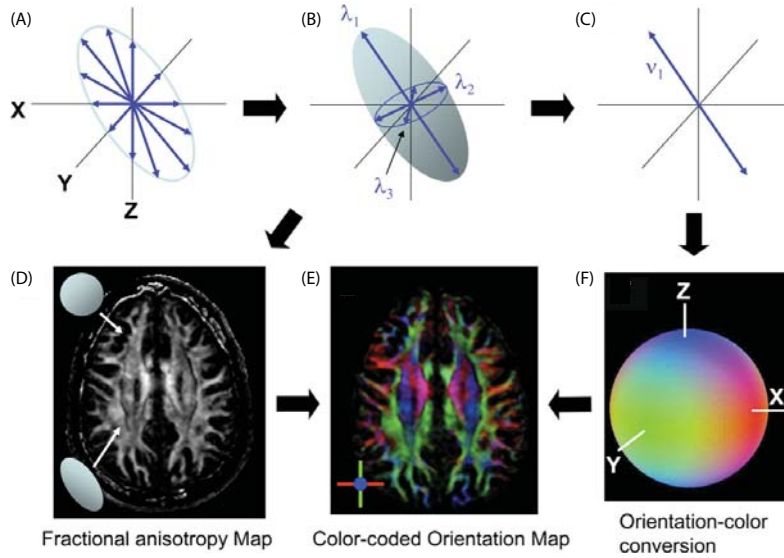


**Figure 3.7:** (A) shows the approximation of the diffusion tensor, several measured directions are indicated (B) shows the estimated diffusion tensor represented by the diffusion ellipsoid, the three main diffusion axis are drawn in with the corresponding eigenvalues  $\lambda_1$ ,  $\lambda_2$  and  $\lambda_3$ . (C) shows the main diffusion axis with the largest eigenvalue. (D) shows an FA image with typical ellipsoids for grey matter (nearly spherical ellipsoid) and white matter images (elongated ellipsoid). (E) show the color encoding for the same FA image which converted the information given by the diffusion tensor to colors (left-right in red, anterior-posterior in green, superior-inferior in blue). (F) focuses on the conversion of color and orientation. Figure modified from [25].

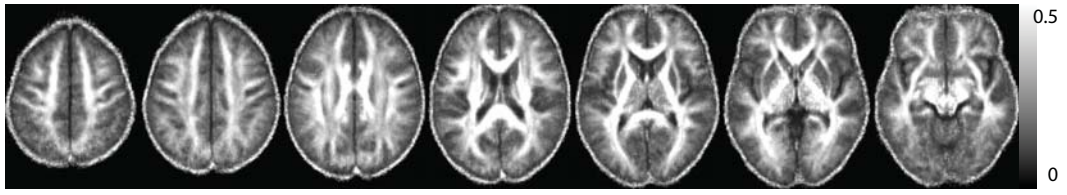


**Figure 3.5:** Data was acquired at a 3 Tesla MRI scanner. FA images of 15 healthy subjects were averaged.

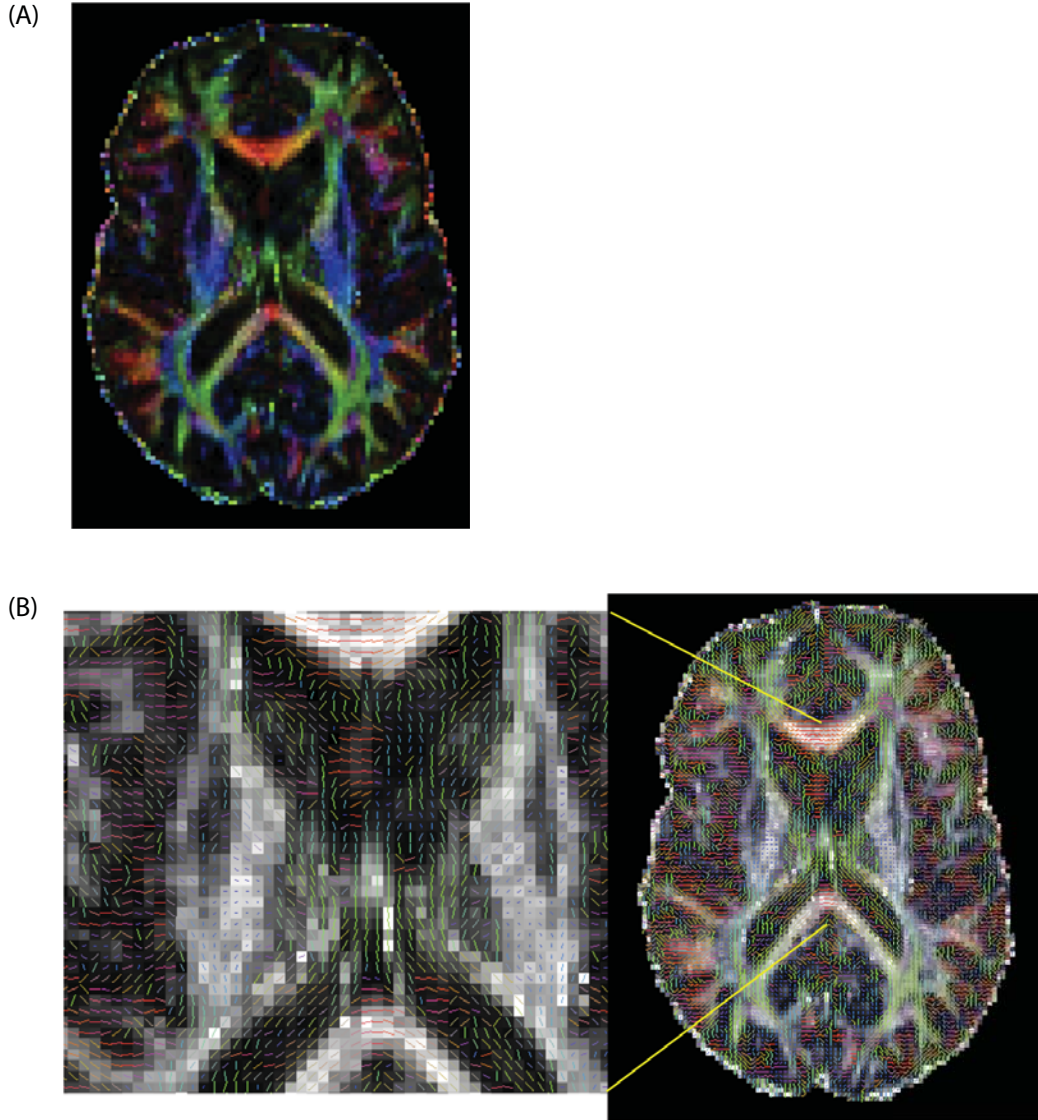


**Figure 3.6:** (A) Axial slice with color encoding (left-right in red, anterior-posterior in green, superior-inferior in blue). (B) Axial slice with color encoding (left-right in red, anterior-posterior in green, superior-inferior in blue) and additional vectors matching the main diffusion directions.

### 3.4 Fiber Tractography

Water diffusion in organized tissue such as brain white matter or muscles is anisotropic. DTI provides us with information on the grade of diffusion anisotropy and its orientation. In this section two fiber tracking approaches will be introduced: (1) "line propagation" and (2) "probabilistic" tracking.

#### 3.4.1 Line Propagation Model

Line (tract) propagation or streamlining models are deterministic and yield only one solution. For this approach three important steps are necessary [23]:

- Estimation of the local fiber orientation
- Line Propagation
- Termination criterion

The diffusion tensor or only the longest eigenvector information can be used for the estimation of the local fiber direction. The most intuitive way to reconstruct fiber tracts is to draw a straight line [24], following the longest eigenvector of the diffusion tensor of a voxel. When we reach the next voxel, the direction changes. But it is clear that this simple procedure cannot represent the real tract. The following method was introduced by Basser et. al. [4]. The fiber tract is represented by  $\mathbf{r}(s)$  which is parameterized by the arc length  $s$  of the trajectory. The equation of motion is:

$$\frac{\mathbf{r}(s)}{ds} = \mathbf{t}(s) \quad \text{with} \quad \mathbf{t}(s) \dots \text{unit tangent vector to } \mathbf{r}(s) \quad (3.26)$$

It is assumed that the normalized eigenvector  $\boldsymbol{\epsilon}_1$  of the largest eigenvalue points in the main diffusion direction which is associated with the local fiber direction (this is principally true [15,33]).

$$\mathbf{t}(s) = \boldsymbol{\epsilon}_1(\mathbf{r}(s)) \quad (3.27)$$

Combining this yields:

$$\frac{\mathbf{r}(s)}{ds} = \boldsymbol{\epsilon}_1(\mathbf{r}(s)) \quad (3.28)$$

This equation then must be solved in three dimensions, for an initial condition  $\mathbf{r}(0) = \mathbf{r}_0$ . To understand the solution process it is easiest to use Euler's method as follows. Choosing a point  $\mathbf{r}(s_1)$  we can calculate the following Taylor series:

$$\mathbf{r}(s_1) = \mathbf{r}(s_0) + \mathbf{r}'(s_0)(s_1 - s_0) + \dots \quad (3.29)$$

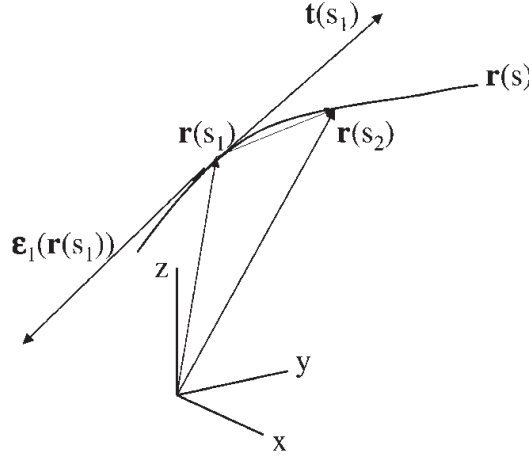


**Figure 3.8:** Calculated fiber trajectory of a 3D space curve  $\mathbf{r}(s)$  using Euler's method.  $\mathbf{r}(s_1)$  is parallel to  $\mathbf{e}_1(\mathbf{r}(s_1))$ , which belongs to the largest eigenvalue. Figure taken from [4]

We assumed that  $\mathbf{t}(s)$  is parallel to  $\mathbf{e}_1$ , therefore we can substitute the last term in equation (3.29) yielding:

$$\mathbf{r}(s_1) \sim \mathbf{r}(s_0) + \alpha \mathbf{e}_1(\mathbf{r}(s_0)) \quad (3.30)$$

$\mathbf{r}(s_1)$  can be calculated using  $\mathbf{r}(s_0)$  and  $\mathbf{e}_1(\mathbf{r}(s_0))$ . This procedure can be repeated for  $\mathbf{r}(s_1)$ ,  $\mathbf{r}(s_2)$ ,... predicting the fiber trajectory. One calculation step can be found in figure 3.8.

Euler's Method is not used in practice since it is a 1<sup>st</sup> order algorithm yielding unacceptable inaccuracies. In practice the solution can be computationally obtained e.g. using Runge-Kutta method of 2<sup>nd</sup> order or higher with adaptive step size to avoid calculation errors. The most intuitive termination call is when low anisotropy regions (such as grey matter) are reached. Typically grey matter regions have an FA value of 0.05 - 0.15 [23]. Hence a typical stop criterion is  $FA < 0.15 - 0.3$ . Another important stop criterion is the change of the angle between two voxels. It is assumed that the diffusion is Gaussian, when the angle is too large the assumption of Gaussian diffusion is no longer valid and therefore the basis of the routine tensor calculation is destroyed. Therefore it is preferable to set a threshold of curvature - by setting a maximum angle - to avoid this. With prohibiting sharp bends, propagation jumps to unrelated tracts are prevented.

To give an example of tract propagation methods, deterministic fiber tracking was applied on one healthy single subject for the whole brain (see figure 3.9) and the uncinate fasciculus (see figure 3.10) using *TrackVis*. The diffusion tensor model was estimated using the *TrackVis* toolbox *Diffusion Toolkit* (<http://trackvis.org>). For tracking an angle threshold of 30° was set. The propagation algorithm was 2<sup>nd</sup> order Runge Kutta. Data was acquired as part of an fMRI study investigating differences between social phobia patients and healthy controls.

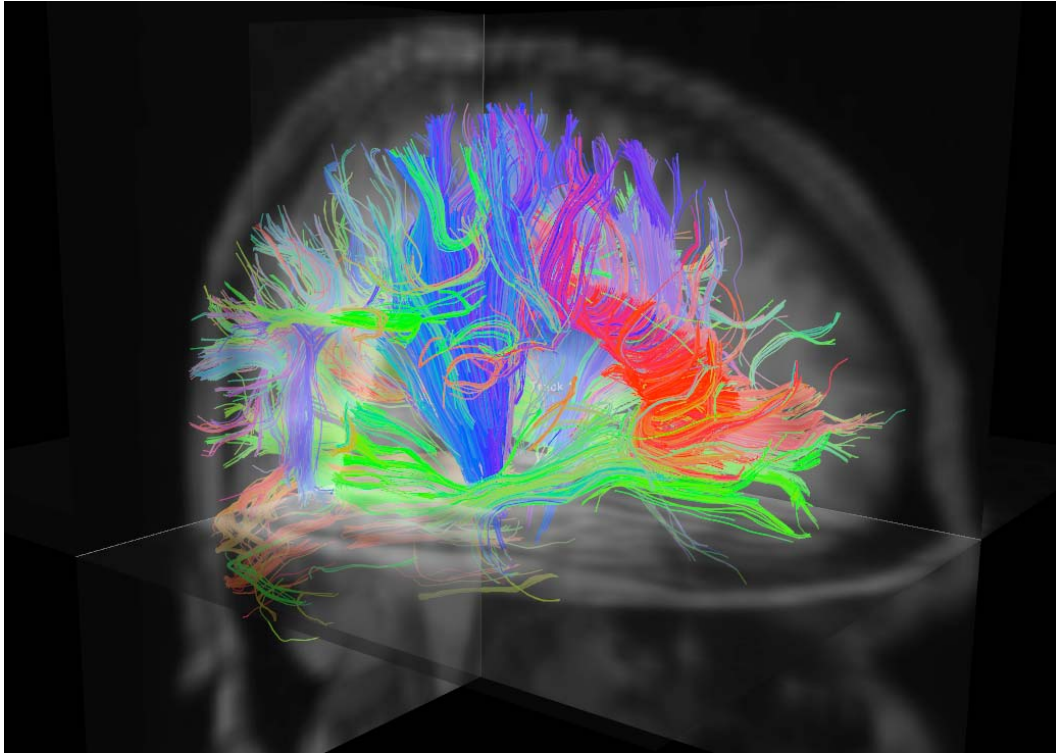


**Figure 3.9:** Deterministic fiber tracking of a healthy single subject using the software package *TrackVis*. No seed mask was used. Fiber tracking was performed for the whole brain.

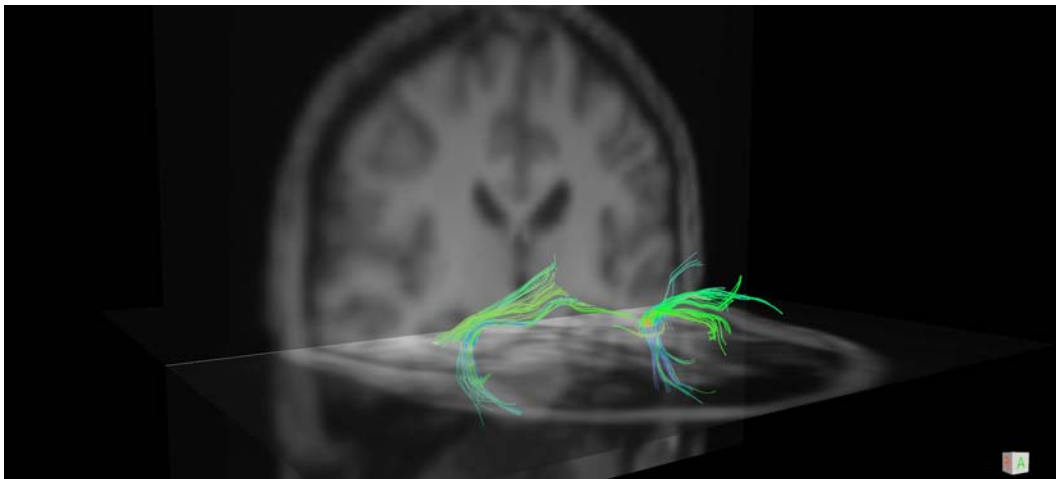


**Figure 3.10:** Deterministic fiber tractography of the UF of a healthy single subject using two seed masks bilaterally in posterior parts of the uncinate fasciculus.

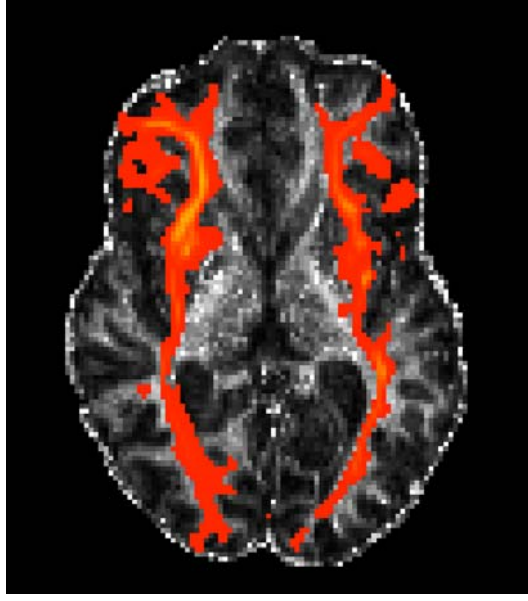


**Figure 3.11:** Probability map of a single subject. The seed masks were placed bilaterally in parts of the uncinatus fasciculus. A probability threshold of 50% was set. Yellow indicates high probability.

### 3.4.2 Probabilistic Fiber Tracking

Noise and MR artifacts but also the modeling of the diffusion signal (origin of the signal is more complex than the model) add additional uncertainty to the model parameters. In probabilistic fiber tracking these uncertainties in the parameters are represented by probability density functions (*pdfs*). The algorithm for this probabilistic framework was first presented by Behrens et. al. in 2003 [7]. With this framework local density functions are estimated. For this estimation different diffusion models can be assumed. Two simple diffusion models are for instance: (1) diffusion tensor model and (2) partial volume model. The former was already introduced in section 3.2. The partial volume model assumes that the diffusion is dominant along a single direction; in all other directions the diffusion is isotropic. We are looking for the set of parameters  $\omega$ , which fit the data best. To calculate the local *pdf* Bayes notation is used ( $Y$ ...data, and  $M$ ...model):

$$\mathcal{P}(\omega | Y, M) = \frac{\mathcal{P}(Y | \omega, M)\mathcal{P}(\omega | M)}{\mathcal{P}(Y | M)} \quad (3.31)$$

The calculation of the *pdf* is seldom straightforward. Therefore we have to re-write equation (3.31):

$$\mathcal{P}(Y, M) = \int_{\Omega} \mathcal{P}(Y | \omega, M)\mathcal{P}(\omega | M)d\omega \quad (3.32)$$

which is often not analytically solvable. Practical ways to solve these integrals are Markov Chain Monte Carlo (MCMC) algorithms.

Using the local parameters, the global connectivity can be estimated. To understand transition from local to global connectivity estimation it is easiest to assume no uncertainty in the parameters

we just estimated for the local *pdf*. Assuming no uncertainty and diffusion only in one direction, the global connectivity can only have two values

$$\mathcal{P}(\exists A \rightarrow B \mid Y) = \begin{cases} 1, & \exists \text{ connecting path} \\ 0, & \text{otherwise} \end{cases} \quad (3.33)$$

were  $\mathcal{P}(\exists A \rightarrow B)$  is the probability for a connection between two points A and B. To calculate this probability we follow the local fiber direction starting from A until a stop criterion is met. If B is met during the calculation, a connection exists. This simple procedure recalls the algorithm of the line propagation model (see section 3.4.1). This model, however, is not taking account of uncertainty. Hence  $\mathcal{P}(\exists A \rightarrow B \mid Y)$  needs to consider all possible fiber orientations. Assuming all possible directions  $(\theta, \phi)_{x_i}$  equation (3.33) becomes using data Y

$$\mathcal{P}(\exists A \rightarrow B \mid Y) = \int_0^{2\pi} \int_0^\pi \cdots \int_0^{2\pi} \int_0^\pi \mathcal{P}(\exists A \rightarrow B \mid (\theta, \phi)_{x_i}) \mathcal{P}((\theta, \phi)_{x_1} \mid Y) \dots \mathcal{P}((\theta, \phi)_{x_n} \mid Y) d\theta_{x_1} d\phi_{x_1} \dots d\theta_{x_n} d\phi_{x_n} \quad (3.34)$$

with  $n$  being the number of all possible directions and  $\mathcal{P}((\theta, \phi)_{x_i} \mid Y)$  the local *pdf* in the position  $i$ . In the case of only one direction,  $\mathcal{P}((\theta, \phi)_{x_i} \mid Y)$  are delta functions and equation (3.34) reduces to the maximum likelihood solution (streamlining) seen in equation (3.33). When the local fiber direction however is uncertain the connectivity pattern will spread from A. We see that the main difference between tract propagation and probabilistic tracking is that uncertainty is allowed. The results of the probabilistic algorithm consider all possible fiber directions of all voxels.

Since the local fiber direction is calculated with a MCMC algorithm equation (3.34) is not analytically solvable. One approach to calculate the global connectivity pattern is to build a *spatial pdf* of  $\mathcal{P}(\exists A \rightarrow B \mid Y)$ . To do so we start with a so-called probabilistic streamline  $\mathbf{z}$  at A, select a direction  $(\theta, \phi)$  from  $\mathcal{P}((\theta, \phi) \mid Y)$  and move a distance  $s$  along  $(\theta, \phi)$ , afterwards we continue this procedure from the new position. This is repeated until one stopping criterion is met (stopping criteria can be found in section 3.4.1). This streamline is calculated several times. Counting all fibers passing through a voxel B and dividing it by the total number of probabilistic streamlines yields a discrete distribution. This discrete distribution is a "connectivity distribution" giving a probability distribution of a pathway using dominant fiber directions for its calculation [7].

The above explained sampling technique depends on continuous samples. This is not possible for MR acquisition therefore interpolation is needed. Standard interpolation such as sinc or trilinear interpolation would be possible but not feasible since the computational time would be too costly. An alternative is to take the diffusion direction of random nearby voxel since the fiber direction does not change very much in the center of the main fiber tracts. This saves computational time and yields comparable results. In figure 3.11 an example of the above explained algorithm can be



found. This algorithm is included in the software package FSL (<http://www.fmrib.ox.ac.uk/fsl/>, Oxford University, UK).

### 3.4.3 Pitfalls and Limitations of Fiber Tractography

Performing fiber tractography we must be aware of limitations and pitfalls.

- Noise

In every MR image the accuracy of the data is limited by noise. In case of fiber tracking this could yield deviations from the real fiber direction.

- Partial volume effect

If we have a voxel between two unrelated fibers the algorithm is not necessarily able to consider both fibers as independent, but rather averages both fibers yielding a wrong angle.

- Branching

Axons often have branches. If axons exit or merge from certain bundles this might not be adequately reflected in DTI derived tracts.

- Crossing fibers

Fiber tracking algorithms that use the diffusion tensor model are not able to differentiate between "crossing" and "kissing" fibers, therefore the algorithm stops or follows a random direction yielding false negatives or false positives, respectively.

- Disk-shape diffusion ellipsoid

In areas where the diffusion anisotropy is disk-shaped the longest axis of the diffusion ellipsoid is random. If the propagation is not terminated in such voxels, large errors are resulting.

## References

Additional literatures that have been used in this section are:

- S Mori. 2007. *Introduction to Diffusion Tensor Imaging*. Elsevier Science.
- F Schmitt, M K Stehling, R Turner. 1998. *Echo-Planar Imaging: Theory, Technique and Application*. Springer.



## Chapter 4

# Data Preprocessing in DTI

In the following a typical and often used preprocessing pipeline for DTI data will be presented. Further, two additional normalization approaches will be introduced: (1) DARTEL and (2) TBSS. The idea behind DARTEL is to register images using a "flow field". Forward and backward deformations for normalization are calculated using this flow field. TBSS is a nonlinear registration method, which aims to improve registration of images via calculation of a "mean FA skeleton" which is then used for further analysis.

### 4.1 Standard Preprocessing

#### Eddy Current Correction

Applying different gradient directions we encounter image distortion in diffusion-weighted images. These distortions (stretching and shearing of data) originate from induced eddy currents in the gradient coils and are dependent on the gradient direction. The software package FSL includes an eddy current correction tool to compensate these distortions, by registering the stretched diffusion-weighted images to the  $b_0$  volume.

#### Fit of the Diffusion Tensor Model

The diffusion tensor is estimated for every voxel. In this step the mean diffusivity, eigenvectors, eigenvalues and FA are calculated for every voxel (see chapter 3). The fit of this model can be performed e.g. with the software package FSL (Centre of functional MRI of the Brain, University of Oxford, United Kingdom).

## Co-Registration

Co-registrations makes use of 6 parameters, 3 for translation (x-, y- and z-direction) and 3 for rotation (angles  $\alpha$ ,  $\beta$  and  $\gamma$ ) to rotate and translate the  $T_1$  image to match the  $b_0$ -volume of the diffusion data (volume acquired without diffusion gradient). The  $T_1$  image is then normalized yielding transformation matrices.

## Segmentation - Normalization

Diffusion data needs to be normalized to a common anatomical space to enable a comparison across groups. One common space is the so-called MNI space (Montreal Neurological Institute space). This space is defined by the average image of 152 subjects. Another option is the Talairach space [38]. The classical normalization approach for EPI data is to use an EPI template (e.g. standard EPI template from SPM8). The measured data is then registered to this template.

In general, spatial normalization is achieved by minimizing the sum of squared difference between a linear combination of one or more templates and the images that need to be normalized. To do, so the first step is to match the position and size of the template by using an affine registration [11]. An affine registration has 12 degrees of freedom: 3 translations, 3 rotations, 3 zooms and 3 shears. The affine transformation aims to minimize the mean squared difference between source and target image by using these 12 parameters. In the next step a global non-linear warping is applied to match the over-all shape of the brain. This deformation is calculated using linear combinations of smooth basis images (lowest frequencies basis function of discrete cosine transform, see figure 4.1).

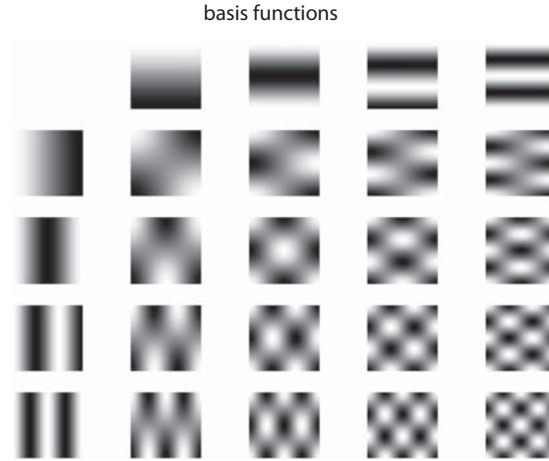


**Figure 4.1:** (A) Basis functions with lowest frequencies of a 2 dimensional discrete cosine transform. Deformation fields are linear combinations of these smooth functions. Light areas indicate a shift left/up and dark areas a shift right/down. Image retrieved from [11].

Another approach for normalization is matching a tissue class with the normalized tissue class template. Therefore segmentation is necessary. To classify different tissues in the human brain a modified Gaussian mixture model is used [2]. To apply this model we assume that every voxel of the brain belongs to a distinct tissue type (cluster) and that every cluster follows a Gaussian distribution (see figure 4.2). Using the intensity information of the histogram of an anatomical image results into some misclassifications, e.g. grey matter is similar to the scalp (see figure 4.2) and therefore, additional prior information is used. Prior probability maps contain the information for each tissue class and are generated using a large number of subjects.

The probability for every voxel to belong to a certain tissue class is calculated combining prior information (probability derived from tissue classification templates) and the likelihood of the voxel to belong to that class (from initial segmentation) using Bayesian rule. In statistics, Bayesian rules relate conditional probabilities. Given the prior probability  $P(A)$  of an event A and the prior probability  $P(B)$  of an event B the posterior probability for both events A and B is [21]

$$P(A | B) = \frac{P(B | A) \cdot P(A)}{P(B)} \quad (4.1)$$

with  $P(B | A)$  being the probability for the event B upon condition that A occurred. Thus combining prior templates with posterior probability maps we can improve the segmentation (see figure 4.3).

Segmentation can be performed using SPM's *Segment* or *New Segment* routine. *New Segment* is an extension of *Segment*. Both use principally the same algorithm, slight differences are in the details of the mixing proportions, the registration model and an extended set of probability maps [1]. A comparison of both routines for one healthy single subject can be found in figure 4.4 for grey matter and in figure 4.5 for white matter.

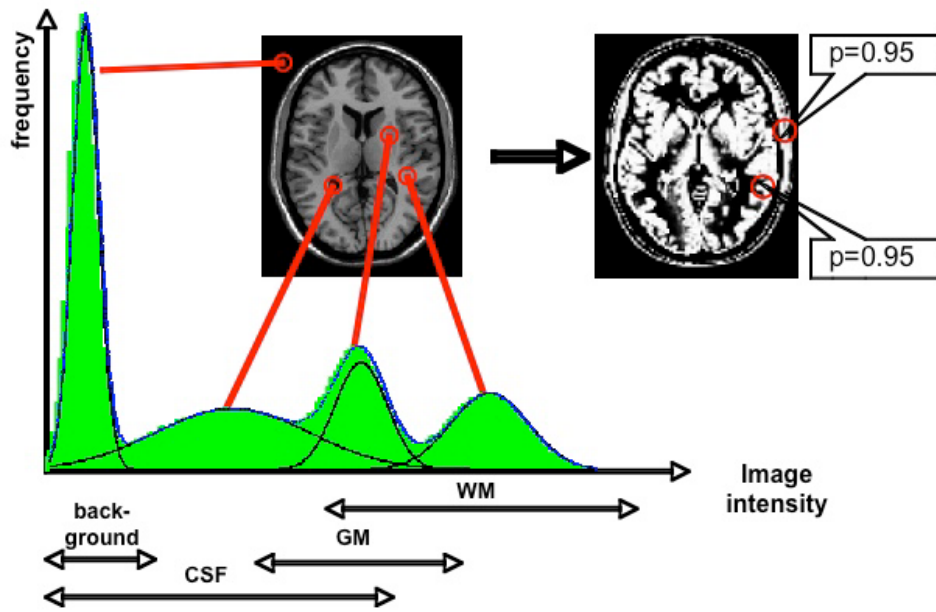


**Figure 4.2:** Histogram. Differentiation of different distributions yields tissue classed and background (left image). Using no prior information the initial segmentation results into some misclassification. In the right image segmented grey matter is shown (right image). Since the scalp intensity is similar to grey matter intensity, also the scalp is shown. Image retrieved from [27].

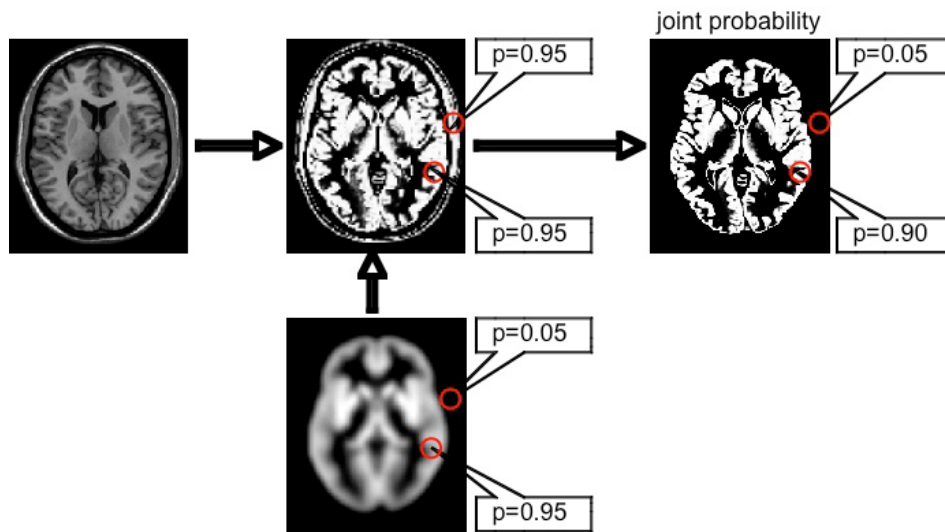


**Figure 4.3:** Using Bayesian rules initial segmented images are combined with prior probability maps improving the assignment to a certain tissue class. The red circles indicate the probability of this voxel to belong to grey matter. In the initial segmentation (upper middle image) contains the scalp (probability of 95 %). The bottom image shows the prior probability map not containing the scalp. Combining both images a joint probability map is calculated improving segmentation of the original image. Image retrieved from [27].

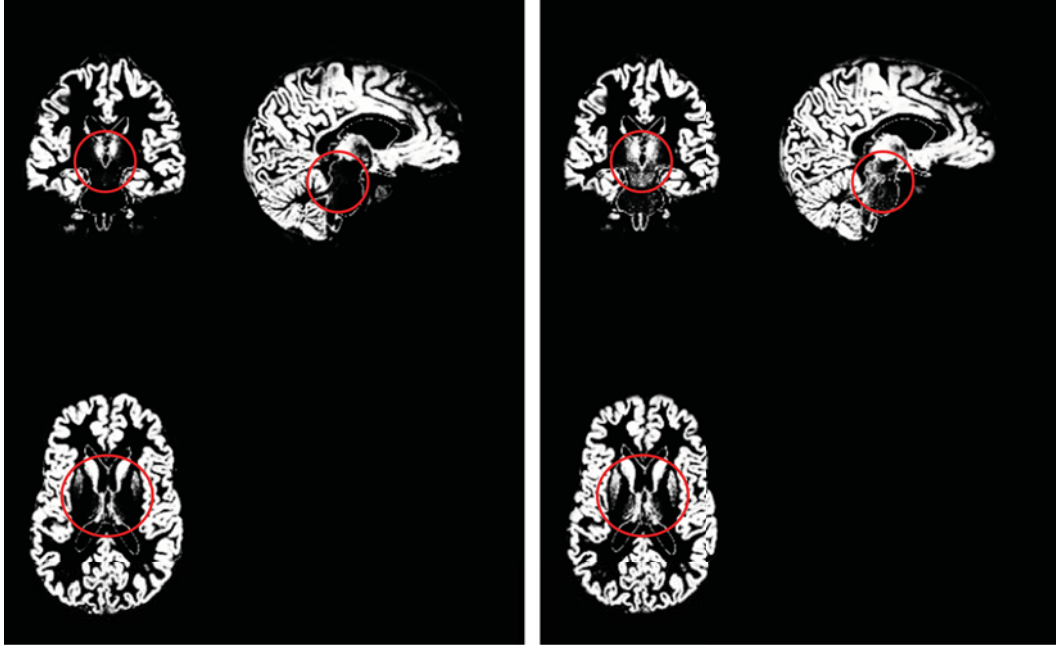


**Figure 4.4:** Segmented grey matter of healthy single subject in native space. Left image processed with *New Segment*, right image with *Segment*. Differences are indicated with a red circle.

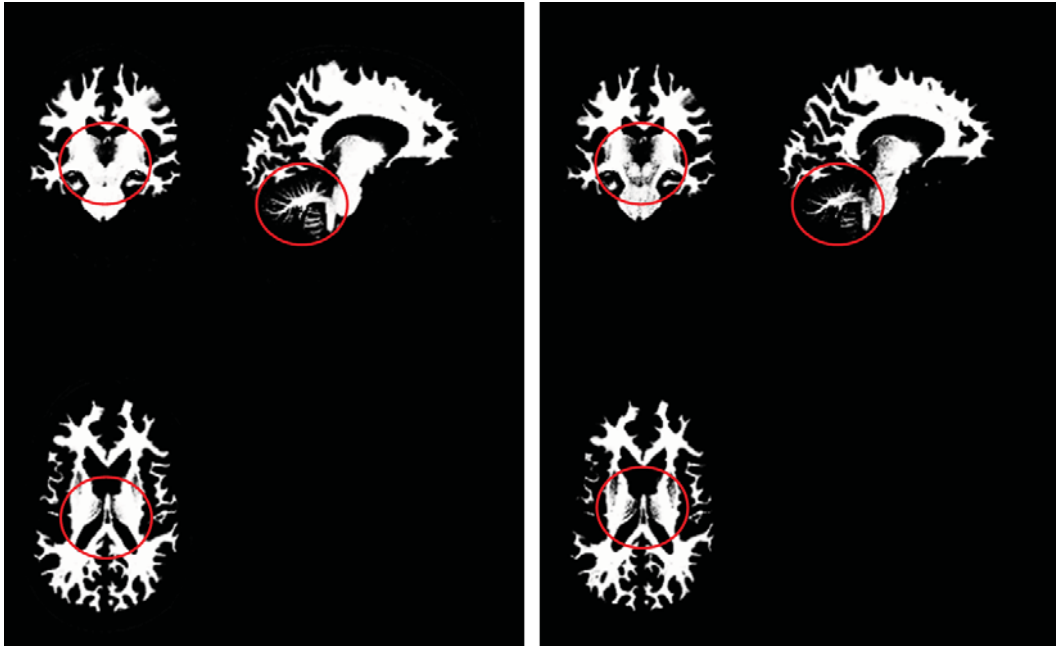


**Figure 4.5:** Segmented white matter of healthy single subject in native space. Left image processed with *New Segment*, right image with *Segment*. Differences are indicated with a red circle.

## Spatial Smoothing

In general, a Gaussian kernel is used for smoothing. The full width half maximum (FWHM) is dependent on the voxel size and on the structures of the tissue which will be analyzed (typically between 2 mm and 9 mm). It improves the signal to noise ratio but also decreased spatial resolution. Smoothing is especially important for group analysis, as it improves inter-subject registration. Figure 4.6 shows the smoothing of an axial slice for one data set.

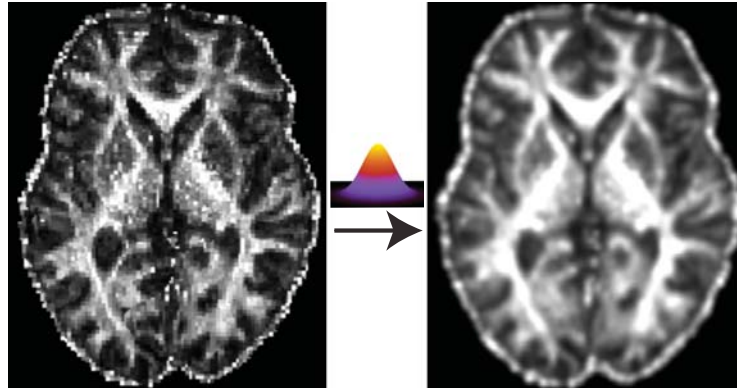


**Figure 4.6:** Smoothing of one data set with an isotropic Gaussian kernel of 3 mm.

## 4.2 DARTEL - A fast diffeomorphic image registration algorithm

Co-registration and normalization "stretches", "squeezes" and "rotates" images to approximately match the structure of a reference image. But we neither have an absolute measure of alignment quality nor if certain tracts of several subjects really contain the same white matter tract.

One way to improve the alignment of MR images was developed and implemented by John Ashburner in the toolbox "DARTEL" in SPM. DARTEL is an abbreviation of Diffeomorphic Anatomical Registration using Exponentiated Lie algebra. As its name implies, DARTEL is an algorithm for diffeomorphic image registration [3]. The motivation behind this algorithm is a better inter-subject alignment, which should yield enhanced fMRI analyses, computational anatomy (volumes and parameterization of brain shapes) and tissue segmentation. Diffeomorphism is a concept of mathematics. The definition of diffeomorphism is [46]:

- $\Omega$  is a continuous bijection  $\phi : \Omega \rightarrow \Omega$  so that the inverse  $\phi^{-1}$  is continuous.
- A diffeomorphism of  $\Omega$  is, if  $\phi : \Omega \rightarrow \Omega$  is continuously differentiable so that  $\phi^{-1}$  is continuously differentiable.



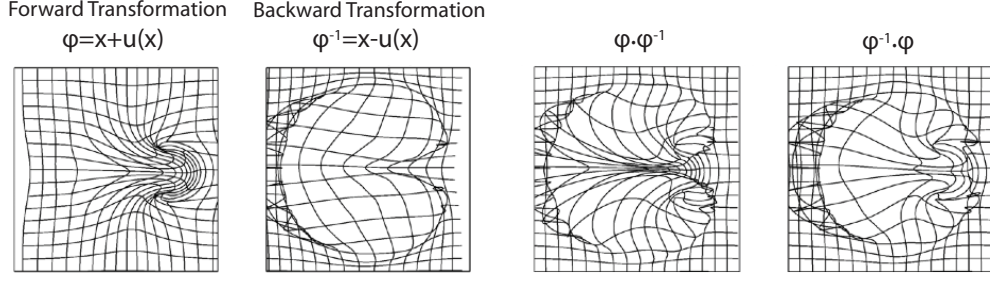


**Figure 4.7:** Non-diffeomorphic transformations.  $\phi \times \phi^{-1}$  is unequal  $\phi^{-1} \times \phi$ . Figure modified from [3]

For MRI analysis this means the following: Having a diffeomorphism applying the forward and inverse transformation on an image should yield the same image. Hence a composition of forward and inverse transformation should yield an identity transform- when we have a perfect diffeomorphism. In figure 4.9 you can see the results of a diffeomorphic composition of forward and inverse transformation and vice versa. In figure 4.7 a non-diffeomorphic composition of forward and inverse transformation and vice versa can be found yielding different results. In other words when we use registration routines the topology of the human brain is conserved. Many registration routines are done by adding a displacement field  $u$  (so-called small deformation model):

$$\Phi(x) = x + u(x) \quad (4.2)$$

The inverse can be calculated by subtracting the displacement field. This leads to the problem that the topology might not be conserved as can be seen in figure 4.7. The huge advantage of DARTEL is that it does not use such a small-deformation model.

Using DARTEL as in [3] a flow field is introduced.

$$\frac{d\Phi}{dt} = \mathbf{u}(\Phi^{(T)}) \quad (4.3)$$

Using Euler integration and starting with an identity ( $\Phi^{(0)} = Identity$ ,  $\Phi^{(1)} = \int_{t=0}^1 \mathbf{u}(\Phi(t))dt, \dots$ ) we can compute several time steps. The inverse is calculated by backward integration. The Euler integration can be performed as follows

$$\Phi^{(t+h)} = (x + h\mathbf{u}) \cdot \Phi(t) \quad (4.4)$$

with  $h$  being the step size. An example of 8 time steps would be [3]

$$\begin{aligned} \Phi^{(1/8)} &= x + \mathbf{u}/8 \\ \Phi^{(2/8)} &= \Phi^{(1/8)} \cdot \Phi^{(1/8)} \\ \Phi^{(3/8)} &= \Phi^{(1/8)} \cdot \Phi^{(2/8)} \\ &\vdots \\ \Phi^{(8/8)} &= \Phi^{(1/8)} \cdot \Phi^{(7/8)} \end{aligned} \quad (4.5)$$

Another approach is [3]

$$\begin{aligned}
\Phi^{(1/8)} &= \mathbf{x} + \mathbf{u}/8 \\
\Phi^{(1/4)} &= \Phi^{(1/8)} \cdot \Phi^{(1/8)} \\
\Phi^{(1/2)} &= \Phi^{(1/4)} \cdot \Phi^{(1/4)} \\
\Phi^{(1)} &= \Phi^{(1/2)} \cdot \Phi^{(1/2)}
\end{aligned} \tag{4.6}$$

De facto more than 8 time steps are needed to calculate accurate solutions. The flow field  $\mathbf{u}$  can be regarded as a member of the Lie algebra.  $\mathbf{u}$  is exponentiated yielding a deformation, which itself is a member of a Lie group. Lie algebra was first introduced by Hermann Weyl and is named after Sophus Lie. Lie algebra is a vector space  $\mathcal{L}$  of linear transformations over a field  $\mathcal{F}$ . A Lie algebra satisfies the following criteria [16]:

- For every pair  $(x, y)$  in  $\mathcal{L}$  the following bilinearity conditions must be satisfied:  
 $(x_1 + x_2)y = x_1y + x_2y$ ,  $x(y_1 + y_2) = xy_1 + xy_2$  and  $\alpha(xy) = (\alpha x)y = x(\alpha y)$
- $[x, x] = 0$  must be fulfilled for all  $x$  in  $\mathcal{L}$
- Jacobi identity:  $[x, [y, z]] + [y, [z, x]] + [z, [x, y]] = 0$

A simple example of a Lie group would be the rotation group of a sphere. All points at the surface can be determined by a certain angle  $\phi$  and  $\theta$ . Through infinitesimal rotations all elements can be reached continuously. Considering the DARTEL algorithm this allows that forward transformation and backward transformation can be calculated from the same flow field  $\mathbf{u}$ , since all elements of the Lie group - in this case the spatial deformations - can be obtained continuously. This also ensures diffeomorphic transformations, since forward and backward transformation can be obtained continuously in both directions. The spatial backward transformation is calculated via backward integration as follows

$$\begin{aligned}
\Phi^{(-1/8)} &= \mathbf{x} - \mathbf{u}/8 \\
\Phi^{(-1/4)} &= \Phi^{(-1/8)} \cdot \Phi^{(-1/8)} \\
\Phi^{(-1/2)} &= \Phi^{(-1/4)} \cdot \Phi^{(-1/4)} \\
\Phi^{(-1)} &= \Phi^{(-1/2)} \cdot \Phi^{(-1/2)}
\end{aligned} \tag{4.7}$$

These integration steps for forward and backward integration can be seen in figure 4.8.

When we now take these two transformations and make a composition of both we get in the best case an identity transform (see figure 4.9). Now we can calculate the derivatives (Jacobian Matrices) of the deformations:

$$J_{\Phi(x)} = (\nabla \Phi^T) = \begin{pmatrix} \frac{\partial \phi_1(x)}{\partial x_1} & \frac{\partial \phi_1(x)}{\partial x_2} & \frac{\partial \phi_1(x)}{\partial x_3} \\ \frac{\partial \phi_2(x)}{\partial x_1} & \frac{\partial \phi_2(x)}{\partial x_2} & \frac{\partial \phi_2(x)}{\partial x_3} \\ \frac{\partial \phi_3(x)}{\partial x_1} & \frac{\partial \phi_3(x)}{\partial x_2} & \frac{\partial \phi_3(x)}{\partial x_3} \end{pmatrix} \tag{4.8}$$

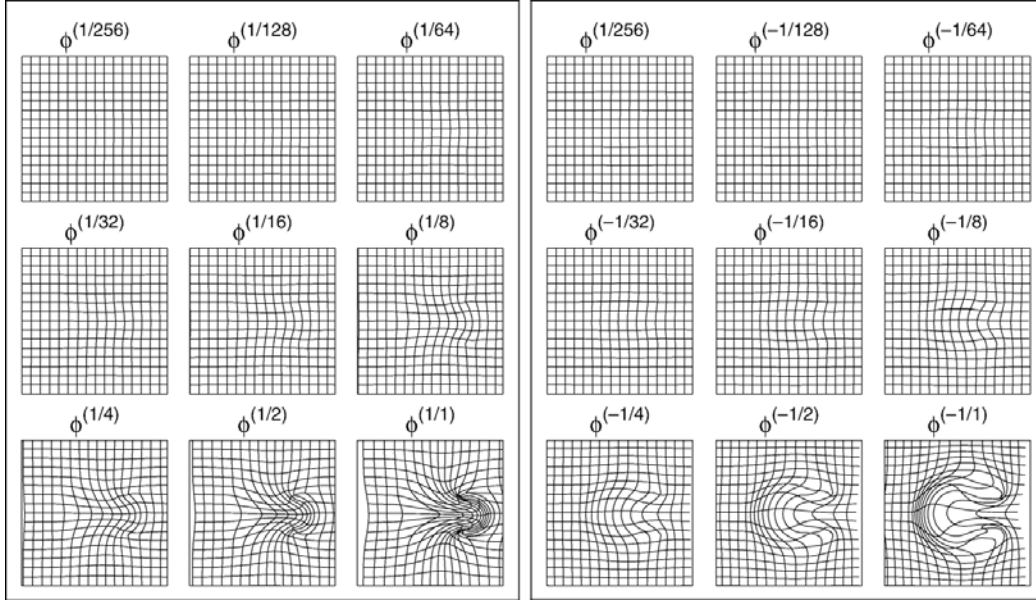


**Figure 4.8:** Computing of the deformation (left) and the inverse deformation (right). Figure taken from [3].

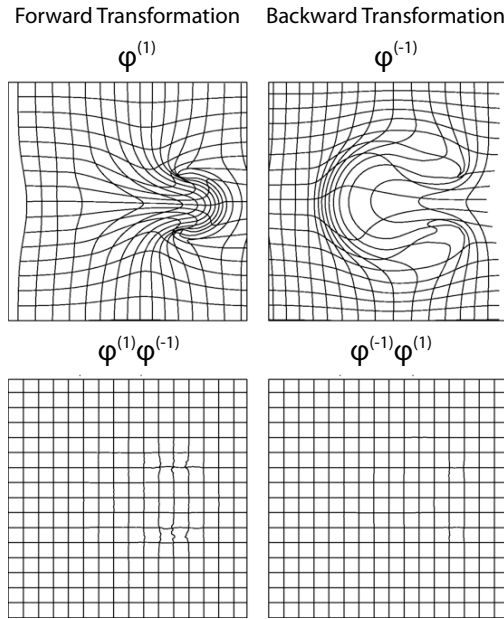


**Figure 4.9:** Composition of forward and inverse transformation yielding a nearly perfect identity transform. Figure taken from [3].

these matrices contain the information of local stretching, shearing and rotating of the deformation field. The model now contains parameters that describe the image deformation. The aim of the algorithm now is to find the "best" set of parameters.

## DARTEL Normalization Example

For normalization with DARTEL the following steps are necessary:

- DARTEL Preprocessing: Segmentation of  $T_1$  images using *New Segment* as implemented in the SPM8. In this step grey matter and white matter are segmented in native space and are subsequently prepared for the following DARTEL algorithm, yielding normalized segmentations. CSF is only segmented in native space. The segmentation of CSF is not necessary, but it has been shown that including it in the calculation improves the segmentation [1]. Normalized grey and white matter images can be seen in figure 4.10.

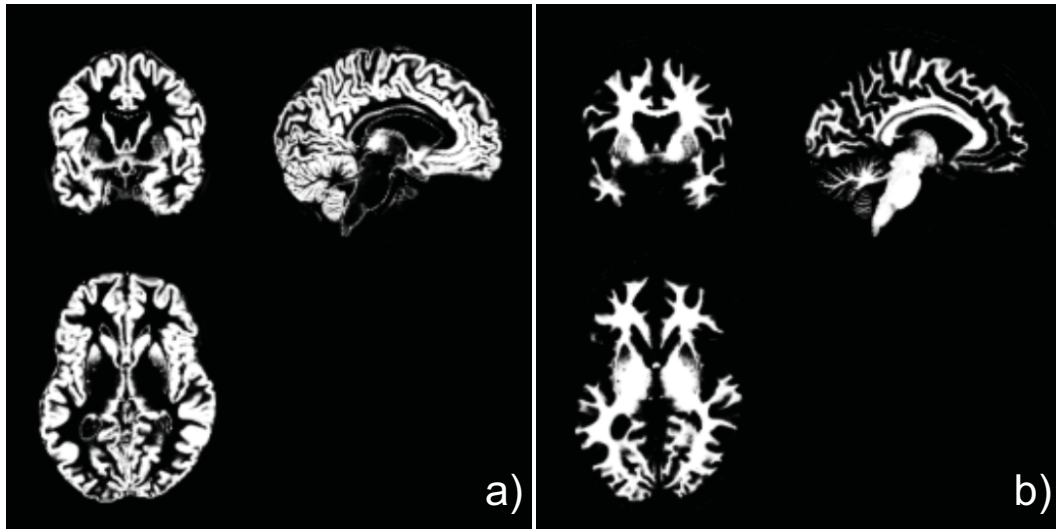


**Figure 4.10:** Segmentation results of a healthy single subject in normalized space (MNI). a) Grey Matter and b) White Matter.

- A DARTEL template is created by using the previously normalized grey and white matter images. With this DARTEL white and grey matter templates are calculated and deformation (or flow field) fields are estimated. The DARTEL template can be found in figure 4.11. The deformation field for grey matter for one healthy subject can be found in figure 4.12. This deformation field contains the information for spatial transformation. Light areas in the deformation field indicate a shift to the left, dark areas to the right.

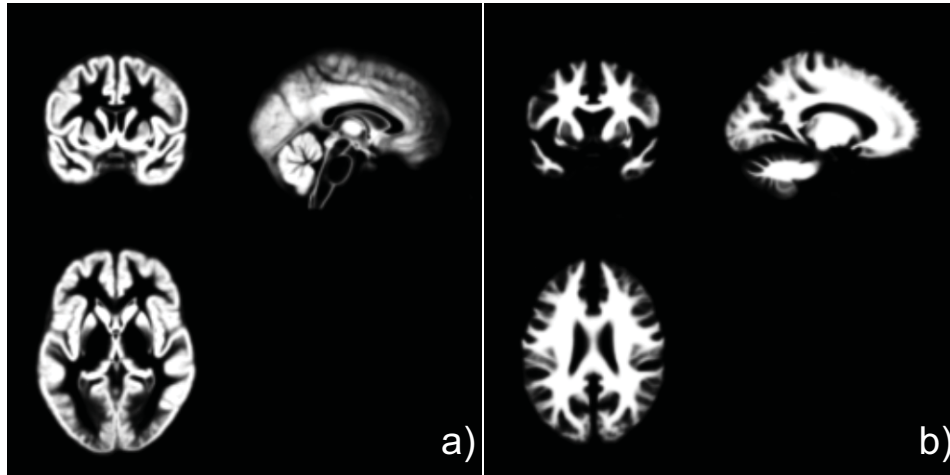


**Figure 4.11:** a) DARTEL grey matter template b) DARTEL white matter template. Both templates are not in MNI space.

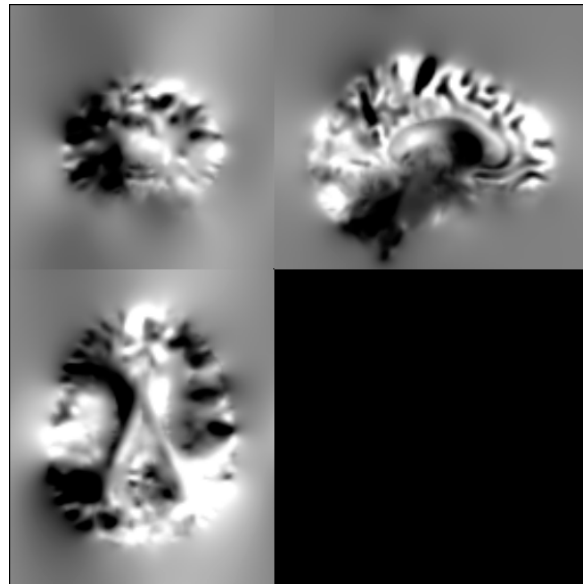


**Figure 4.12:** Grey matter flow field of a healthy single subject calculated using DARTEL.

- The DARTEL template along with the flow field are used for normalization. The template itself is not normalized. In this step the DARTEL template is normalized to MNI space using an affine registration. The flow field along with the parameters of the affine registration are then used for normalization of the original data.

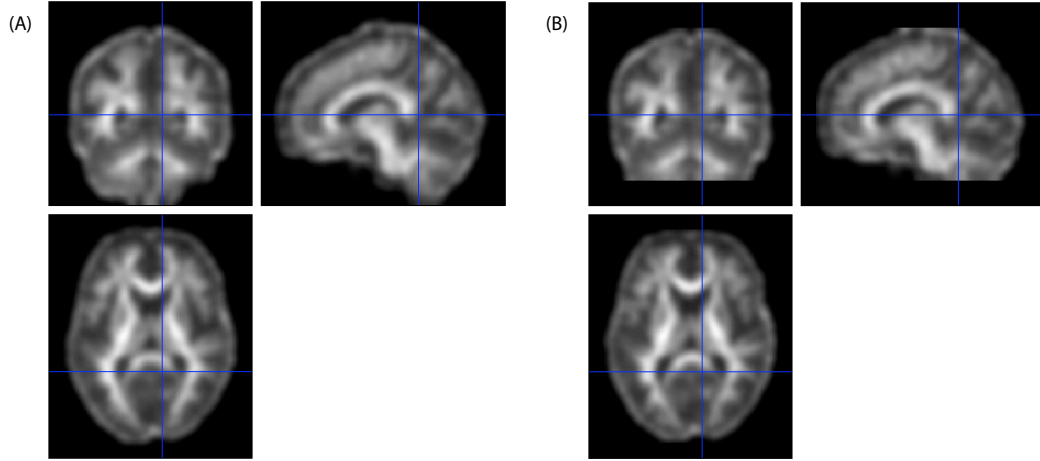


**Figure 4.13:** (A) Normalized FA image of a healthy single subject using DARTEL. (B) Normalized FA image using standard pipeline including co-registration, segmentation and normalization

We can now compare the results of the DARTEL algorithm with the results of the standard preprocessing pipeline. The registration of the brain shape for both normalization routines are comparable (see figure 4.13). However, the DARTEL algorithm reslices the original data to match the template and reduces the spatial resolution in this step. This is not the case for the standard normalization routine, there the original data is also resliced, but the spatial resolution is not reduced.

### 4.3 Tract Based Spatial Statistics - TBSS

Another normalization approach is tract-based spatial statistics (TBSS). Commonly used normalization routines for FA images apply the following preprocessing pipeline:

- aligning volumes with b-value of 0 ( $b_0$  volumes), e.g. data without diffusion weighting, along with the FA images with the anatomical images (for example with SPM8 using the function *coregister(estimate)*)
- Segmentation and Normalization of the  $T_1$  images yielding transformation matrixes
- Applying these transformation matrices to the FA images
- Further smoothing of the FA images

This preprocessing now raises some questions. How good is the alignment of the FA images with the anatomical images. Do the same white matter voxel of different subjects represent the same fiber tract and are therefore comparable voxel-wise? Another question refers to the smoothing. Commonly used smoothing routines use a Gauss kernel with FWHM from 2 mm to 9 mm. This questions was investigated by Jones and colleagues [18], who analyzed schizophrenia data using different smoothing kernels (FWHM from 0 mm to 16 mm). The results were depending on FWHM, hence the choice of the FWHM changes the resulting effects. This short introduction on some problems that come along with the preprocessing pipeline above should make it clear why many researches are trying to improve the normalization pipeline for FA data. Smith and colleagues [34] proposed and implemented TBSS in the software package FSL. The intention of TBSS is to improve the alignment of all subjects by projection of FA to a mean FA skeleton that represents the main fiber tracts in white matter. Further it does not use smoothing.

According to [34] TBSS includes:

- Alignment: All subjects should be aligned to each other. For this all subject images are searched for the most common subject in the group, defined by the minimal displacement that is needed to align all subjects to the most common subject. When the most common subject is identified, all other subjects get aligned to it. At this point the alignment does not need to be perfect.
- Mean image: The next step is to create the mean image of all aligned subjects.
- FA skeleton: The mean image is then "thinned". For the thinning the first derivative of the FA image is calculated. Considering voxel close to the tract center, FA will be higher in one direction, this direction points to the tract center. Looking at the first derivative this means that we are searching for the centre-of-gravity. This local centre-of-gravity represents the tract centre. This gravity centre is calculated over the whole brain examining a  $3 \times 3 \times 3$  voxel neighborhood.

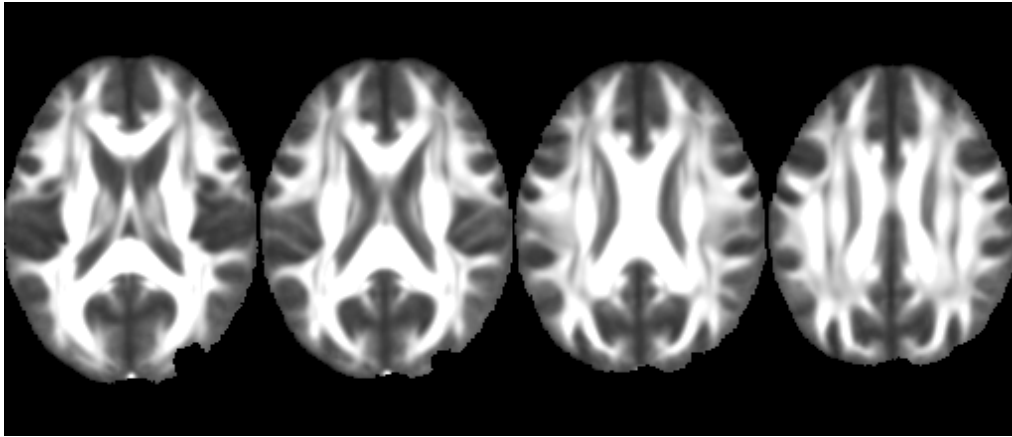


**Figure 4.14:** Calculated mean FA image resulting from 30 data sets. Image was calculated in FSL.

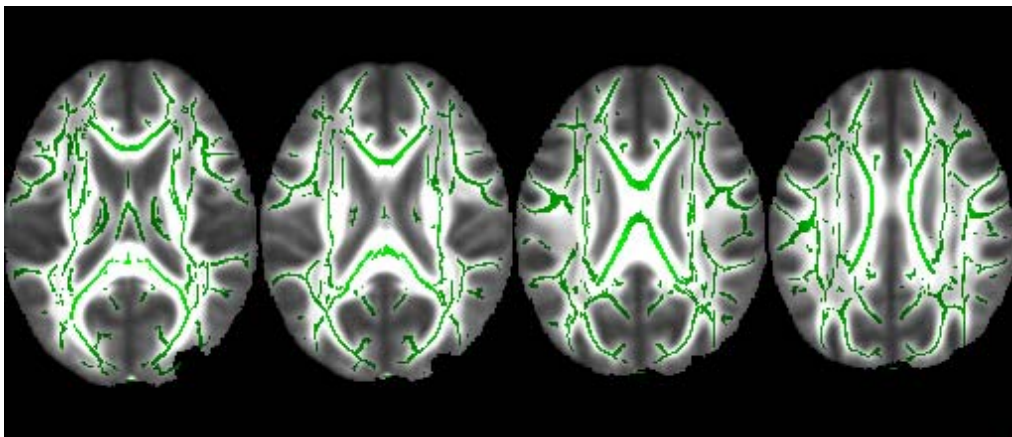


**Figure 4.15:** FA skeleton after "thinning" of the mean FA image.

- **Projection:** The algorithm now needs to "project" the FA values of the aligned subject images onto the created skeleton. The intention behind this step is to take account of possible misalignments. The single subject is examined perpendicular to the tract direction searching for the voxel that is maximal, which is then assigned to the FA skeleton. In this step projection maps are calculated.
- **Statistical Analysis:** Group analysis of the projected data using FSL.

All steps were performed on 30 data sets. For the FA skeleton a minimum FA threshold of 0.2 was set. Mean FA image can be seen in figure 4.14. Figure 4.15 shows the resulting FA skeleton.



## Chapter 5

# Application of Diffusion Tensor Imaging

In this master thesis, MRI and image processing are used to examine white matter differences between social anxiety disorder (SAD) patients and healthy controls (HC). White matter (WM) is one component of the central nervous system mostly containing myelinated axons. In WM fiber tracts connect grey matter regions, similar to a network system that connects several processor units.

Functional magnetic resonance imaging (fMRI) studies have revealed that SAD patients show higher activation in frontal regions and amygdala when presented to emotional faces [8, 9, 28, 36, 37, 45]. This led to the hypothesis that the reason for this may lie in white matter alterations. Diffusion tensor imaging (DTI), a recently developed MRI technique, allows to examine anatomical structure and connectivity by measuring water diffusion (see chapter 3). Therefore recent studies approach the topic additionally using DTI, confirming white matter alterations, especially in the uncinate fasciculus (UF) connecting amygdalae and orbitofrontal cortex [5, 29].

Aiming to quantify white matter alterations in the UF confirming recent findings, DTI and probabilistic fiber was used to examine 30 subjects (15 healthy controls, 15 SAD patients). FA was calculated to study white matter regions connecting amygdalae and frontal regions, especially the orbitofrontal cortex. Further probabilistic fiber tracking was performed to calculate a study specific mask of the UF. The results of this application have been published and presented at the following conferences:

- J Tröstl, R Sladky, A Hummer, C Kraus, E Moser, S Kasper, R Lanzenberger, C Windischberger. 2011. Reduced Connectivity in the Uncinate Fiber Tract Between the Frontal Cortex and Limbic Subcortical Areas in Social Phobia. European Congress of Psychiatry 2011. Poster and Talk

- J Tröstl, R Sladky, A Hummer, C Kraus, E Moser, S Kasper, R Lanzenberger, C Windischberger. White Matter Alterations in Social Anxiety Disorder: a DTI study. Human Brain Mapping Conference 2011. Poster.
- J Tröstl, R Sladky, A Hummer, C Kraus, E Moser, S Kasper, R Lanzenberger, C Windischberger. Veränderungen im Fasciculus Uncinatus in Sozialphobie - eine DTI Studie. 3. Ländertagung medizinische Physik. Talk.
- J Tröstl, R Sladky, A Hummer, C Kraus, E Moser, S Kasper, R Lanzenberger, C Windischberger. DTI of white matter alterations in the uncinate fasciculus of social phobia patients. European Society for Magnetic Resonance in Medicine and Biology Meeting 2011. Talk.

## 5.1 Social Anxiety Disorder

Social phobia, also known as social anxiety disorder (SAD), is one of the most common anxiety disorders. SAD is characterized by an intense and irrational fear of being scrutinized by others. According to DSM-IV, this fear originates from the apprehension of saying or doing something that will embarrass or humiliate them. Therefore individuals with SAD try to avoid social situations whenever possible or if unavoidable, they experience intense distress during such situations. When interacting with others they appear very shy, silent and reserved [35].

Functional MRI studies have demonstrated that SAD patients show higher activation in the amygdala compared to healthy controls when presented with emotional faces [8, 9, 28, 36, 37, 45].

Phillips et. al. proposed a model on cortico-limbic interaction for emotion regulation, which includes prefrontal cortex, hippocampus and parahippocampus participating in automatic regulatory subprocesses [30]. Phillips et. al. then used the model for emotion regulation for the investigation of bipolar disorder (BD). BD is characterized by major emotion dysregulation. It was further suggested structural changes in dorsal and ventral prefrontal cortices [30]. Combining these studies it seems clear that the symptoms observed in SAD patients arise from dysfunctions in the emotion regulation network.

However, DTI-based evidence for dysfunctions in the cortico-limbic circuitry is limited. Not many studies focused on white matter alterations in social phobia and reported significant differences in anatomical connectivity between SAD patients and healthy controls. In 2009 Phan et. al. presented preliminary evidence of white matter alterations in generalized SAD [29]. The study performed a whole brain analysis reporting lower FA in SAD patients in the right uncinate fasciculus (UF) next to orbitofrontal cortex (OFC). UF connects prefrontal and anterotemporal regions via amygdalae with frontal regions terminating in the OFC [13]. This pathway is believed to play an important role in emotion regulation [12]. Hence Phan et. al. suggested that these white matter abnormalities affect the social interaction. A very recent study on SAD partially confirmed these

findings [5]. A region of interest analysis of the UF revealed low FA in the left UF next to OFC and in the left temporal lobe next to superior longitudinal fasciculus. It is unclear, whether this unilaterality was caused by true functional differences or possible methodological shortcomings. Here we aimed at extending previous results by (1) using high-resolution DTI data acquired at high field, (2) applying both FA-based and probabilistic DTI analysis techniques to better assess anatomical connectivity changes in SAD patients, and (3) measuring in 30 directions to improve the approximation of the diffusion tensor.

## 5.2 Methods

### 5.2.1 Subjects

SAD diagnosis was established based on psychiatric screening assessments including structural clinical interview (SCID), Hamilton anxiety scale (HAMA), Spielberger state and trait anxiety inventory (STAI) and the Liebowitz social anxiety scale (LSAS), for details refer to table 1. Clinically assessment was performed by a trained psychiatrist at the Department of Psychiatry of the General Hospital Vienna. Patients had to fulfill criteria for SAD according to DSM-IV criteria assessed by the SCID.

Inclusion criteria for all subjects were age of 18 to 50 years, physical health and signed written informed approval. Exclusion criteria were physical and neurological abnormalities, pregnancy, additional neurological disorders including depressive disorders independent from social phobia. Any known history of substance abuse led to exclusion. Recent drug abuse was ruled out using a ToxiQUICK PAN-10 test panels (ACON Laboratories, San Diego, USA).

|              | SAD Patients | HC       | p-value |
|--------------|--------------|----------|---------|
| Age          | 26.8±8.7     | 25.4±3.4 | > 0.6   |
| LSAS         | 75.6±22.7    | 5.3±7.3  | < 0.001 |
| STAI( state) | 42.1±12.8    | 25.6±3.3 | < 0.001 |
| STAI (trait) | 52.26±11.2   | 27±4.8   | < 0.001 |
| HAMA         | 16.9±5.0     | 0.5±0.6  | < 0.001 |

**Table 5.1:** Characteristics of control and patients group. Hamilton anxiety scale (HAMA), Spielberger state and trait anxiety inventory (STAI trait and state) and the Liebowitz social anxiety scale (LSAS) scores were assessed during a structural clinical interview. Table shows average score± standard deviation.

19 SAD patients and 17 age-matched healthy control (HC) subjects were recruited. 4 SAD patients were excluded (1 exclusion due to positive drug test, 1 exclusion due to a dental implant which yielded intolerable image distortions in the orbitofrontal cortex, 1 exclusion due to technical difficulties during data acquisition, and 1 exclusion in consequence of violation of our study pro-

tol). 2 HC were excluded (due to violation of our study protocol). As a result, 15 SAD patients and 15 healthy controls were finally included (patient group: 26.6 ( $\pm 8.6$ ) years, 8 females, all right handed; control group: mean age = 25.4 ( $\pm 3.4$ ) years, 7 females, all right handed). For group characteristics see table 5.1.

### 5.2.2 Acquisition

Subjects were examined on a 3 Tesla Tim Trio MR scanner (Siemens Medical, Erlangen, Germany). DTI acquisition was performed with 1.6 mm isotropic resolution in 30 directions in 70 slices and a maximum b-value of 800 s/mm<sup>2</sup>. DTI Data was assessed using Echo-Planar-Imaging (EPI) with parallel imaging (Grappa=2) with the following parameters  $TR = 8621$  ms and  $TE = 83$  ms. For normalization purposes, T1-weighted anatomical images were also acquired using an MPRAGE sequence (resolution  $1 \times 1 \times 1.1$  mm<sup>3</sup>,  $240 \times 256 \times 160$  pixel,  $TE = 4.21$  ms,  $TR = 2300$  ms).

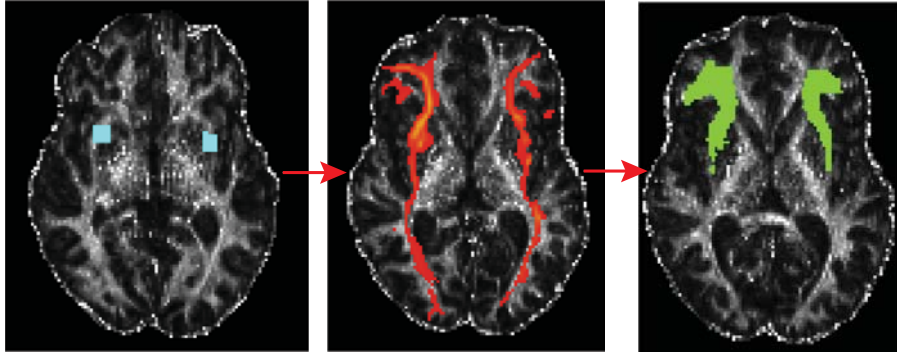
## 5.3 Analysis

Image processing was performed using FSL (Centre of functional MRI of the Brain, University of Oxford, United Kingdom) and SPM8 (Wellcome Trust Centre for Neuroimaging, University College London, United Kingdom). After eddy current correction, binary brain masks were calculated by applying the brain extraction tool (FSL BET) on the unweighted ( $b = 0$  s/mm<sup>2</sup>) EPI volumes. These masks were then applied on the diffusion data and the diffusion tensor model was fitted at each voxel yielding FA, mean diffusivity (MD) and eigenvalue ( $\lambda_1, \lambda_2, \lambda_3$ ) maps.

High-resolution T1-weighted images were first co-registered to the unweighted EPI images and then normalized using SPMs *Segmentation* function. The resulting transformation matrices were then applied to FA, MD and  $\lambda$  images to obtain maps in MNI space. The normalized images were smoothed with isotropic Gaussian kernels with a full width half maximum (FWHM) of 6mm.

Based on our hypothesis of changes in cortico-limbic connections we limited our analysis to the uncinate fasciculus (UF). In order to obtain subject-specific masks of the UF we used probabilistic fiber tracking as implemented in FSL's FDT toolbox. This probabilistic fiber tracking routine allows estimation of multiple fiber orientations per voxel by calculating local probability density functions and using these to approximate the global connectivity. The result is a probability distribution of the white matter connectivity (see [www.fmri.ac.uk/fsl/fdt/fdt\\_bedpostx.html](http://www.fmri.ac.uk/fsl/fdt/fdt_bedpostx.html) or [6, 7]).

On the basis of these calculations fiber tracking can be performed using the *PROBTRACKX* routine. Two cubic seed masks (length 5 voxels) were placed in posterior parts of the UF (according to John Hopkins University White-Matter-Tractography atlas - included in the software package FSL) next to the amygdalae as demonstrated previously ([42]). The mask was defined in MNI space. For fiber tracking the masks need to be in native space. Therefore the MNI seed mask was



**Figure 5.1:** Fiber tracking is performed in the native space of a subject, therefore the masks need to be transformed to native space by applying the inverse matrix of the normalization matrix. These transformed masks can be seen in the left image. The next step is the fiber tracking (middle image). The last step was averaging and thresholding all tracking results of all subjects. Irrelevant parts were cut off by comparing tracking results to JHU tracking atlas. Results can be seen in the right image.

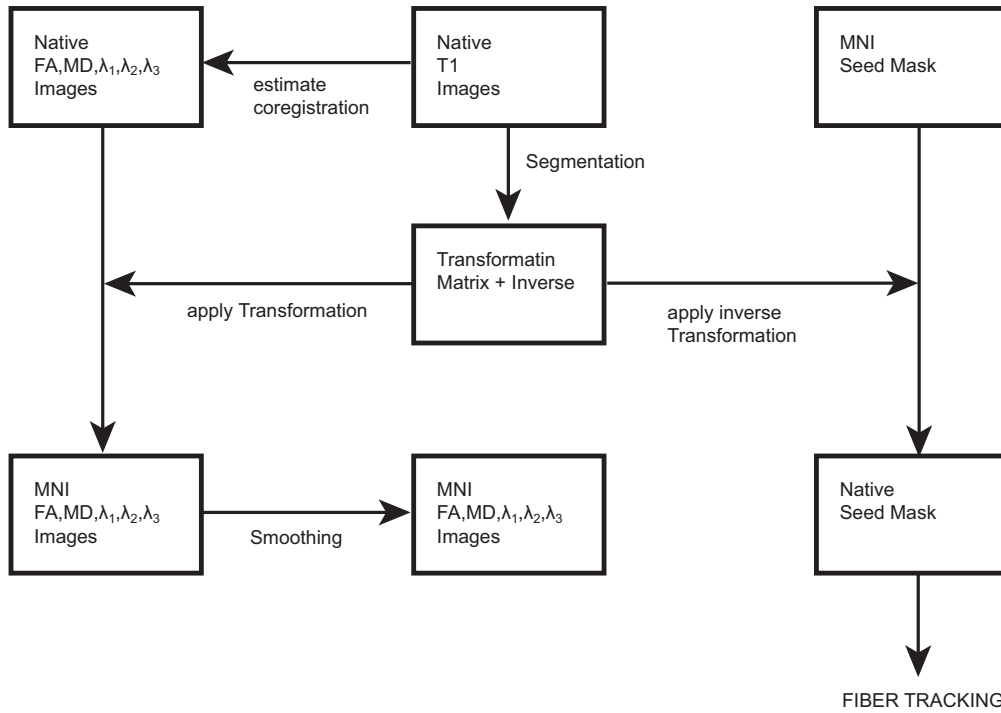


**Figure 5.2:** Outline of the normalization routine for DTI data and seed masks. All steps of the normalization were performed in SPM8.

transformed by using the inverse transformation matrix of the normalization routine above. Fiber tracking was then performed in FSL using *PROBTRACKX* routine for all subjects. Number of samples was 5000, and calculation of every sample was terminated after 2000 steps with a step length of 0.5mm. The curvature threshold was set to 0.2 (approximately  $\pm 80^\circ$ ). An outline of several steps can be found in figure 5.2.

Resulting probabilistic data was normalized, averaged over the whole group and thresholded to calculate the specific mask of the UF. This mask was used for all group-level tests. The calculation steps can be seen in figure 5.1.

Statistical testing was performed in SPM8 using a two-sample t-test. For all statistical tests, significance threshold were set at a voxel-wise  $p < 0.05$  uncorrected with a minimum cluster size of 100 voxel. The main analysis focused on group differences in FA. In addition we compared MD,  $\lambda_1$ ,  $\lambda_2$  and  $\lambda_3$  between groups within statistically significant clusters regarding FA.

## 5.4 Results

The analysis was limited to the UF that was calculated using probabilistic fiber tractography. For all analyses  $p$  was smaller than 0.05 uncorrected. Voxel threshold was set to 100 voxel.

Group analysis for differences in FA between SAD patients and controls revealed lower FA in SAD patients bilaterally in anterior parts of the UF (see table 5.2 for details). In addition, increased FA values in SAD patients relative to HC were found in posterior parts of the UF (see table 5.2).

Fig. 5.4 shows a multislice image with significant alterations in FA values highlighted in blue (SAD < HC) and red (SAD > HC). A 3-dimensional figure of the same results can be seen in 5.3. In this figure decreased FA values in SAD patients are again highlighted in blue and increased FA values in red. In addition you can see the region of interest that has been calculated by probabilistic fiber tractography (cyan envelope). Detailed results can be found in table 5.2.

To investigate this FA decrease in anterior parts of the UF in patients (see blue highlighted voxel in fig. 5.4 and fig. 5.3) we additionally analyzed MD,  $\lambda_1$ ,  $\lambda_2$  and  $\lambda_3$ . For this we examined the peak voxel of significant clusters regarding FA across groups. The mean diffusivity in patients was significantly increased in anterior parts of UF. Comparing this with the  $\lambda_1$ ,  $\lambda_2$  and  $\lambda_3$ , we find that this increased mean diffusivity yields from a significant increase of  $\lambda_2$  and  $\lambda_3$  in patients.  $\lambda_1$  did not show significant alterations. Remembering section 3 we see that the diffusion in SAD patients is more isotropic in anterior parts of the UF relative to healthy control subjects. When we think of the diffusion ellipsoid increased  $\lambda_2$  and  $\lambda_3$  yield a more spherical shape which reduces FA. The results of the MD,  $\lambda_1$ ,  $\lambda_2$  and  $\lambda_3$  analysis can be see in figure 5.5 and figure 5.6. Figure 5.5 shows the values of MD,  $\lambda_1$ ,  $\lambda_2$  and  $\lambda_3$  with error bars in the voxel (-29,34,-6) near left OFC. Figure 5.6 shows changes near right OFC in the voxel (41,33-9). Significant values are indicated

| Contrast | MNI  |       |     |    |     | Comment             |
|----------|------|-------|-----|----|-----|---------------------|
|          | T    | p     | x   | y  | z   |                     |
| SAD<HC   | 3.67 | 0.001 | 41  | 33 | -9  | Near left OFC       |
|          | 2.75 | 0.005 | -29 | 34 | -6  | Near right OFC      |
| SAD>HC   | 3.29 | 0.001 | 30  | 7  | -12 | Near left amygdala  |
|          | 2.90 | 0.004 | -29 | 7  | -10 | Near right amygdala |
|          | 2.39 | 0.012 | -41 | 5  | -24 | Near right amygdala |

**Table 5.2:** Peak voxel of significant clusters ( $p < 0.05$  uncorrected, voxel threshold of 100 voxel) that can be seen in figure 5.4 and figure 5.3.

with \*.

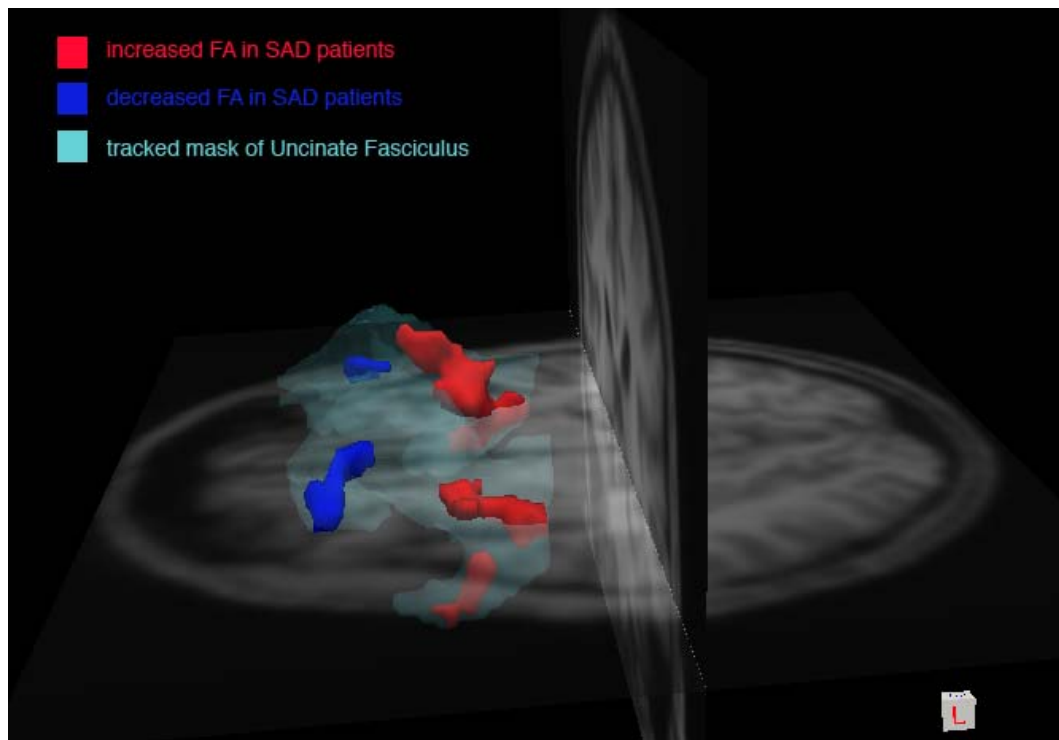


**Figure 5.3:** The envelope represents the results from probabilistic fiber tracking averaged over all subjects. Inside this area voxel with high FA of patients relative to healthy controls are highlighted red, whereby voxel with lower FA of patients are highlighted blue.



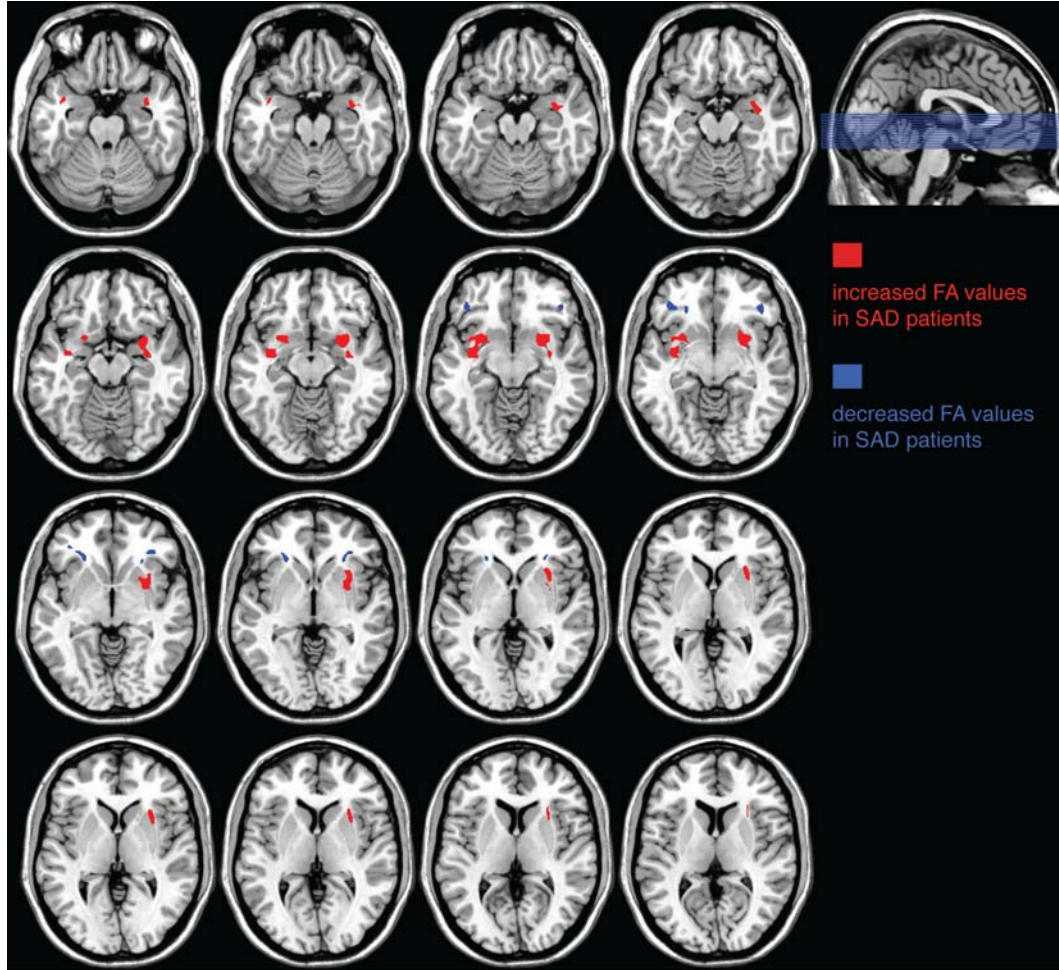


**Figure 5.4:** Fractional Anisotropy. Voxel with increased FA relative to healthy controls are highlighted red. Voxel with decreased FA are highlighted blue. Chosen slices are even slices between slice 50 and 80 in z-direction.

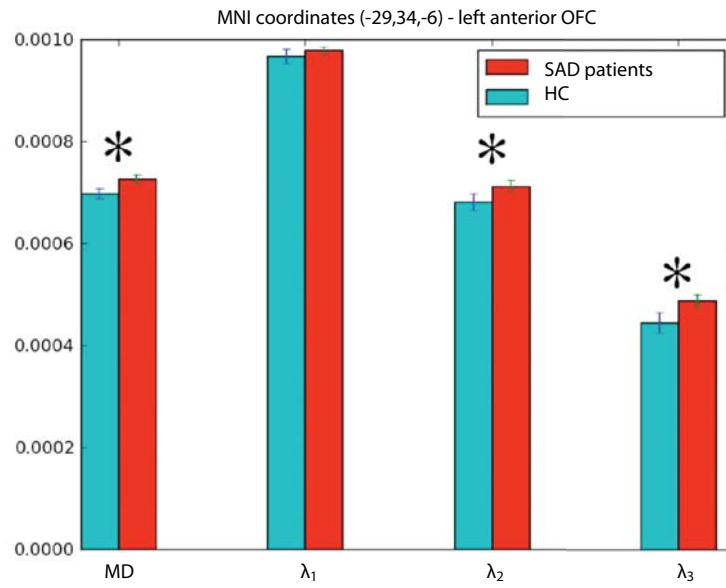


**Figure 5.5:** Changes in MD,  $\lambda_1$ ,  $\lambda_2$  and  $\lambda_3$  (peak voxel coordinates: -29, 34, -6 - near left OFC) with error bars. Significant deviations are indicated with \*. SAD Patients (red) show increased values of MD and radial eigenvalues ( $\lambda_2$  and  $\lambda_3$ ) compared to healthy controls (cyan). This leads to a more isotropic diffusion yielding lower FA.

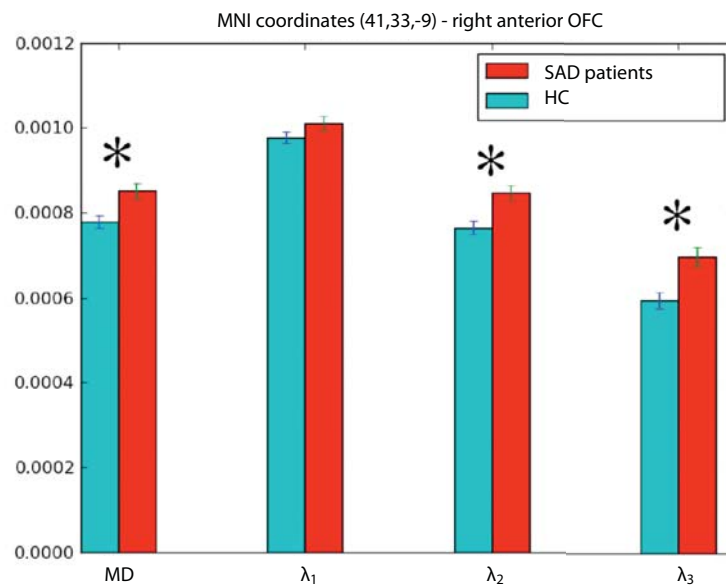


**Figure 5.6:** Changes in MD,  $\lambda_1$ ,  $\lambda_2$  and  $\lambda_3$  (peak voxel coordinates: -41,33,-9 - near right OFC) with error bars. Significant deviations are indicated with \*. SAD Patients (red) show increased values of MD and radial eigenvalues ( $\lambda_2$  and  $\lambda_3$ ) compared to healthy controls (cyan). This leads to a more isotropic diffusion yielding lower FA.

## 5.5 Discussion

In this study we have examined differences in white matter properties between SAD patients and matched healthy controls. Based on the main symptoms of SAD, i.e. intense and irrational fear in a social context, we restricted our analysis to the uncinate fasciculus, which connects amygdalae as the central structures in the human emotion processing circuitry, to orbitofrontal brain regions. Given the OFC's role in regulating limbic activity in general and amygdalar activity in particular, we hypothesized reduced connectivity in the uncinate fasciculus of SAD patients. Such reductions in connectivity should be reflected in reduced FA values as assessed with DTI methodology.

Our results show indeed a reduction in FA values in the anterior parts of the uncinate fasciculus of SAD patients. This is in agreement with a previous study by Phan who reported reduced FA in the right hemisphere. A very recent study by Baur shows two regions with reduced FA in the left hemisphere of SAD patients (left UF next to OFC and left temporal lobe next to superior longitudinal fasciculus). Here we were able to confirm the findings next to OFC. Our results not only corroborate these two previous studies in showing a left and right hemispheric reduction of FA near UF in SAD patients but also extend these findings to both hemispheres. The reason for this unilaterality and hemisphere differences in [29] and [5] are not clear. Baur et. al. argued that their findings corroborate with previous findings suggesting that the left OFC plays a role in changes of the functional connectivity pattern in SAD. However concerning the hemisphere differences Baur et. al. requested further DTI studies.

Compared to both studies we acquired data with higher spatial resolution. We used an isotropic resolution of 1.6 *mm*. Phan and colleagues had a slice thickness of 3 *mm* and Baur and colleagues of 3.2 *mm*, both had matrix size of  $256 \times 256$  pixel and field-of-view of  $240 \times 240$  *mm*<sup>3</sup>. We acquired 70 slices compared to 36 (Phan) and 39 (Baur), respectively.

It has been shown that FA significantly depends on the number (*N*) of diffusion-weighted directions. A recent study showed that a high number of gradient directions ( $N > 20$ ) is recommended allowing for a better visualization of white matter tracts in FA maps and increasing the contrast-to-signal variance ratio [14]. In addition it has been found a significant dependences of  $\lambda_1$ ,  $\lambda_2$  and  $\lambda_3$  to the number of gradient directions. For a region-of-interest analysis more than 21 diffusion weighted directions are recommended for a better estimation of  $\lambda_1$ ,  $\lambda_2$  and  $\lambda_3$  [26]. Hence we measured in 30 diffusion-weighted directions (Phan-study: 12; Baur-study: 21), which allows for a better approximation of water diffusion.

It has been shown that different smoothing kernels can lead to different results [18]. Here smoothing was performed with a Gaussian kernel of 6 *mm*. Baur et. al. also used the same smoothing kernel. Phan et. al. used Gaussian kernels of 5 *mm* and 9 *mm* yielding similar results. This could possibly yield to small differences in the results. Since Phan et. al. found similar effects with 5 *mm* and 9 *mm*, the differences to a Gaussian kernel of 6 *mm* should not be crucial.

Concerning the characteristics of the study population, score differences of the psychiatric assessments between SAD patients and HC were on average larger compared to Phan and Baur. Patients showed on average higher scores than compare to the study population of Phan and Baur and HC showed on average lower scores. Summarized we had better underlying conditions to exam white matter alterations, which could be the reason why Phan and Baur only found unilateral abnormalities.

None of the previous studies found increased FA in SAD patients, however we found significantly increased FA in the UF near amygdalae bilaterally. The interpretation of these results is difficult. The anatomical structure of the close vicinity in the UF near amygdala is utterly different compared to the just addressed areas. Therefore we cannot exclude partial volume effects. Further studies are required to clarify this issue.

In summary we have found strong evidence of structural alterations in social phobia which confirms and expands previous findings [5,29] to both hemispheres. In addition we found areas with significantly increased FA in social phobia patients.

## Chapter 6

# Conclusion and Outlook

DTI is one of the most promising tools to examine organized tissue in the human body, such as the human brain or muscles. In this master thesis DTI has been successfully applied for analyzing white matter alterations. Using the data of 30 subjects (15 social phobia patients, 15 healthy control), fractional anisotropy, mean diffusivity and diffusion eigenvalues have been calculated. Statistical analysis was performed to find group differences in FA, MD and eigenvalues. The results confirmed and expanded previous studies [5, 29]. For image preprocessing different normalization techniques (standard normalization, DARTEL normalization, TBSS) have been applied and tested. Probabilistic fiber tracking was performed for all 30 subjects to create a study specific mask. In addition deterministic fiber tracking algorithms have been tested. The preprocessing pipelines for DTI presented in this master thesis will be applicable on several recent studies in progress at the MR Centre of Excellence (Medical University of Vienna):

- DTI of glaucoma

Glaucoma is an eye disorder resulting a damage of the optic nerve. Since this damage yields alterations in the diffusion due to demyelination of the fibers DTI can be used for quantization of the damage.

- Steroid hormones

Application of steroid hormones such as oestrogen or testosterone in transgender patients might lead to structural changes in the human brain which can be analyzed using DTI.

For further DTI studies different acquisition parameters, such as number of gradient directions, acquisition time and variation of b-values, can be used to investigate benefits for image quality. Besides the typical diffusion parameters the axonal parameter can be estimated using diffusion MRI. The axon diameter gives additional information on the tissue. Existing models for axon diameter approximation assume a single fiber direction per voxel and the same diameter for all axons. These assumptions often lead to an overestimation of the diameter. A very recent approach

is the so-called axon diameter mapping. This technique considers an axon diameter distribution and allows orientation dispersion yielding improvements in the estimation of the axon diameter [47].

In general diffusion is far more complicated to be approximated by a symmetric diffusion tensor. Hence there exist several more sophisticated non-tensor approximations of water diffusion. DTI cannot identify structures such as fiber bendings, crossings and twistings within a voxel. However these intravoxel structures can be approximated using Q-ball imaging. The Q-ball algorithm can estimate multiple fiber directions without assumption of Gaussian diffusion. Data acquisition for Q-ball imaging, however, is very time-consuming and needs large pulsed diffusion gradients [40]. Such an acquisition protocol measures in more directions and uses higher b-values. Sequences that only use one b-values are called HARDI (high-angular-resolution diffusion imaging) sequences.

A technique that retrieves fiber directions from HARDI data is the so-called spherical deconvolution. This method considers the signal from a single voxel as the sum of all contributing fiber bundles and hence determines the real distribution of fiber orientations [39].

Another method that allows for approximating multiple fiber directions within a single voxel is diffusion spectrum imaging (DSI) [43]. DSI needs typically 300-500 measurements in many directions with high b-values (up to  $b \sim 17000 \text{ s/mm}^2$ ) [23].

All these non-tensor methods aim for a better approximation of the true nature of diffusion. These methods, however, require longer measurement times because of the time consuming data sampling and large diffusion gradients. Nevertheless, such approaches may be successfully applied in future studies given the possibilities for accelerated acquisition at ultra-high magnetic field strengths.

# Bibliography

- [1] J Ashburner. Spm8 manual. *Imaging*, 2009.
- [2] J Ashburner and K J Friston. Voxel-based morphometry - the methods. *NeuroImage*, 11(6):805–821, 2000.
- [3] John Ashburner. A fast diffeomorphic image registration algorithm. *NeuroImage*, 38(1):95–113, 2007.
- [4] P J Basser, S Pajevic, C Pierpaoli, J Duda, and A Aldroubi. In vivo fiber tractography using dt-mri data. *Magnetic Resonance in Medicine*, 44(4):625–632, 2000.
- [5] V Baur, J Hänggi, M Rufer, A Delsignore, L Jäncke, L Herwig, and A B Bruühl. White matter alterations in social anxiety disorder. *Journal of Psychiatric Research*, 3, 2011.
- [6] T E J Behrens, H J Berg, S Jbabdi, M F S Rushworth, and M W Woolrich. Probabilistic diffusion tractography with multiple fibre orientations: What can we gain? *NeuroImage*, 34(1):144–155, 2007.
- [7] T E J Behrens, M W Woolrich, M Jenkinson, H Johansen-Berg, R G Nunes, S Clare, P M Matthews, J M Brady, and S M Smith. Characterization and propagation of uncertainty in diffusion-weighted MR imaging. *Magnetic Resonance in Medicine*, 50(5):1077–1088, 2003.
- [8] N Birbaumer, W Grodd, O Diedrich, U Klose, M Erb, M Lotze, F Schneider, U Weiss, and H Flor. fMRI reveals amygdala activation to human faces in social phobics. *NeuroReport*, 9(6):1223–1226, 1998.
- [9] Karleyton C Evans, Christopher I Wright, Michelle M Wedig, Andrea L Gold, Mark H Pollack, and Scott L Rauch. A functional MRI study of amygdala responses to angry schematic faces in social anxiety disorder. *Depression and Anxiety*, 25(6):496–505, 2008.
- [10] Taylor F. *Digital Filters: Principles and Applications with MATLAB*. Wiley-IEEE Press, 2011.
- [11] R Frackowiak, K J Friston, C Frith, R Dolan, and J Mazziotta. Human brain function. *Academic Press*, 2:xiii, 528 p., 1997.

- [12] H T Ghashghaei and H Barbas. Pathways for emotion: interactions of prefrontal and anterior temporal pathways in the amygdala of the rhesus monkey. *Neuroscience*, 115(4):1261–1279, 2002.
- [13] H T Ghashghaei, C C Hilgetag, and H Barbas. Sequence of information processing for emotions based on the anatomic dialogue between prefrontal cortex and amygdala. *NeuroImage*, 34(3):905–923, 2007.
- [14] Marco Giannelli, Mirco Cosottini, Maria Chiara Michelassi, Guido Lazzarotti, Gina Belmonte, Carlo Bartolozzi, and Mauro Lazzeri. Dependence of brain DTI maps of fractional anisotropy and mean diffusivity on the number of diffusion weighting directions. *Journal of applied clinical medical physics American College of Medical Physics*, 11(1):2927, 2010.
- [15] E W Hsu, A L Muzikant, S A Matulevicius, R C Penland, and C S Henriquez. Magnetic resonance myocardial fiber-orientation mapping with direct histological correlation. *American Journal of Physiology*, 274(5):1627–1634, 1998.
- [16] J E Humphreys. *Introduction to Lie algebras and representation theory*, volume 9. Springer, 1972.
- [17] H Johansen-Berg. *Diffusion MRI: from quantitative measurement to in-vivo neuroanatomy*. Academic Press, 2009.
- [18] D K Jones, M R Symms, M Cercignani, and R J Howard. The effect of filter size on vbm analyses of dt-mri data. *NeuroImage*, 26:546–54, 2005.
- [19] D Le Bihan, J F Mangin, C Poupon, C A Clark, S Pappata, N Molko, and H Chabriat. Diffusion tensor imaging: concepts and applications. *Journal of Magnetic Resonance Imaging*, 13(4):534–546, 2001.
- [20] Z-P Liang and P Lauterbur. *Principles of Magnetic Resonance Imaging: A Signal Processing Perspective*. Wiley-IEEE Press, 1999.
- [21] S M Lynch. Introduction to applied bayesian statistics and estimation for social scientists. *Journal of the American Statistical Association*, 103(483):1322–1323, 2008.
- [22] H Mori. Diffusion tensor imaging. *Rinsho shinkeigaku Clinical neurology*, 48(11):945–946, 2008.
- [23] S Mori. *Introduction to Diffusion Tensor Imaging*. Elsevier Science, 2007.
- [24] S Mori and P C M Van Zijl. Fiber tracking: principles and strategies - a technical review. *NMR in Biomedicine*, 15(7-8):468–480, 2002.



- [25] S Mori and J Zhang. Principles of diffusion tensor imaging and its applications to basic neuroscience research. *Neuron*, 51(5):527–539, 2006.
- [26] H Ni, V Kavcic, T Zhu, S Ekholm, and J Zhong. Effects of number of diffusion gradient directions on derived diffusion tensor imaging indices in human brain. *Ajnr American Journal Of Neuroradiology*, 27(8):1776–1781, 2006.
- [27] Structural Brain Mapping Group University of Jena. <http://dbm.neuro.uni-jena.de/vbm/>.
- [28] K L Phan, D A Fitzgerald, P J Nathan, and M E Tancer. Association between amygdala hyperactivity to harsh faces and severity of social anxiety in generalized social phobia. *Biological Psychiatry*, 59(5):424–429, 2006.
- [29] K L Phan, E Orlichenko, Aand Boyd, M Angstadt, E F Coccaro, I Liberzon, and K Arfanakis. Preliminary Evidence of White Matter Abnormality in the Uncinate Fasciculus in Generalized Social Anxiety Disorder. *Biological Psychiatry*, 66(7):691–694, 2009.
- [30] M L Phillips, C D Ladouceur, and W C Drevets. A neural model of voluntary and automatic emotion regulation: implications for understanding the pathophysiology and neurodevelopment of bipolar disorder. *Molecular Psychiatry*, 13(9):829, 833–857, 2008.
- [31] RadioGraphics. <http://radiographics.rsna.org/>.
- [32] F Schmitt and R Stehling, Mand Turner. *Echo-Planar Imaging: Theory, Technique and Application*. Springer, 1998.
- [33] D F Scollan, A Holmes, R Winslow, and J Forder. Histological validation of myocardial microstructure obtained from diffusion tensor magnetic resonance imaging. *American Journal of Physiology*, 275(6):2308–2318, 1998.
- [34] S M Smith, M Jenkinson, H Johansen-Berg, D Rueckert, Th E Nichols, C E Mackay, K E Watkins, O Ciccarelli, M Z Cader, P M Matthews, and T E J Behrens. Tract-based spatial statistics: voxelwise analysis of multi-subject diffusion data. *NeuroImage*, 31(4):1487–1505, 2006.
- [35] M B Stein, P R Goldin, J Sareen, L T E Zorrilla, and G G Brown. Increased amygdala activation to angry and contemptuous faces in generalized social phobia. *Archives of General Psychiatry*, 59(11):1027–1034, 2002.
- [36] M B Stein and D J Stein. Social anxiety disorder. *Lancet*, 371(9618):1115–1125, 2008.
- [37] T Straube, I-T Kolassa, M Glauer, H-J Mentzel, and W H R Miltner. Effect of task conditions on brain responses to threatening faces in social phobics: an event-related functional magnetic resonance imaging study. *Biological Psychiatry*, 56(12):921–30, 2004.

- [38] J Talairach and P Tournoux. *Co-planar stereotaxic atlas of the human brain: 3-dimensional proportional system: an approach to cerebral imaging*, volume 39. Thieme, 1988.
- [39] J-D Tournier, F Calamante, D G Gadian, and A Connelly. Direct estimation of the fiber orientation density function from diffusion-weighted mri data using spherical deconvolution. *NeuroImage*, 23(3):1176–1185, 2004.
- [40] D S Tuch. Q-ball imaging. *Magnetic Resonance in Medicine*, 52(6):1358–1372, 2004.
- [41] Oxford University. <http://users.fmrib.ox.ac.uk/>.
- [42] S Wakana, A Caprihan, M M Panzenboeck, J H Fallon, M Perry, R L Gollub, K Hua, J Zhang, H Jiang, and P Dubey. Reproducibility of quantitative tractography methods applied to cerebral white matter. *Neuroimage*, 36(3):630–644, 2007.
- [43] V J Wedeen, R P Wang, J D Schmahmann, T Benner, W Y I Tseng, G Dai, D N Pandya, P Hagmann, H DArceuil, and A J De Crespigny. Diffusion spectrum magnetic resonance imaging (dsi) tractography of crossing fibers. *NeuroImage*, 41(4):1267–1277, 2008.
- [44] Wikipedia. <http://en.wikipedia.com>.
- [45] K L Yoon, D A Fitzgerald, M Angstadt, R A McCarron, and K L Phan. Amygdala reactivity to emotional faces at high and low intensity in generalized social phobia: a 4-Tesla functional MRI study. *Psychiatry Research*, 154(1):93–98, 2007.
- [46] L Younes. *Shapes and Diffeomorphisms*. Springer, 2010.
- [47] H Zhang, Pl Hubbard, Gjm Parker, and Dc Alexander. Axon diameter mapping in the presence of orientation dispersion with diffusion mri. *NeuroImage*, 56(3):640–647, 2011.

# List of Figures

|     |  |    |
|-----|--|----|
| 1.1 | Classical picture of the angular momentum $\mathbf{l}$ and magnetic moment $\boldsymbol{\mu}$ due to the orbital motion of the electron with the velocity $\mathbf{v}$ and the radius $r$ . . . . .  | 10 |
| 1.2 | Quantized angular momentum with $l = 2$ . . . . .  | 11 |
| 1.3 | Stern-Gerlach Experiment. The particle beam of neutral silver atoms passes through an inhomogeneous magnetic field in z-direction. In the figure you see the set-up of the magnetic poles, which produce the magnetic field. The particle beam is detected at a photographic plate. Without a magnetic field no deflection is measured (straight line at photographic plate). When the magnetic field is turned on the classical expectation was a homogenous distribution, as it was believed that the orientation of the magnetic moment should be random. But the results showed two clear maxima. This is due to the quantization of $s_z$ . Only two orientations are possible (spin up and spin down) yielding the two maxima. . . . . | 13 |
| 1.4 | Two possible orientations (spin up and spin down) of the electron spin. . . . .  | 14 |
| 1.5 | Excitation of magnetization vector while the radio-frequency field is applied. Plotted with gnuplot ( <a href="http://www.gnuplot.info">www.gnuplot.info</a> ). . . . .  | 22 |
| 1.6 | $T_2$ relaxation after $90^\circ$ RF- Pulse compared to $T_2^*$ relaxation. When the radio-frequency (RF) field is switched on the magnetization flips to the x-y-plane. When the spins get out of phase the transversal magnetization $M_{x,y}$ decreases. This decrease is due to spin-spin interactions. But the actual decrease we are measuring is due to $T_2^*$ relaxation. . . . .   | 24 |
| 1.7 | $T_1$ relaxation after $90^\circ$ RF- Pulse. When the radio-frequency (RF) field is switched on the magnetization flips to the x-y-plane. After the pulse the longitudinal magnetization recovers due to the longitudinal relaxation. . . . .  | 24 |
| 2.1 | Examples of Fourier transforms. (A) Boxcar function vs. sinc function and (B) delta function vs. constant function. . . . .  | 28 |
| 2.2 | Truncation of RF pulse. Since a perfect sinc-pulse with an infinite duration is not realizable in an MR experiment, the pulse is truncated yielding a different slice-selection profile an example seen in this figure (from <a href="http://www.currentprotocols.com">http://www.currentprotocols.com</a> ). . . . .  | 29 |

|      |   |    |
|------|---|----|
| 2.3  | (a) sagittal slice (x-axis), (b) coronal slice (y-axis) and (c) axial slice (z-axis) [41]. .  | 30 |
| 2.4  | The upper figure shows the effect of the readout gradient on the Larmor frequencies. This gradient is applied during data acquisition yielding different precession frequencies at different spatial positions. The bottom figure shows the effect of the phase-encoding gradient. This gradient is applied for the time $T_{PE}$ before data acquisition yielding a phase shift for different spatial positions. . . . .   | 32 |
| 2.5  | k-space trajectories. In the left image a line is measured for every $T_R$ . After the line is acquired the signal is reformed and a new phase-encoding gradient is applied, yielding a new line. In the right image we see a typical EPI sequence. After every readout line a new phase-encoding gradient is applied. In this sequence the data acquisition of the readout line must be fast enough that all lines can be measured while the MR signal is still present, therefore the acquisition time for each line is smaller, this needs strong gradient fields. . . . . | 34 |
| 2.6  | This figure shows the effects of missing k-space data. This case is simulated by setting distinct points zero as shown in the left column indicated with a black box. (A) contains the whole k-space. (B) The center is set zero, the image only contains small structures. (C) The periphery is set zero yielding a low-resolution image containing contrast information. Figure modified from [31]. . . . .   | 34 |
| 2.7  | Spin echo sequence. A $90^\circ$ pulse is applied and the magnetization is flipped to the x-y-plane. Due to dephasing of the spins, the magnetization is decaying. After $T_E/2$ a $180^\circ$ pulse is applied. The spins rephase and a spin echo can be measured at the time $2\tau$ . The signal is attenuated due to spin-spin interaction ( $e^{-2\tau/T_2}$ ). . . . .  | 35 |
| 2.8  | EPI sequence. After excitation prephasing gradients are applied. Subsequently readout gradient are applied with changing polarity. Gradient "blips" are applied for a very short time between readout gradients. . . . .  | 36 |
| 2.9  | Misregistration due to chemical shift. The fat signal is shifted to lower frequencies [20].   | 37 |
| 2.10 | Typical frequency-encoding period. Dashed line shows effects of motion in the frequency-encoding direction yielding a different phase shift than compared to no motion (black line) [20]. . . . .   | 38 |
| 2.11 | Aliasing due to undersampling. In the upper figure you see a signal measured with an adequate sampling frequency ( $f_s > f_{Nyquist}$ ). In the bottom figure you see the same signal with a sampling frequency not meeting the Nyquist criterion, therefore the reconstructed signal does not represent the original signal. . . . .  | 41 |
| 2.12 | Aliased MR image due to undersampling. . . . .  | 41 |

|     |  |    |
|-----|--|----|
| 3.1 | Basics of diffusion measurement. A strong static magnetic field $B_0$ is applied in z-direction. A $90^\circ$ pulse flips the spins to the x-y-plane. All spins have the same precision frequency. After the time $t_1$ a dephasing pulse is applied (switch off at $t_2$ ). In this figure we can see how the dephasing pulse yields different precision frequencies of the spins, the spins get out of phase and the signal vanishes. At $t_3$ a rephasing pulse is applied. When the spins did not change their position, the rephasing pulse brings the spins back in phase and the full signal can be measured. Figure taken from [23]  | 45 |
| 3.2 | Basics of diffusion measurement. The upper row shows the case of no diffusion. In this case the rephasing pulse focuses all spins. In the lower row diffusion is allowed. In this case the dephasing and rephasing gradient are in z-direction (the color implies different Larmor frequencies due to the gradient). If spins change their position vertically this would not affect the signal, but when they change their position horizontally the rephasing gradient does not have the same effect on the spins due to their different phase shift resulting from the first dephasing pulse. Figure modified from [25].  | 45 |
| 3.3 | (A) $\tau \ll \Delta$ . Diffusion during gradient pulse can be neglected (B) Realistic diffusion gradients. Diffusion during gradient pulse cannot be neglected. Modified from [23].   | 46 |
| 3.4 | Time course of diffusion gradients. The bottom figure shows the acquired phase angle as function of time. Modified from [23].  | 48 |
| 3.7 | (A) shows the approximation of the diffusion tensor, several measured directions are indicated (B) shows the estimated diffusion tensor represented by the diffusion ellipsoid, the three main diffusion axis are drawn in with the corresponding eigenvalues $\lambda_1$ , $\lambda_2$ and $\lambda_3$ . (C) shows the main diffusion axis with the largest eigenvalue. (D) shows an FA image with typical ellipsoids for grey matter (nearly spherical ellipsoid) and white matter images (elongated ellipsoid). (E) show the color encoding for the same FA image which converted the information given by the diffusion tensor to colors (left-right in red, anterior-posterior in green, superior-inferior in blue). (F) focuses on the conversion of color and orientation. Figure modified from [25]. | 50 |
| 3.5 | Data was acquired at a 3 Tesla MRI scanner. FA images of 15 healthy subjects were averaged.  | 51 |
| 3.6 | (A) Axial slice with color encoding (left-right in red, anterior-posterior in green, superior-inferior in blue). (B) Axial slice with color encoding (left-right in red, anterior-posterior in green, superior-inferior in blue) and additional vectors matching the main diffusion directions.  | 51 |
| 3.8 | Calculated fiber trajectory of a 3D space curve $\mathbf{r}(s)$ using Euler's method. $\mathbf{r}(s_1)$ is parallel to $\mathbf{e}_1(\mathbf{r}(s_1))$ , which belongs to the largest eigenvalue. Figure taken from [4]  | 53 |

|      |  |    |
|------|--|----|
| 3.9  | Deterministic fiber tracking of a healthy single subject using the software package <i>TrackVis</i> . No seed mask was used. Fiber tracking was performed for the whole brain.   | 54 |
| 3.10 | Deterministic fiber tractography of the UF of a healthy single subject using two seed masks bilaterally in posterior parts of the uncinate fasciculus. . . . .   | 54 |
| 3.11 | Probability map of a single subject. The seed masks were placed bilaterally in parts of the uncinate fasciculus. A probability threshold of 50% was set. Yellow indicates high probability. . . . .  | 55 |
| 4.1  | (A) Basis functions with lowest frequencies of a 2 dimensional discrete cosine transform. Deformation fields are linear combinations of these smooth functions. Light areas indicate a shift left/up and dark areas a shift right/down. Image retrieved from [11]. . . . .   | 60 |
| 4.2  | Histogram. Differentiation of different distributions yields tissue classed and background (left image). Using no prior information the initial segmentation results into some misclassification. In the right image segmented grey matter is shown (right image). Since the scalp intensity is similar to grey matter intensity, also the scalp is shown. Image retrieved from [27]. . . . .  | 62 |
| 4.3  | Using Bayesian rules initial segmented images are combined with prior probability maps improving the assignment to a certain tissue class. The red circles indicate the probability of this voxel to belong to grey matter. In the initial segmentation (upper middle image) contains the scalp (probability of 95 %). The bottom image shows the prior probability map not containing the scalp. Combining both images a joint probability map is calculated improving segmentation of the original image. Image retrieved from [27]. . . . . | 62 |
| 4.4  | Segmented grey matter of healthy single subject in native space. Left image processed with <i>New Segment</i> , right image with <i>Segment</i> . Differences are indicated with a red circle. . . . .   | 63 |
| 4.5  | Segmented white matter of healthy single subject in native space. Left image processed with <i>New Segment</i> , right image with <i>Segment</i> . Differences are indicated with a red circle. . . . .  | 63 |
| 4.6  | Smoothing of one data set with an isotropic Gaussian kernel of 3 mm. . . . .   | 64 |
| 4.7  | Non-diffeomorphic transformations. $\phi \times \phi^{-1}$ is unequal $\phi^{-1} \times \phi$ . Figure modified from [3] . . . . .   | 65 |
| 4.8  | Computing of the deformation (left) and the inverse deformation (right). Figure taken from [3]. . . . .  | 67 |
| 4.9  | Composition of forward and inverse transformation yielding a nearly perfect identity transform. Figure taken from [3]. . . . .   | 67 |

|      |   |    |
|------|---|----|
| 4.10 | Segmentation results of a healthy single subject in normalized space (MNI). a) Grey Matter and b) White Matter. . . . .   | 68 |
| 4.11 | a) DARTEL grey matter template b) DARTEL white matter template. Both templates are not in MNI space. . . . .  | 69 |
| 4.12 | Grey matter flow field of a healthy single subject calculated using DARTEL. . . .   | 69 |
| 4.13 | (A) Normalized FA image of a healthy single subject using DARTEL. (B) Normalized FA image using standard pipeline including co-registration, segmentation and normalization . . . . .   | 70 |
| 4.14 | Calculated mean FA image resulting from 30 data sets. Image was calculated in FSL.  | 72 |
| 4.15 | FA skeleton after "thinning" of the mean FA image. . . . .  | 72 |
| 5.1  | Fiber tracking is performed in the native space of a subject, therefore the masks need to be transformed to native space by applying the inverse matrix of the normalization matrix. These transformed masks can be seen in the left image. The next step is the fiber tracking (middle image). The last step was averaging and thresholding all tracking results of all subjects. Irrelevant parts were cut off by comparing tracking results to JHU tracking atlas. Results can be seen in the right image. . . . . | 77 |
| 5.2  | Outline of the normalization routine for DTI data and seed masks. All steps of the normalization were performed in SPM8. . . . .  | 77 |
| 5.3  | The envelope represents the results from probabilistic fiber tracking averaged over all subjects. Inside this area voxel with high FA of patients relative to healthy controls are highlighted red, whereby voxel with lower FA of patients are highlighted blue. .   | 80 |
| 5.4  | Factional Anisotropy. Voxel with increased FA relative to healthy controls are highlighted red. Voxel with decreased FA are highlighted blue. Chosen slices are even slices between slice 50 and 80 in z-direction. . . . .   | 81 |
| 5.5  | Changes in MD, $\lambda_1$ , $\lambda_2$ and $\lambda_3$ (peak voxel coordinates: -29, 34, -6 - near left OFC) with error bars. Significant deviations are indicated with *. SAD Patients (red) show increased values of MD and radial eigenvalues ( $\lambda_2$ and $\lambda_3$ ) compared to healthy controls (cyan). This leads to a more isotropic diffusion yielding lower FA. . . . .   | 82 |
| 5.6  | Changes in MD, $\lambda_1$ , $\lambda_2$ and $\lambda_3$ (peak voxel coordinates: -41,33,-9 - near right OFC) with error bars. significant deviations are indicated with *. SAD Patients (red) show increased values of MD and radial eigenvalues ( $\lambda_2$ and $\lambda_3$ ) compared to healthy controls (cyan). This leads to a more isotropic diffusion yielding lower FA. . . . .  | 82 |





# List of Tables

|     |   |    |
|-----|---|----|
| 1.1 | In this table a small selection of nuclear isotopes including spin, natural abundance and Larmor frequency at 11.4 Tesla are displayed. More Isotopes can be found on <a href="http://www.webelements.com">www.webelements.com</a> . . . . .  | 16 |
| 1.2 | Relaxation times for tissues in the human body at 1.5 Tesla [44]. . . . .   | 25 |
| 5.1 | Characteristics of control and patients group. Hamilton anxiety scale (HAMA), Spielberger state and trait anxiety inventory (STAI trait and state) and the Liebowitz social anxiety scale (LSAS) scores were assessed during a structural clinical interview. Table shows average score $\pm$ standard deviation. . . . . | 75 |
| 5.2 | Peak voxel of significant clusters ( $p < 0.05$ uncorrected, voxel threshold of 100 voxel) that can be seen in figure 5.4 and figure 5.3. . . . .   | 79 |



# Danksagung

Für die Unterstützung bei dieser Masterarbeit möchte ich mich bei allen bedanken.

Ich möchte mich speziell bei Prof. Ewald Moser, Leiter der Arbeitsgruppe am Exzellenzzentrum, bedanken.

Besonderer Dank geht an meine Betreuer Prof. Christian Windischberger und Prof. Gerald Badurek, die es mir ermöglichten diese Masterarbeit zu verfassen.

Ein herzliches Dankeschön geht auch an Emrah, Jacqueline und Ronald.

Auch möchte ich mich bei allen meinen Kollegen am MR-Zentrum bedanken: Claudia, Elmar, Jürgen, Klaudius, Manuela, Roberta, Roland und Wolfgang.

Besonderer Dank gilt auch meinen Eltern, die mich während des ganzen Studiums unterstützt haben und mir dieses überhaupt ermöglicht haben.

Zuletzt möchte ich Markus danken, der mir stets zur Seite stand.